The Study of Zirconium Hydroxide and Zirconium (IV) Metal-Organic Frameworks as Reactive Substrates for the Decomposition of Chemical Warfare Agents

James W. Kollar
Kennesaw State University

The Study of Zirconium Hydroxide and Zirconium (IV) Metal-Organic Frameworks as
Reactive Substrates for the Decomposition of Chemical Warfare Agents

by

James Kollar

B.S. in Chemistry
Clayton State University, 2014

Submitted in Partial Fulfillment of the Requirements
For the Degree of Master of Science in the
Department of Chemistry and Biochemistry
Kennesaw State University
2017
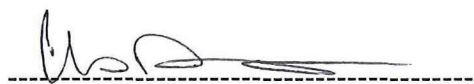
_____   _____
Committee Chair   Graduate Program Coordinator
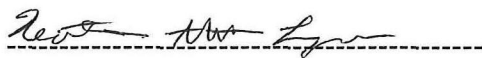
_____   _____
Committee Member   Department Chair

_____   _____
Committee Member   College Dean

ABSTRACT

Nerve agents have been described by the Center for Disease Control and Prevention to be the most toxic and rapidly acting of chemical warfare agents. The present study investigates the efficacy of zirconium hydroxide, $Zr(OH)_4$, and $Zr(IV)$ Metal-Organic Frameworks (MOFs) in the uptake and decomposition of the gas phase nerve agent simulant dimethyl methylphosphonate, DMMP. This investigation was carried out using two different methods: 1) with the use of Diffuse Reflectance Infrared Fourier Transform Spectroscopy (DRIFTS) to examine the surface reaction between DMMP and the solid; and 2) using a flow reactor system that monitored gas phase reaction products produces by the surface reaction. The results show that $Zr(OH)_4$, an amorphous, amphoteric substrate with a Brunauer-Emmeet-Teller (BET) surface area 462 m^2/g greatly outperforms the MOFs, which have 2-6 times the surface area of $Zr(OH)_4$, in both uptake and decomposition of DMMP. $Zr(OH)_4$ acts as a reactive adsorbent which irreversibly binds the phosphorous-containing products from the reaction, in a manner similar to other solid oxides. However, $Zr(OH)_4$ arguably shows the highest reactivity to date, especially for simple metal oxide substrates, in terms of the yield of gas phase products per unit area as well as showing a novel decomposition product containing a P-H moiety. Further investigation of $Zr(OH)_4$ showed that pretreatment of the material by heating either with a flow of ultra-high purity N_2 or under vacuum reduced both adsorption capacity and reactivity; and that post exposure heating led to further reaction including loss of phosphorous containing species from the surface.

TABLE OF CONTENTS

LIST OF FIGURES

LIST OF TABLES

CHAPTER I. BACKGROUND

Detoxification of highly toxic compounds is of the utmost importance, especially those used as chemical warfare agents (CWAs). CWAs have been employed in combat and terroristic acts since WWI, where chlorine gas was deployed during the Battle of Ypres, 1915, effectively killing over 5000 Allied troops.[1] These chemical agents include chemicals from simple chlorine gas, to cyanide, and organophosphates. These CWAs ad others have been continually improved upon in efficacy of harm to persons and large scale synthesis procedures since their first production.

A. Chemical Warfare Agents

  1. Nerve Agents

Chemical warfare agents are described by many as weapons of mass destruction (WMDs) and are arguably the most brutal.[2] They are solid, liquid, or gaseous substances used with the intention of harming people, particularly in a conflict setting. These chemical agents in comparison to other WMDs are relatively easy to produce, have a low cost, and can have an enormous impact with a small amount of material. The Center for Disease Control and Prevention (CDC) categorizes these chemical agents by their effect: biotoxins, vesicants, blood agents, acids, pulmonary agents, incapacitating agents, anticoagulants, metals, nerve agents, tear gas, toxic alcohols, and vomiting agents. Among these groups of chemicals the CDC has named nerve agents as being, "the most toxic and rapidly acting of the chemical warfare agents." These are therefore, the most

important materials to have a defense against. Nerve agents belong to the organophosphates class of chemicals, which also includes many pesticides. There are two main classes of nerve agents used and studied namely G series and V series. The G series contain such nerve agents as tabun (GA), sarin (GB), and soman (GD), and the main nerve agent in the V series is VX, all shown Figure 1. Production of organophophates is not terribly complex for such harmful chemicals, thus, can be produced by persons with some basic scientific background. Production of these nerve agents can be quite similar to the production of pesticides, due to both being organophosphate derivatives. There are a vast number of journal articles and books expressing the direct synthesis route of pesticides, which can be altered to create a nerve agent.[3-5] There are even journal articles detailing the direct route to synthesizing the nerve agents, which in the paper by Reesor *et al.* there are multiple routes supplied in one article to produce sarin.[6] One of the routes from Reesor is shown Scheme 1. Despite their simplicity and low cost, the toxicity level of these compounds is incredible. Details for sarin and VX are included in Table 1.[7] LCt_{50} and LD_{50} are the time dependent lethal concentration for vapor phase and lethal dose required to kill 50 percent of those exposed, respectively. Also listed are the LCt_{50} of chlorine gas and the LD_{50} and LCt_{50} of hydrogen cyanide as comparison to show the extremely high toxicity of these nerve agents.

Table 1. Toxicity of select chemical agents.

	Sarin	VX	Chlorine (g)	Hydrogen Cyanide
$LCt_{50} \left(\frac{mg*min}{m^3} \right)$	100	10	6000	2500
$LD_{50} \left(\frac{g}{kg\ body\ weight} \right)$	.024	.14	-	95
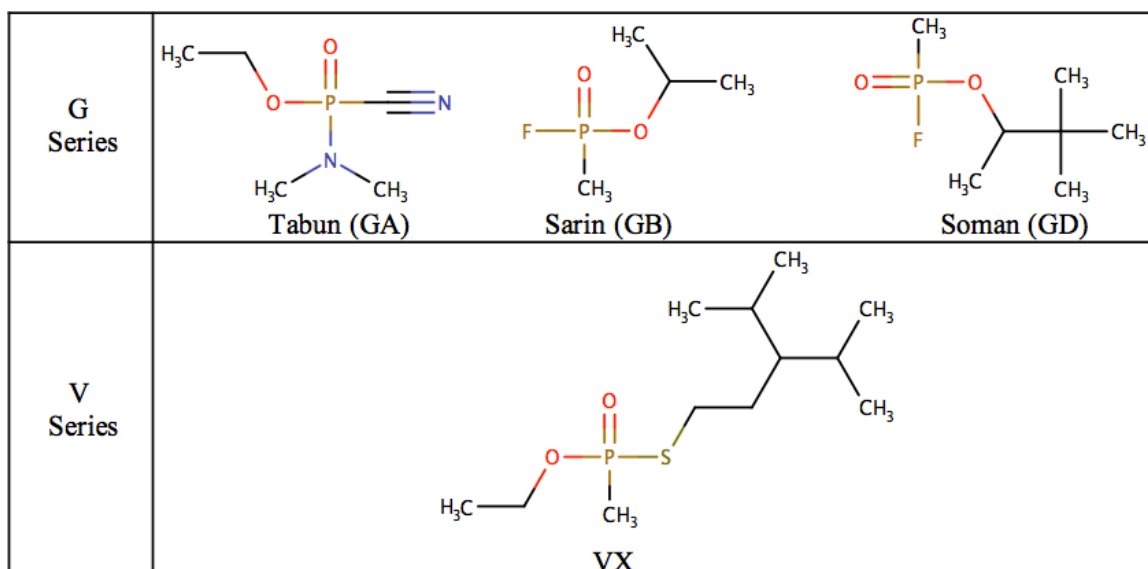
Figure 1. Structures of G and V series nerve agents.
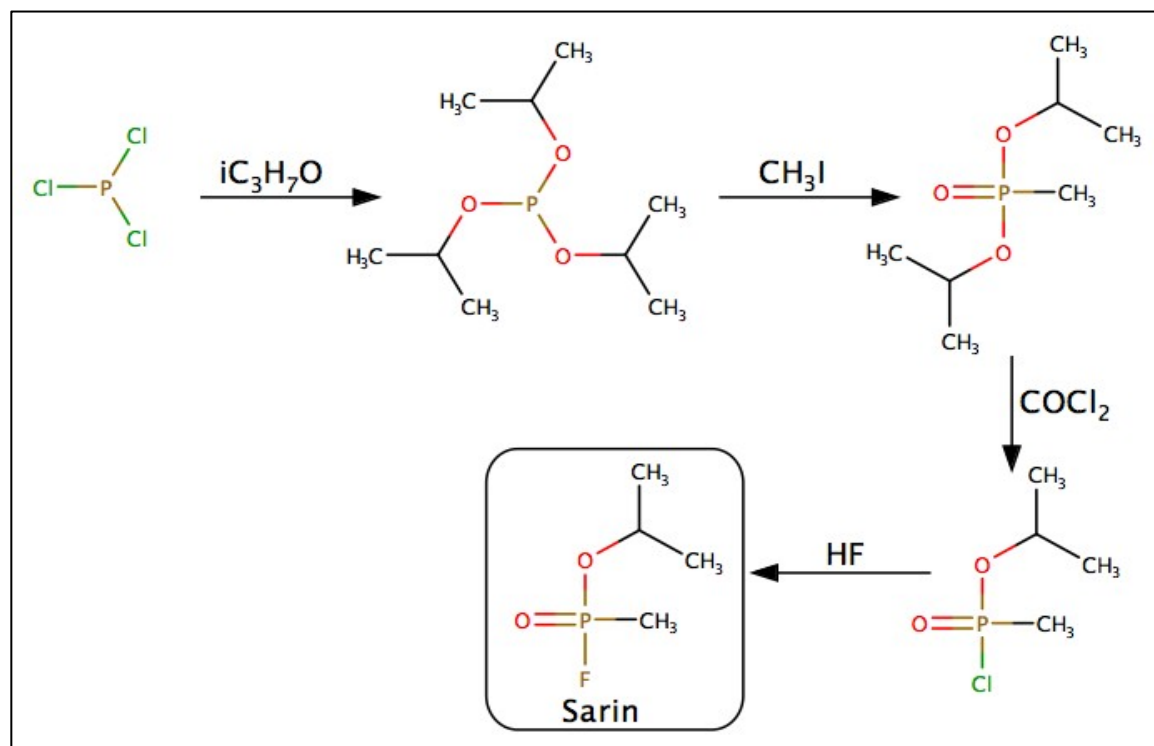
Scheme 3. Synthesis of Sarin gas (GB).

Nerve agents are acetylcholinesterase inhibitors. They function by irreversibly bonding with the enzyme, actelycholinesterase, which is responsible for cleaving the bond between neurotransmitter acetylcholine and its muscle cell receptor. This effectively inhibits the separation of acetylcholine from the muscle cell receptor and

causes the muscle cell to receive continuous signal to activate, which has dire effects

including: constriction of airways, decreased heart rate and blood pressure, muscular

twitches and cramps, cardiac arrhythmia, and seizures.[2,8-9] Depending on the nerve agent

and the phase it is in, uptake can be pulmonary, transdermal, or absorption through the

eyes. Recent examples of the use of nerve agents include: nearly 100 killed in Syria from

sarin (April 4, 2017), the assassination Kim Jong-Nam (February 13, 2017), the exiled

half brother of Kim Jong-Un, using VX, 1400 people killed in Syria by Sarin gas (August

21, 2013), and the Tokyo subway bomb deploying Sarin gas killing 13 and injuring 6000

(March 20, 1995).

The most common form of protection from these nerve agents is gas masks and

chemical suits, which then need to rapidly be placed on when exposure occurs. Apart

from this delayed preventative measure there is not much in the means of defense. There

is a two part injection treatment of atropine and 2-PAM, which acts as a multi-process

repair of the synapse function. The atropine inhibits muscle receptor sites from further

binding with ACh and the 2-PAM cleaves the bond of acetylcholinesterase and the nerve

agent. This 2-part injection sequence needs to be administered within hours of exposure

in order to completely nullify the effects of the nerve agent. Apart from being time

sensitive and requiring an injection the anti-agent treatment can also lead to negative side

effects including brain damage. The potential benefit to the military and civilians for the

advances made from the research described here is a powerful response mechanism to

terror threats and protection of personnel in conflict areas.

2. CWA Simulants

Most research facilities are not equipped to handle the toxicity of actual chemical warfare agents so simulants are commonly used. By far the most commonly used nerve agent simulant in literature is dimethyl methylphosphonate (DMMP), first cited by Jonas et al.[10] The draw of this compound is that it is non-toxic to humans but still is an organophosphate like the nerve agents, shown Figure 2. The draw of DMMP is also its shortcoming, the toxicity in a nerve agent is dependent on having an electron withdrawing group replacing one of the methoxy groups attached to the phosphorous, i.e. nitride for tabun, fluoride for sarin and soman, and sulfide for VX. It should be noted that that in comparing the mechanism of interaction between Sarin and DMMP it has been shown that though somewhat electronically different molecules the reaction mechanisms and energies seem to be generally similar, indicating DMMP as a fine simulant for nerve agents.[11] This finding very well may not hold true in interactions with every type of decontamination material, thus, needs to be considered a source of potential error.
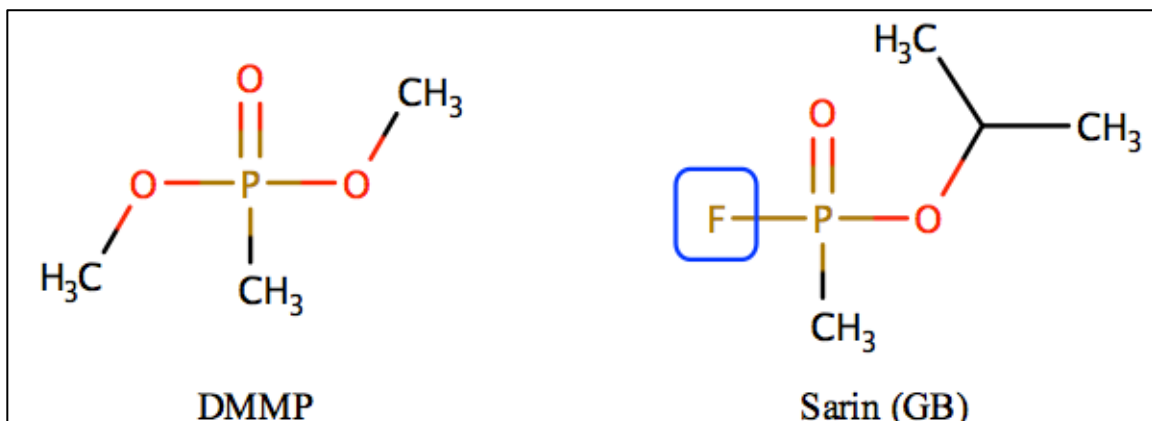
Figure 2. Comparison of simulant DMMP with nerve agent Sarin.

B. Multifunctional Materials

  1. Zirconium Hydroxide

Much work has been done studying the effectiveness of certain metal oxides for adsorption/decomposition of CWAs and Toxic Industrial Compounds (TICs). Chemical warfare agents on metal oxides particularly have a high number of studies both theoretical and experimental. Aluminum oxide[12-15], magnesium oxide[14,16], silicone dioxide[17,18], and titanium oxide[19,20] have been extensively studied by various groups and concluded to be, in gas-solid heterogeneous interactions, reactive adsorbents for DMMP with surface poisoning causing the cessation of the decontamination or further adsorption. Mitchell *et al.* have done much work with metal oxide supported/impregnated metal oxide, i.e. alumina supported iron oxide, and has shown varying degrees of success with decontamination and adsorption.[15, 21-23] These many experiments have been conducted at varying temperatures from room temperature to extremely high, in different atmospheres including: vacuum, atmospheric, high and low humidity, under flow of N_2, inclusion of ozone, and others.[24,25] The techniques with the exception of ozone, have shown varying degrees a success but all culminate with the material active sites experiencing surface poisoning via covalent bond formation with the phosphorous containing fragment causing the reaction to be stoichiometric rather than catalytic.

Recently zirconium hydroxide has become a material of particular interest due to articles showing high reactivity with certain toxic compounds. VX, arguably the most toxic nerve agent to date, has been reported to be decomposed by $Zr(OH)_4$ with less than a minute half life by Bandosz *et al.* making it the material with the fastest decomposition rate to date.[26] Bandosz reported that it was necessary to increase the standard

concentration used in these liquid agent-solid $Zr(OH)_4$ experiments in order to get results because the reaction occurred too quickly. Peterson *et al.* showed reaction of SO_2 with $Zr(OH)_4$ to be an adsorption mechanism with up to 110 mg SO_2/g $Zr(OH)_4$, which is much greater than that of activated carbon impregnated with CuO despite only ~10 % of the $Zr(OH)_4$ sites reacting.[27,28] In another study by Peterson *et al.* removal of cyanogen chloride was tested and was shown to be more effective than traditional impregnated activated carbon.[29] Removal of chlorine-containing gases with $Zr(OH)_4$ was shown to be effective for HCl, Cl_2, and $COCl_2$ specifically by terminal hydroxides of the $Zr(OH)_4$.[30]

Zirconium hydroxide is a polymorphic metal (hydr)oxide. A molecular dynamics simulation of the amorphous material is depicted Figure 3, courtesy of Ivan Iordanov from the Naval Research Laboratory. Figure 3a is a monomer of the $Zr(OH)_4$ structure which was found to be an insufficient model to describe the chemistry seen experimentally. Figure 3b and 3c are different angles of an optimized monolayer of $Zr(OH)_4$. What can be noticed about the zirconium polymorph is that the zirconium atoms are all highly coordinated species, ranging from 4 - 6 coordinated atoms, which creates a lot more potentially reactive sites than typical metal oxides. Figure 3d is an optimized representation of multilayer $Zr(OH)_4$ system. It should be noted that in this molecular dynamics optimized multilayer representation there are two distinct monolayers interacting only by hydrogen bonding. This seems highly unlikely and the structure would more probably propagate in three dimensions so that there would be chemical bonds between the "layers". However, there is literature support for the distinct monolayer formation depiction in an article discussing a $Zr(OH)_4$ material capable of reversibly converting between sol and gel phase.[31] The gel phase is descried as tetramers

coalescing by forming bridging hydroxyls in sheet like fashion propagating in 2 dimensions where each zirconium atom is coordinated to 4 other zirconium atoms, which is what is predicted from the calculations. What is important to notice about this structure is that unlike most metal oxides that have repeating metal-oxygen bonds with a varying degree of terminal hydroxide groups bound to the metal and few hydrogenated bridging oxygens, the $Zr(OH)_4$ is a network of entirely Zr-OH bonds: terminal, bridging, and aqua (H_2O). The key point and the proposed source of the reactivity comes from all of the oxygens being hydrogenated. $Zr(OH)_4$ has been to have 5 distinct types of OH bound included in the structure.[25] These sites are depicted schematically Figure 4.
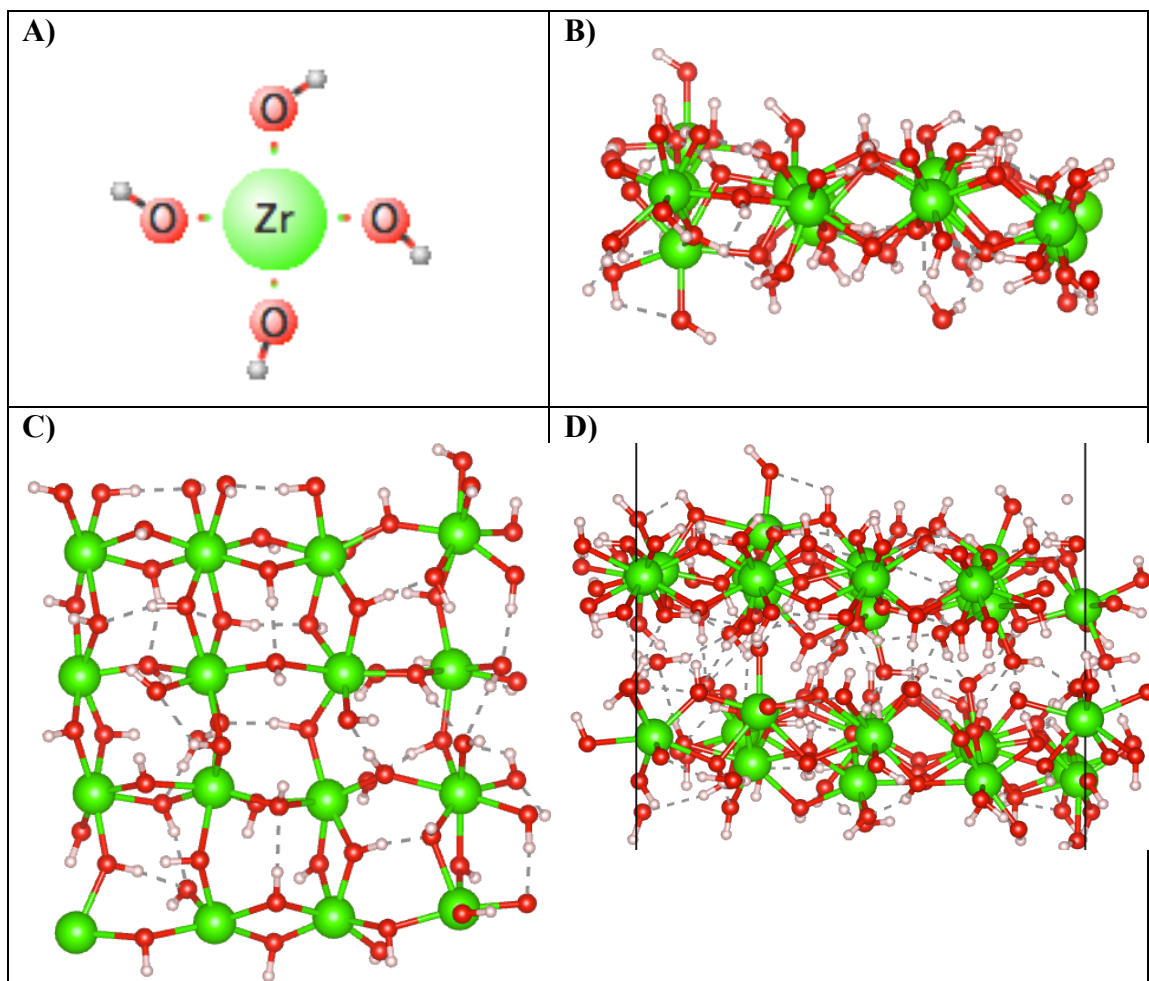
Figure 3. Molecular dynamics simulation of $Zr(OH)_4$ structure.[75]
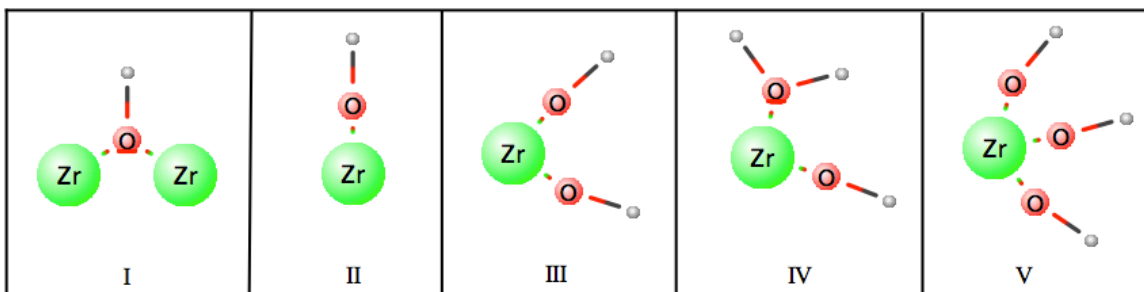
Figure 4. Hydroxyl species present on Zr(OH)₄.

Depending on the method and materials used to create the particular zirconium hydroxide, of which the suppliers provide limited information, the characteristics of the solid can be quite different. The general procedure for producing $Zr(OH)_4$ is to precipitate it out of a zirconium salt solution by adding a base. In literature the most common salt used for this is the highly water soluble zirconyl oxychloride octahydrate, $ZrOCl_2 \cdot 8H_2O$.[32-44] The dissolved zirconyl oxychloride is a quite acidic solution with a pH=1.7.[32] A pH of 3 has been shown to be sufficient of precipitating the $Zr(OH)_4$ out of solution.[32] It has been reported that the pH at which the $Zr(OH)_4$ is precipitated out at causes differences in the material and is most likely the root of the non-disclosed differences from the suppliers.[28] The difference between the types of zirconium hydroxide produced causes different reactivities to be observed. This difference, however, seems not to come from chemically different substrates, meaning all of the types have the same characteristic highly coordinated zirconium atoms bound to monodentate/terminal (*t*-OH) and bidentate/bridging hydroxides (*b*-OH) with each oxygen being hydrogenated. The difference comes in the conformation these bonds make causing higher or lower surface areas and more importantly higher or lower pore volumes. If the pore volumes are small then there is limited access to the reactive sites, which would cause lower reactivity. These conclusions have been proposed in work from Edgewood Chemical and Biological Center (ECBC) comparing reactivities of "type B" and "type C" $Zr(OH)_4$. SEM images,

9

provided by ECBC, of the two types are shown in Figure 5. Type B forms small crystallites agglomerated into larger areas. Type C is characterized by much larger spherical particles. The surface area of "type B" due to being composed of small crystallites is much higher than that of "type C" which leads to the higher reactivity of the "type B" $Zr(OH)_4$.
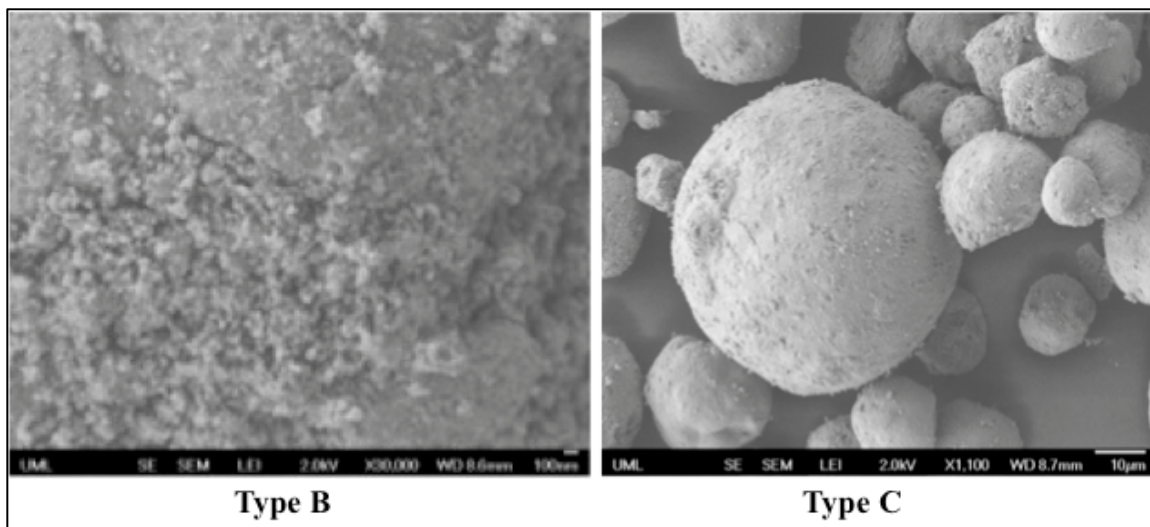
Figure 5. SEM images of different $Zr(OH)_4$ types.

The draw back with using metal (hydr)oxides and many other materials for this degradation of nerve agents, is that, as previously discussed the reaction is stoichiometric not catalytic. The process has potentially more aptly been described as reactive adsorption with surface poisoning, meaning that the nerve agent decomposes but leaves the phosphoryl group strongly bound to the surface at the active sites, effectively inhibiting any further reaction, and the removal of this requires a tremendous amount of energy. This drawback is the reason that research in this area is still extremely critical. What is desired is a material possible of true heterogeneous catalysis of these toxic compounds.

2. Metal-Organic Frameworks

Metal-organic frameworks, MOFs, have been materials of particular interest to chemist interested in metal/metal oxide chemistry since around 2000 due to the potential increased activity over traditional metal/metal oxides because of greatly increased surface areas. A MOF is composed of two parts, organic ligands which connect secondary binding units (SBU), which are metal or metal (hydr)oxide cores, leading to formation of a large supramolecular structures. In 2014 DeCoste and Peterson cited that there were upwards of 6000 MOFs registered in the Cambridge Structural Database.[35] There has been great interest for MOFs in the areas of gas storage[36-39], catalysis[40-42], filtration[35,43], and sensors[44]. It is a well-known tendency that as surface area of a metal oxide increases the reactivity increases proportionally among the same type of metal oxide, due to more active sites being accessible to the compound of interest. Since organic linkers in a MOF separate the SBUs, the surface area can be dramatically larger than a traditional metal (hydr)oxide, while essentially using metal oxide chemistry. The idea behind using these MOFs for the decontamination research rather than traditional metal oxides stems from the understanding that the massive increase in surface area potentially provided by MOFs will enhance efficiency of the reaction. Further increase or decrease in surface area and pore volume as well as addition of functional groups are easily manipulated by varying the organic linker used in their synthesis. For example in the case of the current research the SBU, $Zr_6O_4(OH)_4$, is the same for UiO-66, UiO-66-NH_2, UiO-67, and MOF-808. The difference between the MOFs structures is solely caused by the organic linker, benzene dicarboxylate (BDC), 2-amino-benzen dicarboxylate (BDC-NH_2), biphenyl dicarboxylate (BPDC), and benzene- 1,3,5-tricarboxylate (BTC) respectively, all shown Figure 6.

11

The SBU of the MOF family studied in the current research is $Zr_6(\mu_3\text{-}O)_4(\mu_3\text{-}OH)_4$ [μ_3 = bridging], a hexanuclear zirconium (hydr)oxide with each zirconium atom bound to two bridging oxygen (μ_3-O) and two bridging hydroxyl (μ_3-OH) groups, forming an octahedron, shown Figure 7.[45,46] Figures 7-10 are courtesy of Dr. Diego Troya.[105] The UiO family, a subset of the Zr_6 node containing MOFs, has an isoreticular topography that has a face centered cubic geometry.[47] The orientation of the necessary 12 ligands around the SBU, shown in Figure 8, to balance the charge of the SBU causes the supramolecular structure to be composed of two distinct types of cavities, a large octahedral, Figure 7c, which is capped on all sides by tetrathedral cavities, Figure 7b. The supramolecular structure of UiO-66 and UiO-67 are shown Figure 9 to show the effect of substituting the larger linker BPDC in UiO-67.
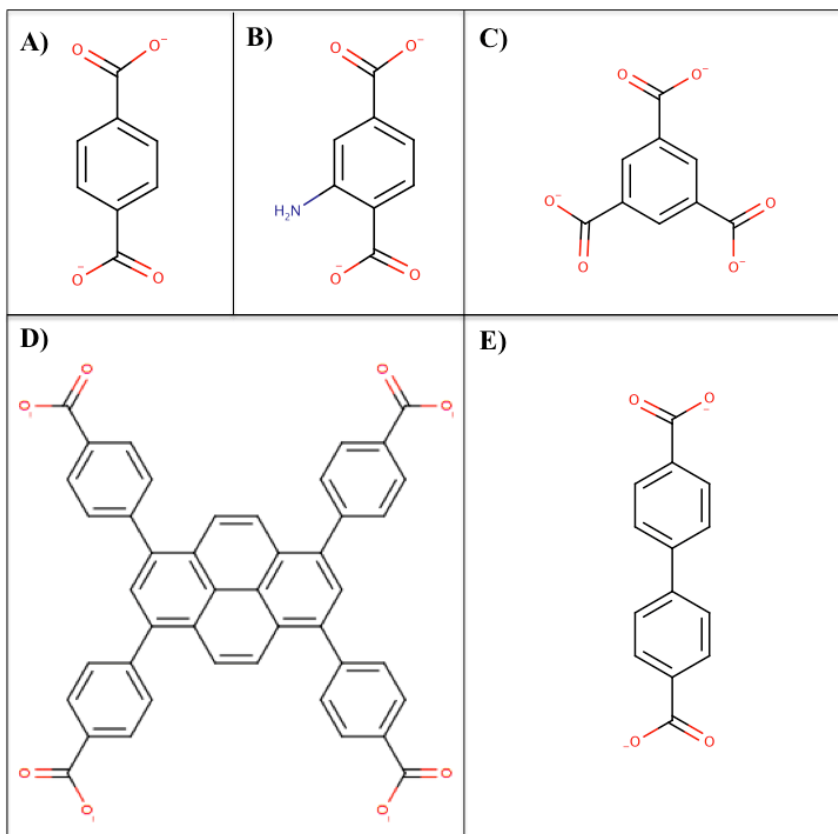
Figure 6. Organic linkers BDC (A), BDC-NH$_2$ (B), BTC (C), TBAPy^{4-} (D) and BPDC (E) for UiO-66, UiO-66-NH$_2$, MOF-808, NU-1000, and UiO-67 respectively.
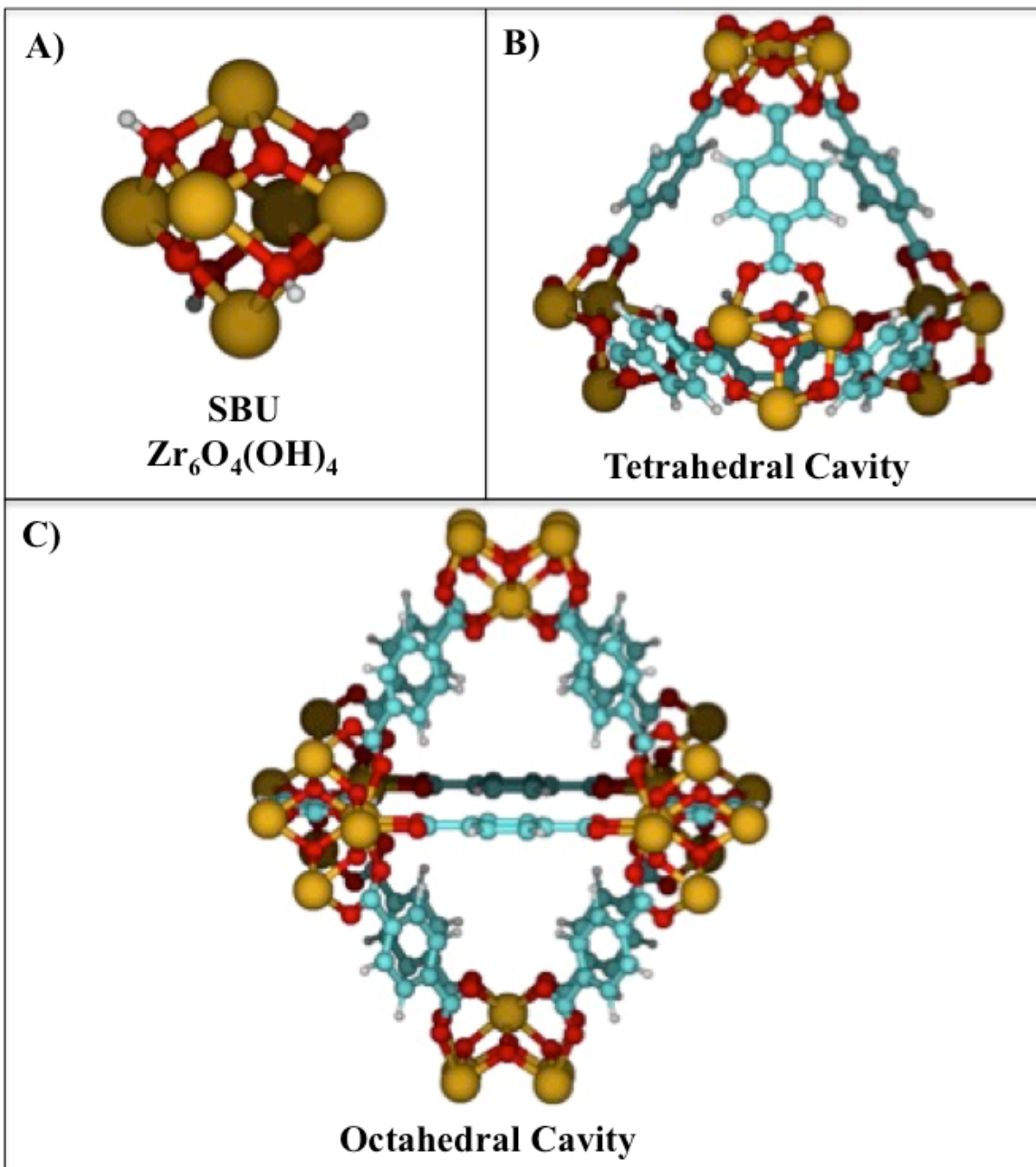
Figure 7. MOF family, UiO, SBU (A) and cavaties (B and C) formed in supramolecular structure.

The other main two MOFs studied with the Zr_6 node are NU-1000 and MOF-808. The geometries of the linkers force the node to have lower coordination of the SBU to the linkers, thus, different topology from the UiO subset. This is quite simply due to the structural arrangement caused by the linkers, 1,3,6,8-tetrakis(p-benzoate)pyrene [TBA-Py^{4-}] and BTC which are non-linear, compared to the linear linkers of the UiO series. The

coordination for NU-1000 and MOF-808 is reduced to 8 fold and 6 fold respectively.[48,49]

The importance of this lower coordination upon use of modulators and thermal treatment

is addressed later. The reason for this series of MOFs having such high interest is due to

the exceptional thermal, chemical, and mechanical stability of the structure along with

their potential reactivity.[47,50]
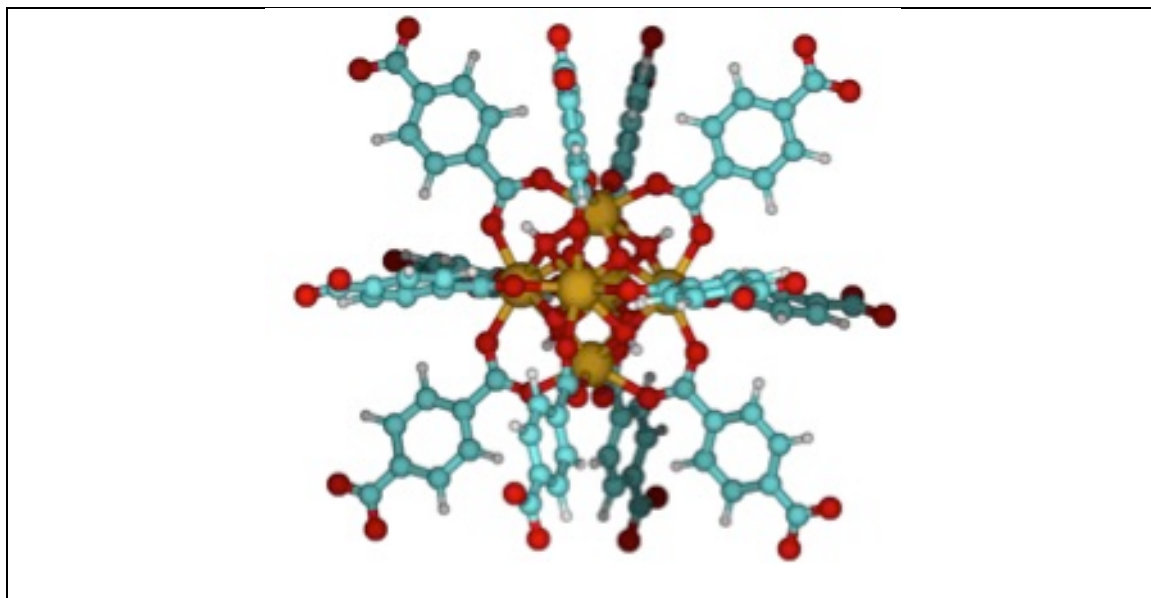
Figure 8. One UiO-66 SBU fully coordinated to 12 BDC linkers.
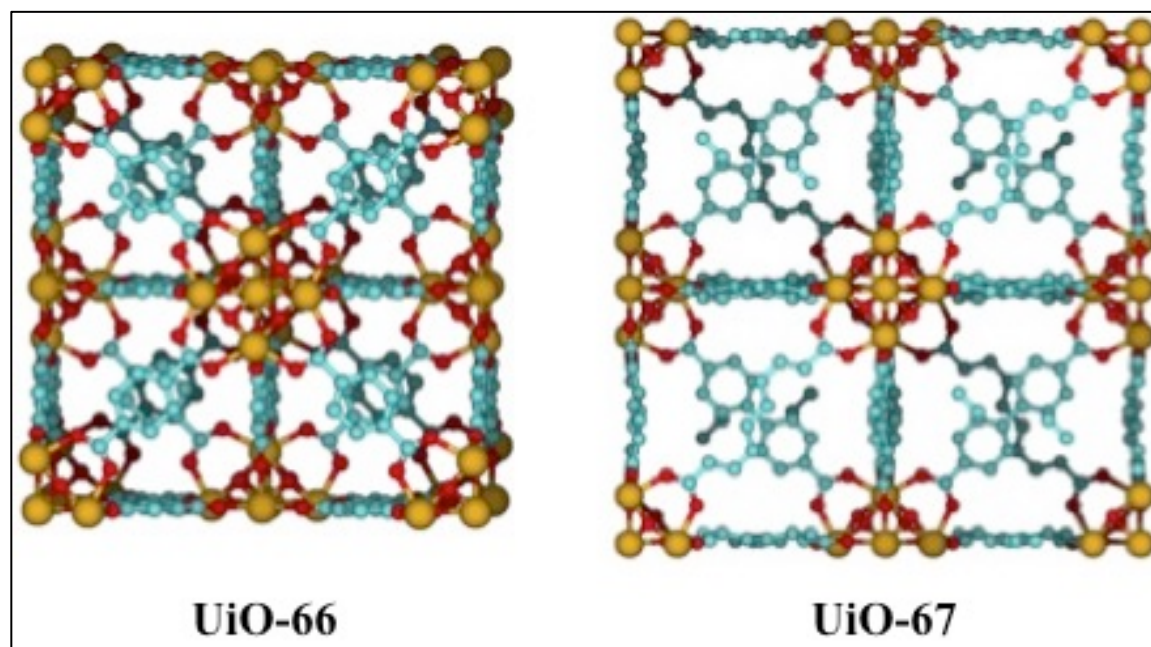
Figure 9. Supramolecular structure of UiO-66 and UiO-67.
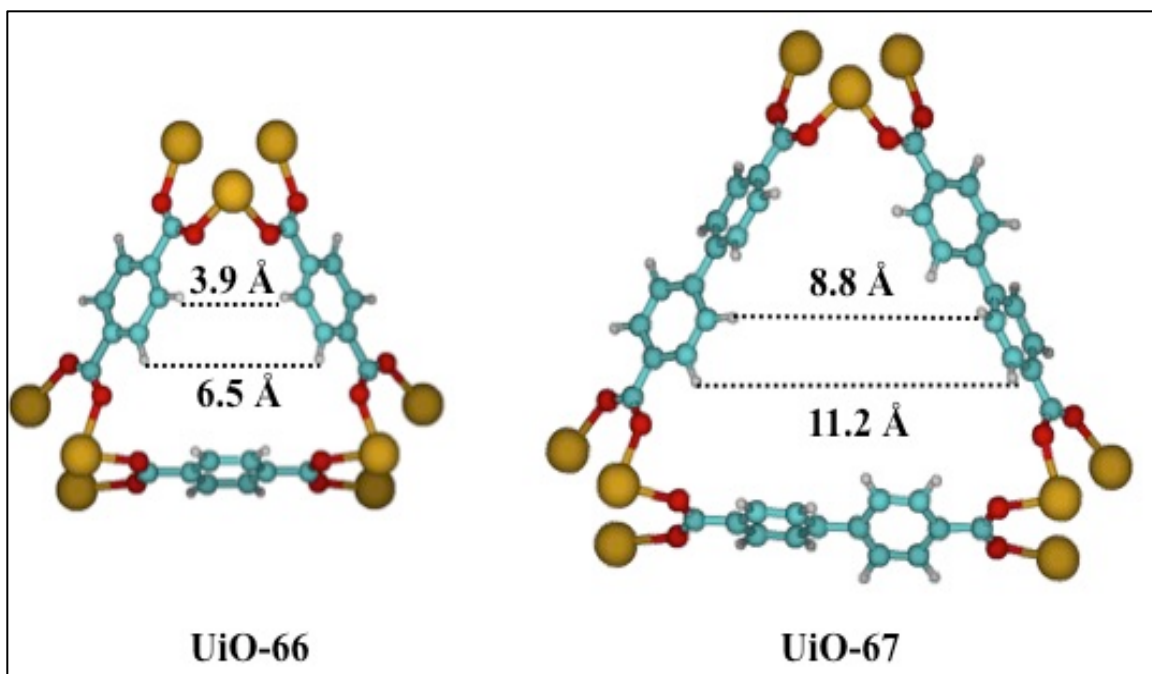
Figure 10. Pore size comparison of UiO-66 (A) and UiO-67 (B).

What has been shown is that pristine UiO-66 is non-reactive with nerve agent simulants.[51] The MOF is able to physiosorb the simulants but due to the high coordination of the Zr atoms there is no reactive site available to induce a reaction, whereas including defect sites has shown increased activity by Moon *et al.*[49,52] What is necessary for reaction of this series of MOFs are under saturated Zr sites.[49] These unsaturated, "defect", sites allow interaction of compounds of interest with the SBU due to leaving a metal site accessible for reaction. There is a well-developed technique of using modulators to reduce the coordination of UiO-66 to varying extents in order to make it more active.[53,54] The modulator can be another organic component which is monotopic as to form no bridge to another SBU or inorganic such as H_2O or HCl. This under coordinating technique seems to be unnecessary with UiO-67 because following the same synthesis route as the pristine UiO-66 leads to higher percentage of defect sites on the UiO-67. Consequently, under-coordinating the SBU in the UiO to enhance the

reactivity also reduces the stability of the supramolecular structure.[47] With that in mind,

UiO-66 and UiO-66-NH$_2$ seem to have a much longer shelf life compared to UiO-67.

Keeping the under coordination concept in mind there seems to be an advantage in using

NU-1000 and MOF-808 rather than the UiO series due to the Zr atoms being under-

coordinated without exhibiting the reduction in stability.[49] Synthesis of the UiO series of

MOFs is a solvothermal condition mixture of equimolar zirconium salt and organic linker

dissolved in DMF. The synthesis of MOF-808 is similar to preparation of defective UiO-

66, which uses varying modulators such as acetic acid for charge compensation. MOF-

808 uses an equivalent volumetric ratio of DMF to formic acid in the synthesis along

with equivalent molar ratio of ZrOCl$_2$:BTC linker.[55] The formic acid acts as a modulator

to form the topology desired but can later be removed by thermal treatment.[56] Since the

structures of NU-1000 and MOF-808 have dramatically larger pore volumes and contain

inherently under-coordinated Zr sites, the reaction probability is much higher than the

UiO series.

The ultimate goal of this research effort is development of multifunctional

materials capable of protection against many harmful materials, including nerve agents

addressed in the present study. The ideal application is not limited to either military or

industrial, but applicable to both. Research has demonstrated the effectiveness of metal

(hydr)oxides but more work is possible in that regard. MOFs are a relatively new class of

compounds and further testing is still needed but the indications thus far are quite

promising. With the metal (hydr)oxides reaction with nerve agents it seems to be

improbable that changing the reaction from stoichiometric to catalytic will happen due to

the strong binding of the surface phosphate groups. The MOFs bring some hope into this

aspect as the functionalization of the linkers could potentially lower that binding energy

enough that it could be removed. In terms of other harmful compounds besides nerve

agents the MOFs as well as the metal (hydr)oxides seem very promising.

CHAPTER II. MATERIALS AND METHODS

A. Infrared Experiments

  1. Diffuse Reflectance Infrared Fourier Transform Spectroscopy

    a. Background and Theory

  Diffuse Reflectance Infrared Fourier Transform Spectroscopy (DRIFTS), is a powerful infrared spectroscopy tool used to look at non-transparent materials. DRIFTS systems have several significant advantages over the transmission infrared systems commonly used including simpler sample preparation, analysis of non-transparent samples and irregular surfaces, and detailed *in situ* studies of reactions on surfaces. The information from diffuse reflectance is obtained in a different manner than traditional transmission infrared yet produces comparable data. When an incident beam of radiation strikes a surface it has a few possibilities as to the outcome. The radiation can either be reflected at an angle proportional to the incident beam dependent on refractive index of the material (specular reflection), Figure 11a, transmitted and adsorbed by a particle, Figure 11b, or diffused through the sample by a series of reflection off of particles, Figure 11c. The latter of these is the information a DRIFTS system takes advantage of. The incident beam strikes a particle on the surface and is reflected multiple times through and off of particles of the top few layers of the material with some beams finally being directed toward the detector for analysis.
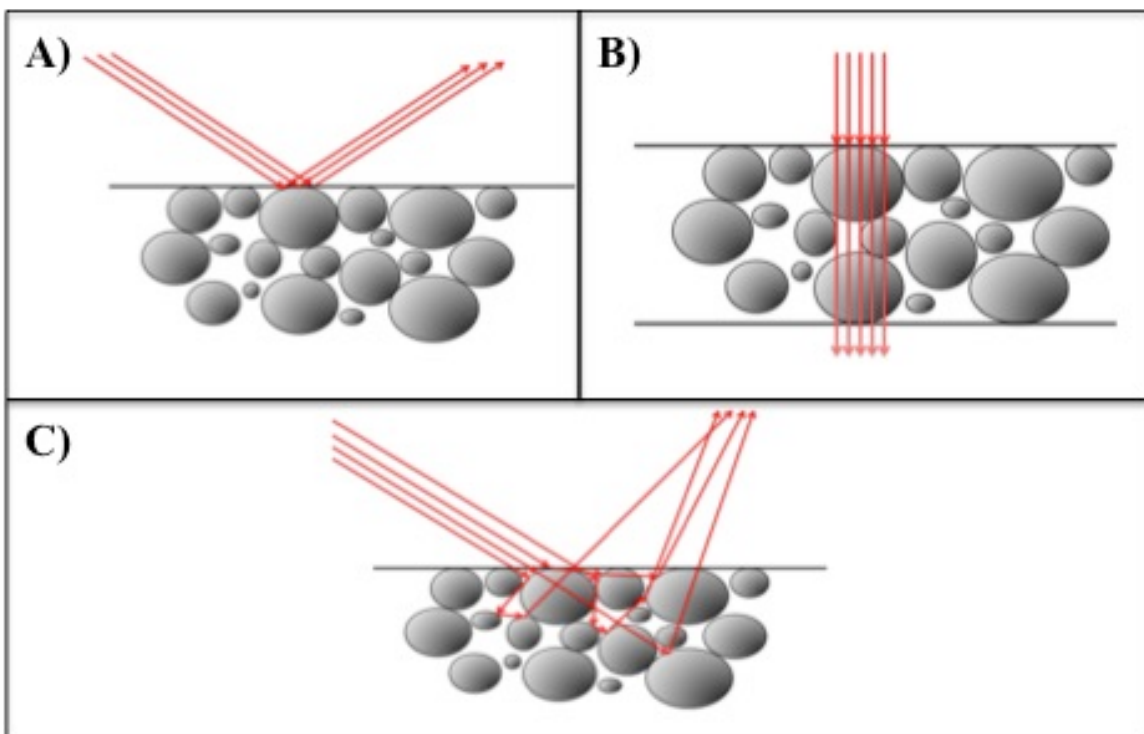
Figure 11. Infrared (A) Specular Reflection, (B) Transmission, and (C) Diffuse Reflectance.

The most commonly used theory in describing diffuse reflectance spectra was developed by Kubelka and Munk, derived from a model in which a sample is of sufficient thickness such that further increasing sample thickness does not change the reemission of the radiation.[57] The radiation field can be described by two fluxes, from the illuminated surface toward the unilluminated surface and from the unilluminated surface back toward the illuminated surface. This theory takes into account absorption and scattering of the infrared radiation and thickness of the sample. The Kubelka-Munk function, $f(R_\infty) = \frac{(1-R_\infty)^2}{2R_\infty} = \frac{K}{S}$, where R is the reflectance, K is the absorbance coefficient, and S is the scattering coefficient is derived from this theory.[57]

This theory seems to be quite adequate for describing substances meeting certain criteria, one of which being with the sample having high reflectivity, R = 0.6-1. In this case it is possible to construct the formula $C = ZR_\infty$, where C is the concentration and Z

is a constant.[57] However, in the case of observing an adsorbate reacting on the surface of a sample matrix rather than the sample matrix itself, if the adsorbate is poorly absorbing (R' > 0.6), as is in the case with the reaction of DMMP, the $log\left(\frac{1}{R'}\right)$ transform is most proportional to concentration, shown in depth by Sirita *et al.*[58] Olinger and Griffith described that if the sample matrix, typically the metal oxide support in the catalytic investigations, is strongly absorbing, the transform that corresponds most closely to concentration for a solute is $log\left(\frac{1}{R'}\right)$ rather the Kubelka-Munk function.[59] $Log\left(\frac{1}{R'}\right)$ is used analogously to the manner in which transmittance relates to absorbance, $A = log\left(\frac{1}{T}\right)$, thus, using this analogy $A' = log\left(\frac{1}{R'}\right)$, where A' is the "absorbance" of the sample. Since $A = \varepsilon bc$; $C = \frac{A'}{\varepsilon b} = KA' = K * log\left(\frac{1}{R'}\right)$ which makes concentration directly proportional to the $log\left(\frac{1}{R'}\right)$ value. It is necessary to state that $R' \neq R$ but $R' = \frac{I_{sur+ads}}{I_{sur}}$, where $I_{sur+ads}$ is the intensity of the IR radiation after encountering the surface with adsorbate present and I_{sur}, is the intensity of the IR radiation after encountering the surface without the adsorbate present, and $R = \frac{I_{sur}}{I_0}$, where I_0 is obtained using a completely reflective mirror.[57]

b. Setup

The DRIFTS setup used in the current work can be seen Figure 12. The setup is centered around the DRIFTS cell, the Harrick Scientific praying mantis diffuse reflectance accessory which is placed in the sample chamber a Thermo Scientific Nicolet 6700 Infrared Spectrometer, equipped with a deuterated triglycine sulfate (DTGS)

detector. A high temperature reaction chamber is the most critical portion of the DRIFTS accessory. The reaction chamber is a stage with a sample cup, 5mm wide, in the center, covered by a removable stainless steel dome with three 10 mm windows, one quartz for physical viewing of the sample, the other two NaCl for transmission of the IR beam. The dome itself sits on top of the main body of the chamber sealed with an o-ring and tightened with two brackets. Once the dome is in place and tightened the chamber is evacuated via a turbo molecular pump, Leybold TMP-50 with a flow rate of 50 L/sec, backed with a mechanical pump, UL-VAC GLD-136, to pressure of 1-5 millitorr, dependent on sample, after sitting overnight. The reaction chamber is capable of being heated by cartridge heater from a power supply and monitored with a K type thermocouple. The thermocouple measures the temperature of the sample post just under the sample, not inside of the powder so it is necessary to allow adequate time for equilibration of the temperature of the sample with that of the sample cup. The sample chamber has three available input/output connections, one of which goes to the vacuum, one goes to the gas vacuum manifold, the last is currently capped. Samples are placed into the sample cup and evacuated with the mechanical pump under a flow of UHP N_2 at 20-50 torr in the cell for 2 hours, followed by evacuation with the turbo molecular pump overnight. The gas vacuum manifold, volume 2.7 L, top right portion of Figure 12b, is where any gas or gas mixture to be introduced to the powder was prepared. In detail description of the procedure of preparing and running DRIFTS experiments is in included in the standard operating procedure (SOP), Appendix A.

Liquid samples were stored in sample tubes and have been treated by a series of three freeze-pump-thaw cycles to remove high-vapor-pressure impurities prior to use.

The amount of a gas mixture at a particular concentration that can be prepared is limited by the vapor pressure of the compound. As an example, DMMP is a liquid at room temperature and has a vapor pressure of 0.7 torr at 295 K, so a typical mixture made of DMMP was a concentration of 0.6 torr/100 torr, or 0.6 %. This is a critical component of computing the amount of gas mixture we introduce at a given time, given by equation 1.

$$n_{vapor} = \left(\frac{P_{vapor}}{P_{total}}\right)\frac{(P_i - P_f)V}{RT}$$

where, n_{vapor} is the number of moles of the vapor that has been introduced to the powder, P_{vapor} is the partial pressure of the vapor in the mixture, P_{total} is the total pressure of the gas mixture of vapor in the carrier gas, P_f is the pressure at the end of each collected spectra, P_i is the initial total pressure of the gas mixture in the manifold, V is the volume, 2.7 L, R is the ideal gas constant, 62.36 $\frac{L\,Torr}{K\,mol}$, and T is the temperature in Kelvin, 294 K.

DRIFTS dosing experiments were carried out maintaining the pressure in the DRIFTS cell at 3-5 torr. Spectra collected were 250 scans at 4 cm^{-1} resolution, using a 74 mm aperture, and 0.6329 cm/s mirror velocity. Unless otherwise noted, all DRIFT spectra during reactions are represented by dividing the corresponding single beam spectrum to the first single beam spectrum collected after initiation of mixture flow through the cell. This background was chosen because of the spectral distortion that results when the gas pressure in the cell is different for the sample and background spectra, shown Figure 13. This distortion is presumed to be caused by change in index of refraction above the sample, not a change in packing/orientation of the sample, since if the flow is stopped and a spectrum of the evacuated sample is divided by the background sample, the resulting reflectance spectrum shows no distortion.
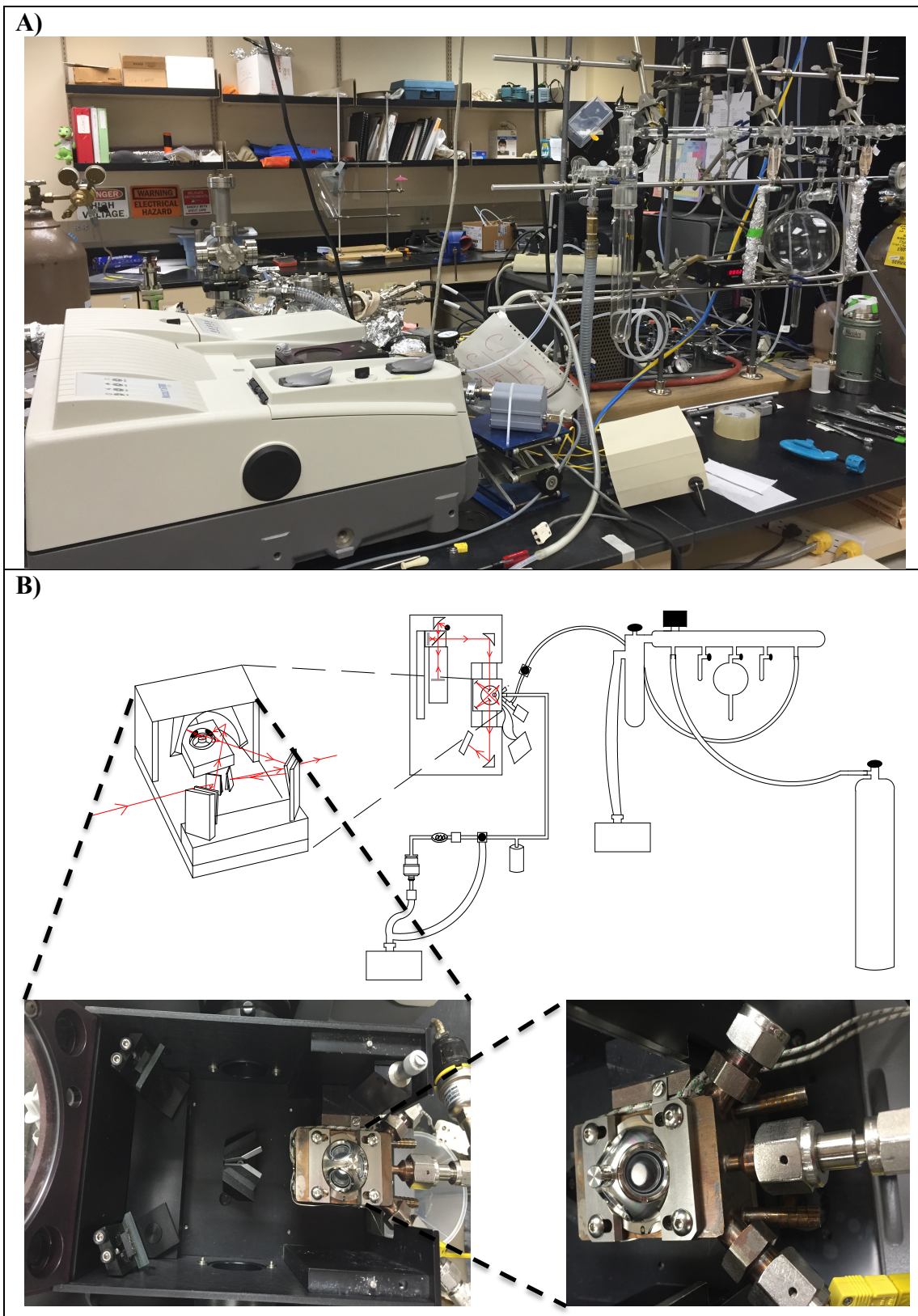
Figure 12. DRIFTS setup: (A) image, and (B) schematic.
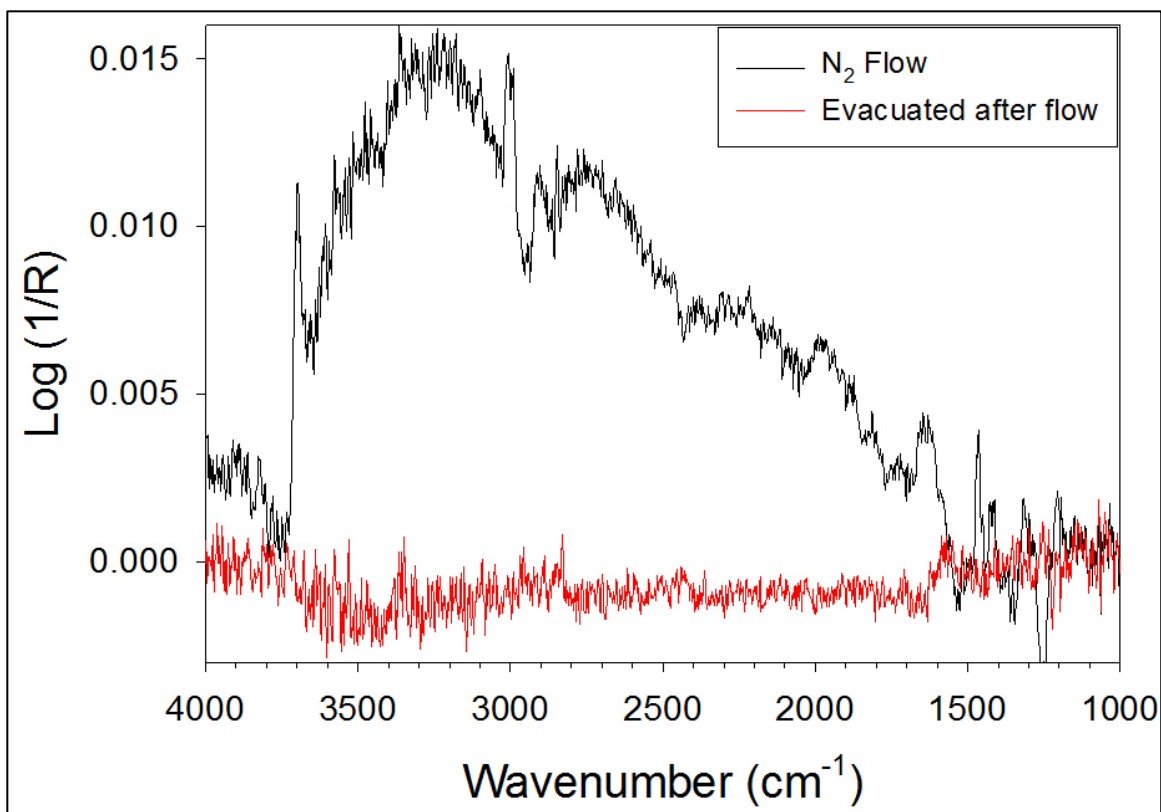
Figure 13. Spectral distortion caused by flow in the DRIFTS cell.

2. Micro reactor

      The other infrared technique that was used to study the catalysis reaction was a

micro reactor system, Figure 14. The data collected is from a Thermo Scientific Nicolet

360 FTIR equipped with a long path gas cell and a DTGS detector. Spectra collected

were 32 scans at 4 cm^{-1} resolution with a 100 mm aperture and 0.6329 cm/s mirror

velocity. The long mini long path gas cell has an effective path length of 2.4 m. The

effective path length is achieved by a series of 24 reflections at either end of the cell

before exiting and going to the detector. The reason this long path length is desired is

because in the setup, concentrations of the analytes are very small compared to the carrier

gas and since absorbance is known to be directly proportional to path length from the

Beer-Lambert Law A=εbc, where A is the absorbance, ε is the molar absorptivity in

$\frac{L}{mol*cm}$, b is the path length of the beam through the gas, cm, and c is the concentration of the gas, mol/L, it is seen that a greater absorbance is obtained with longer path length. The infrared system is positioned downstream from the flow reactor setup, which consists of a reaction stainless steel U-tube that houses the powder sample. A bubbler containing liquid DMMP precedes the U-tube. Flowing a carrier gas through the bubbler, pure N_2 at 10 mL/min in these experiments, results in the gas mixture. The bubbler has two porous disks that help to saturate the flow. The U-tube is placed inside of a furnace so that reactions can be run at temperatures from room temperatures up to 500 ^{o}C. One three-way ball valve directs UHP N_2 flow either through the bubbler or through a bubbler bypass, used for purging the sample prior to dosing DMMP. The opposite side of the bubbler and the end of the bypass both have quarter turn plug valves to ensure appropriate flow direction. Control of the carrier gas flow rates is established through a calibrated Teledyne mass flow controller (MFC) upstream of the bubbler.

What this setup accomplishes is that gas phase products from the reaction can be monitored and identified, the breakthrough time of the vapor adsorbing on the solid can be determined, and amount per gram or amount per unit surface area adsorbed or reacted on the solid can be determined. The long path gas cell accessory on the infrared spectrometer measures absorbance of the gas phase compounds coming from the micro reactor. This data is very clear in identifying what gas phase products come from the reaction whether there is decomposition at the powder, adsorption, both, or neither. The concentration of the gas mixture in this setup is dependent on the carrier gas flow rate into the bubbler, and a constant rate of 10 mL/min was used.

A)

B)
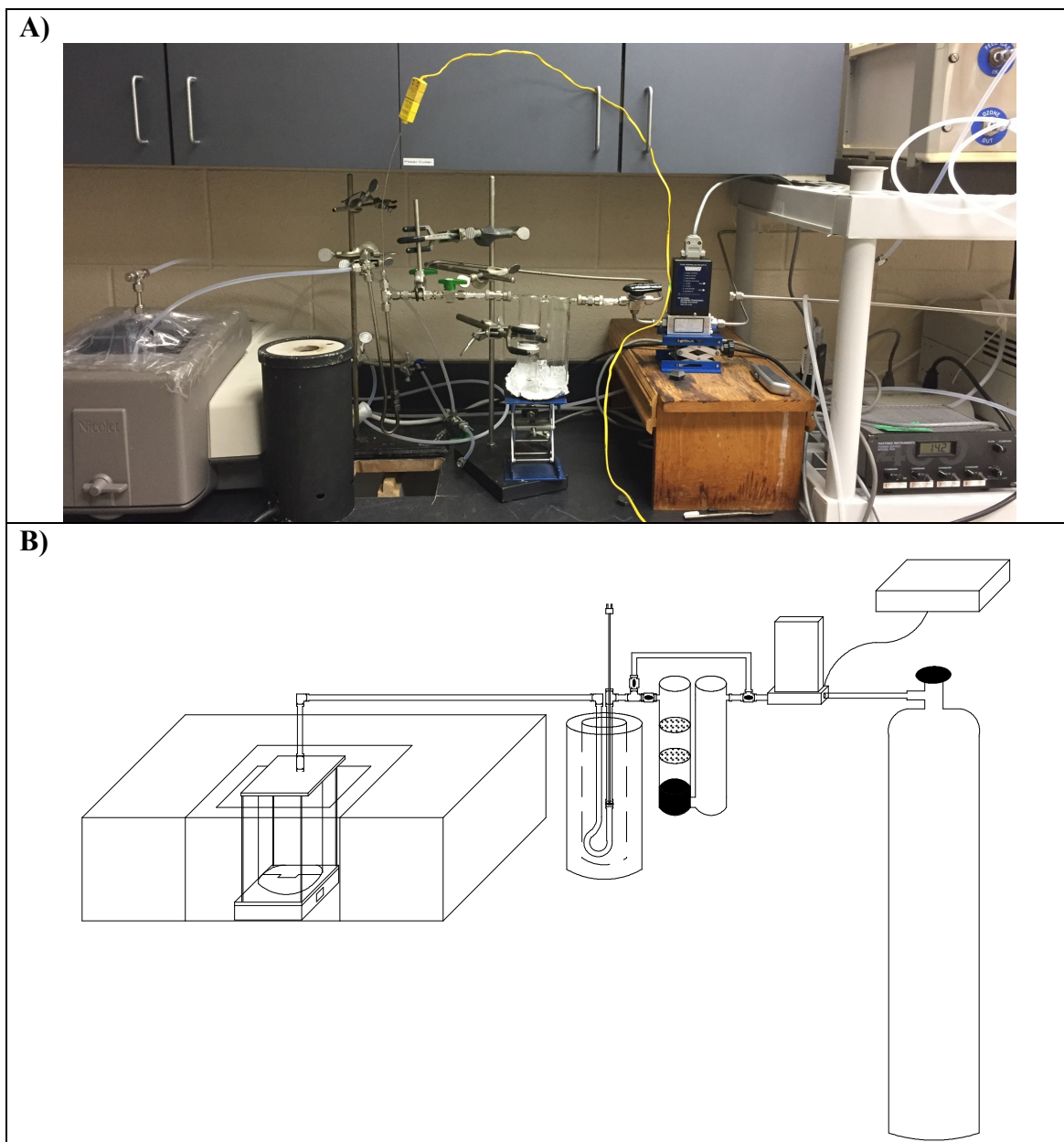
Figure 14. Microreactor setup: (A) image, and (B) schematic

Certain control experiments were conducted in order to gain quantitative results of the reaction of DMMP with the materials. First a Beer's Law standard curve for methanol, Figure 15, a common decomposition product of DMMP, was produced by flowing varying concentrations of methanol (MeOH) in N_2 through the system and recording the integrated area of the P branch of the C-O stretch at 1013 cm^{-1} once it reached equilibrium. This was accomplished using a gas mixture from Praxair of 0.104 %

MeOH in N_2 at a constant flow rate of 10 mL/min which was then diluted with an additional flow of N_2 at varying rates. Secondly, DMMP flow rate was determined using a condensing chamber submerged in an ice bath of dry ice in ethanol with the flow of N_2 through the bubbler containing the DMMP at 10 mL/min. The flow rate of DMMP was found to be 0.5 µmol/min. Last, in order to measure breakthrough time of DMMP through $Zr(OH)_4$ the amount of time it takes for DMMP to flow through an empty cell must be considered and subtracted out. The preparation was exactly as used in experiment with no $Zr(OH)_4$ sample in the microreactor, the flow of DMMP was started and spectra were collected continuously until emergence of DMMP was seen. Constructing a line graph of 1275 cm^{-1} peak height vs. time and calculating the x-intercept from the first ten spectra with visible peaks determined the baseline breakthrough time with no sample which is used as a delay and must be subtracted out, Figure 16. This test was also used as a confirmation that no MeOH is present or produced in the system without any substrate in the reactor. The time elapsed for emergence of DMMP into the IR gas cell was 40 minutes, equating to 20 µmol of DMMP flow.

A typical experiment was performed by pretreating the material samples by flowing N_2 through the bypass for a 30-minute period followed by switching to flow through the bubbler and collection of spectra every five minutes overnight, typically ~20 hours total collection. In other experiments when heating the sample was involved purge time was typically two hours plus 30-minutes for cooling; this is noted where necessary for clarity.

The concentration in the cell is not a true representation of the concentration coming from the microreactor due to the sizable change in volume between the cell and

the microreactor. In order to correct this Sheinker *et al*. used the differential equation

$$\frac{dC_{cell}}{dt} = \frac{f*C_{in}}{V} - \frac{f*C_{cell}}{V},$$ which can be rearranged and integrated to yield

$$C_{in} = \frac{C_{cell,t2} - C_{cell,t1}e^{-\frac{f}{V}(t_2-t_1)}}{1 - e^{-\frac{f}{V}(t_2-t_1)}},$$ where C_{in} is the concentration coming from the

microreactor, C_{cell} is the concentration in the IR gas cell, f is the flow rate in mL/min, V

is the volume in mL, t is elapsed time in minutes.[15] This same correction was used in the

work presented here.
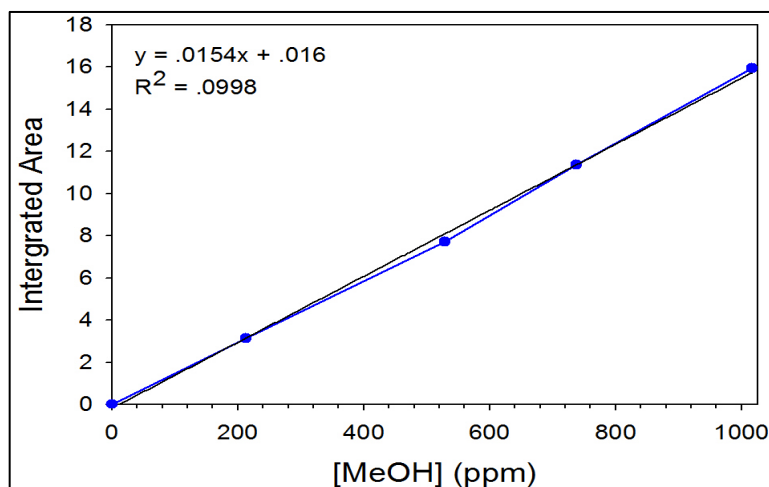
Figure 15. Microreactor methanol calibration curve.
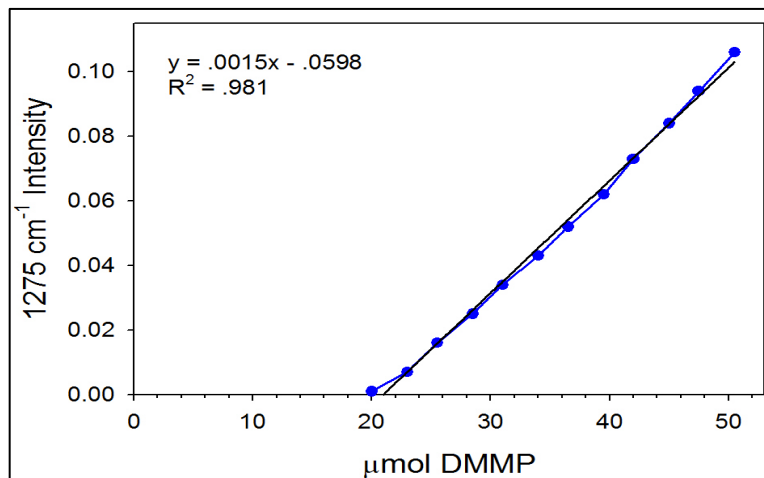
Figure 16. Microreactor DMMP breakthrough blank.

28

B. Material Characterization

  1. Thermogravimetric Analysis/Differential Scanning Calorimetry

Thermogravimetric analysis (TGA) and differential scanning calorimetry (DSC) are two techniques commonly used to describe energetics of a system. In the current work TGA/DSC collected using a Shimadzu TGA50/DSC60, and were used to characterize the desorption of water and decomposition of materials, including dehydrogenation and/or breakdown of the internal structure of the material, as a function of temperature.

Thermogravimetric analysis is a process that measures the change in mass of a sample versus the temperature or time. The sample is suspended on a small hanging balance inside of the instrument, on which an aluminum pan with the sample is placed, which monitors and records the mass of the sample as the programmed temperature ramp proceeds under a controlled environment, in all the cases used in this work pure N_2 atmosphere. From this one obtains a curve, which correlates weight loss or gain to specific temperature. Based on the starting mass and molecular mass of the components of the sample, it is possible for the user to ascribe what components of the material are being lost or gained at that specific temperature.

DSC is a technique that monitors the difference in heat flow of the sample versus that of an empty reference pan as a function of temperature. Instrument setup is two small pan holders inside of a calorimeter, one for a pan sealed with the sample inside, the other an empty sealed pan. Once the sample and reference are in place the calorimeter is closed and the temperature ramp is initiated. Since this technique is held at a constant pressure by a carrier gas, it is known that the heat flow is exactly equal to the change in enthalpy

29

as a function of temperature, $(dq/dt)_p = dH/dt$ where, in DSC $dH/dt = dH/dt$(sample) -

dH/dt(reference pan). The mathematics allow both positive and negative solutions

depending on which enthalpy change is greater, sample or reference. If the change in

enthalpy of the sample is greater than that of the reference the number will be positive

meaning an endothermic process (absorption of energy) has occurred, and *visa versa* for

an exothermic process (release of energy). The resulting dH/dt values are graphed as a

function of temperature and yield positive and negative peaks corresponding to the

aforementioned endothermic or exothermic processes.

2. X-ray Photoelectron Spectroscopy

   X-ray photoelectron spectroscopy was used to further characterize the materials.

XPS is a process, which under high vacuum, 10^{-8}-10^{-10} torr, a sample is bombarded with

low energy X-ray photons, produced from an aluminum anode hit with a beam of

electrons from an electron gun. The emitted photons are then passed through a

monochromator for the purpose of producing photons traveling at one specific

wavelength toward a sample, i.e. the energy of the photons are all the same. The energy

of the radiation passed through the monochromator is Al Ka x-rays, 1.486 eV = 8.34 Å.

When the photons contact the surface there is minimal penetration into the sample,

typically only a few nanometers, and this contact causes the photoelectric effect by which

core electrons are excited to exit the sample toward the detector by the photons. The X-

rays strike the entire sample, however, only a limited portion of the excited electrons are

analyzed due to a filter reducing the allowable electron ejection angle, which is the same

as the angle of the incident radiation relative to surface normal. The general equation of

the photoelectric effect is $\phi = hv - \frac{1}{2}m_e v$, where ϕ is the binding energy (work function

– minimum energy required to excite an electron), h is Planck's constant, v is the

frequency of the photon, m_e is the mass of an electron, and v is the velocity of the

electron ejected. Since the energy of the photon is a constant due to the monochromator,

the kinetic energy of the ejected electrons is measured using a electron energy analyzer,

thus, yielding the binding energy of that electron. Binding energies are individual and

characteristic of the specific electron orbitals of specific atom that the electron was

emitted, and thus, can be used as an identifying feature. XPS data was collected at

Georgia Institute of Technology using a Thermo K-alpha XPS using Al K-alpha source,

400 μm spot size, and 0.1 eV step size.

3. N_2 Sorption Isotherm

Nitrogen isotherm measurements were performed by Jacob Deneff, a graduate

student in the research group of Dr. Krista Walton at Georgia Institute of Technology,

using a Quadrasorb Evo produced by Quantachrome Instruments. Nitrogen sorption

isotherms can yield information about the material regarding surface area, pore size, and

pore distribution. The process is to first heat the material to 150 ^{o}C under vacuum

overnight, then cool the sample down to 77 K and incrementally dose N_2. After each dose

the material is allowed to reach equilibrium and the amount of adsorbed N_2 is

determined. This is continued until complete saturation of the material. The graph of each

of these points makes up the isotherm, and the characteristics of the graph give the

information regarding pore size and distribution. Surface area measurements are

calculated from a monolayer of adsorbed N_2, a subset of the entire isotherm information, as complete saturation of the material results multilayer adsorption of N_2.

4. X-ray Diffraction

Powder X-ray diffraction patterns were collected at Georgia Institute of Technology using a Panalytical XPert PRO Alpha-1 XRD equipped with Cu K-alpha source.

C. Materials

1. Zirconium Hydroxide

Type B zirconium hydroxide, $Zr(OH)_4$ was received from Edgewood Chemical and Biological Center. The material was ground in a mortar and pestle and passed through a 125 μm sieve and stored in a sealed glass vial. Zirconium hydroxide nanopowder ($Zr(OH)_4$ 99.9 %, 40 nm, Amorphous) was purchased from US Research Nanomaterials, Inc. Both materials were stored in sealed glass vials.

2. Metal-Organic Frameworks

The Craig Hill group, primarily Wei-Wei Gou, at Emory University using the standard methods discussed in the background section, synthesized the MOFs, UiO-66, UiO-66-NH2, and UiO-67. Samples were ground in mortar and pestle and passed through 125 μm sieve and stored in sealed glass vials kept in the dark.

3. Reaction Analytes and Standards

Dimethyl methylphosphonate (DMMP), 99 %, purchased from Alfa Aesar, was distilled and placed into sealed containers. DMMP was tested using a Shimadzu GCMS-QP2010 PLUS for impurities before experiments to confirm purity. Dimethyl hydrogen phosphite, 99 %, was purchased from Sigma Aldrich. Methanol 99.999 % was purchased from Fisher Scientific. MeOH calibration mixture 0.104 % in N_2 was purchased from Praxair.

D. Synthesis

1. Nano zirconium hydroxide

The following procedurewas used to synthesize nano-particulate $Zr(OH)_4$ was performed. Approximately 200 mg of $Zr(OH)_4$ as received was placed into a 20 mL glass vial that had been triply rinsed with 18.3MΩ nano-pure water. Nano-pure was then added to give a final concentration of 10 mg/mL and was then shaken, and sealed with electrical tape. The sealed vial was then placed into an ultrasonic bath at room temperature for 6 hours with repeated shaking every 30 minutes to disrupt any settlement to the bottom of the vial. Once sonication was complete the solution was allowed to stand for 10 minutes before decanting into a centrifugation tube. The solution was then centrifuged at ~260 xG for five minutes followed by decanting the supernatant into another tube and repeated two more times. The solution was then decanted into a new triply rinsed glass vial. Any of the material to be studied was placed into an oven preheated to 60 ^{o}C in an evaporation dish covered by a watch glass and left overnight. The resulting material was scraped from the sides and bottom of the evaporating dish and placed into a glass vial.

CHAPTER III. ZIRCONIUM HYDROXIDE RESULTS

A. Material Characterization

 1. Differential Scanning Calorimetry

      Figure 17 shows the DSC thermogram of the zirconium hydroxide sample. The

curve shows 4 distinct peaks, one endothermic and the other three exothermic. The

endothermic peak is seen first corresponding to the loss of physiosorbed H_2O from the

$Zr(OH)_4$. The peak's maximum is at 60 ^oC and extends from the start of the heating to

over 100 ^oC, This first peak maximum was quite a bit lower than 88 ^oC reported by

Stefanic et al.[60] The three exothermic peaks are due to calcination of the material through

different phases, listed Table 2. The overall calcination seems to follow a mechanism put

forth by Sato et al.[61] $Zr(OH)_4 \rightarrow$ Amorphous $ZrO_2 \rightarrow$ Metastable Tetragonal $ZrO_2 \rightarrow$

Monoclinic ZrO_2. The first peak centered at 60 ^oC is due to physiosorbed H_2O as stated

before, with the shoulder indicating the shift to amorphous ZrO_2 by the removal of

chemisorbed H_2O species. The peaks at 370 and 439 ^oC indicate the next two changes

respectively. The last peak is proposed to be the direct conversion of Amorphous $ZrO_2 \rightarrow$ Monoclinic ZrO_2, an additional pathway described by Sato in the same study, believed

to be seen due to change of the material due solely to grinding the sample.[61,62]

Table 2. Results from DSC $Zr(OH)_4$ thermogram.   *Also observed by Stephanic et al.[60]

Transition Type	Range (^oC)	Maximum (^oC)	Enthalpy (kJ/mol)
Endothermic	30-100	60	34.99
Exothermic	330-380	367	-4.36
Exothermic*	425-475	448	-9.20
Exothermic	480-580	526	-48.04
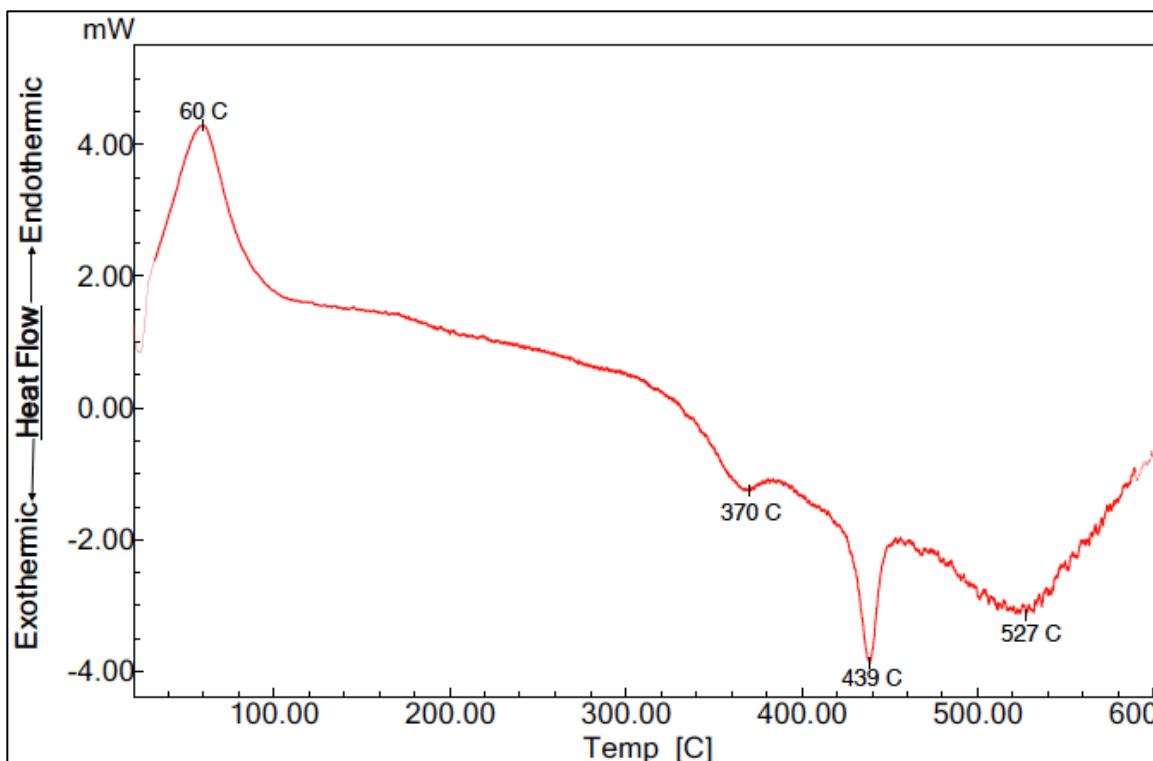
Figure 17. DSC thermogram of Zr(OH)₄.

2. Thermogravimetric Analysis

Though zirconium hydroxide materials vastly differ in pore volume and surface area, due to different synthesis conditions, the TGA curve is consistent. This holds true in the current work as well, Figure 18. There is an initial loss of weakly bound H_2O starting at just above room temperature continuing to 70 ^{o}C at which point another curve starts corresponding to the condensation of neighboring OH groups, and persists throughout the duration of the experiment. It should be noted that typically this TGA analysis of Zr(OH)₄ is continued up to 900 ^{o}C at which point complete calcination of the material is seen, however, that range far exceeds the scope of this study.[26] The curve is very similar to those previously sited, with total loss percentage ~28 % at 600 ^{o}C which is in good agreement with the 30-35 % reported experimentally and theoretically for the fully calcined material.[28,63]
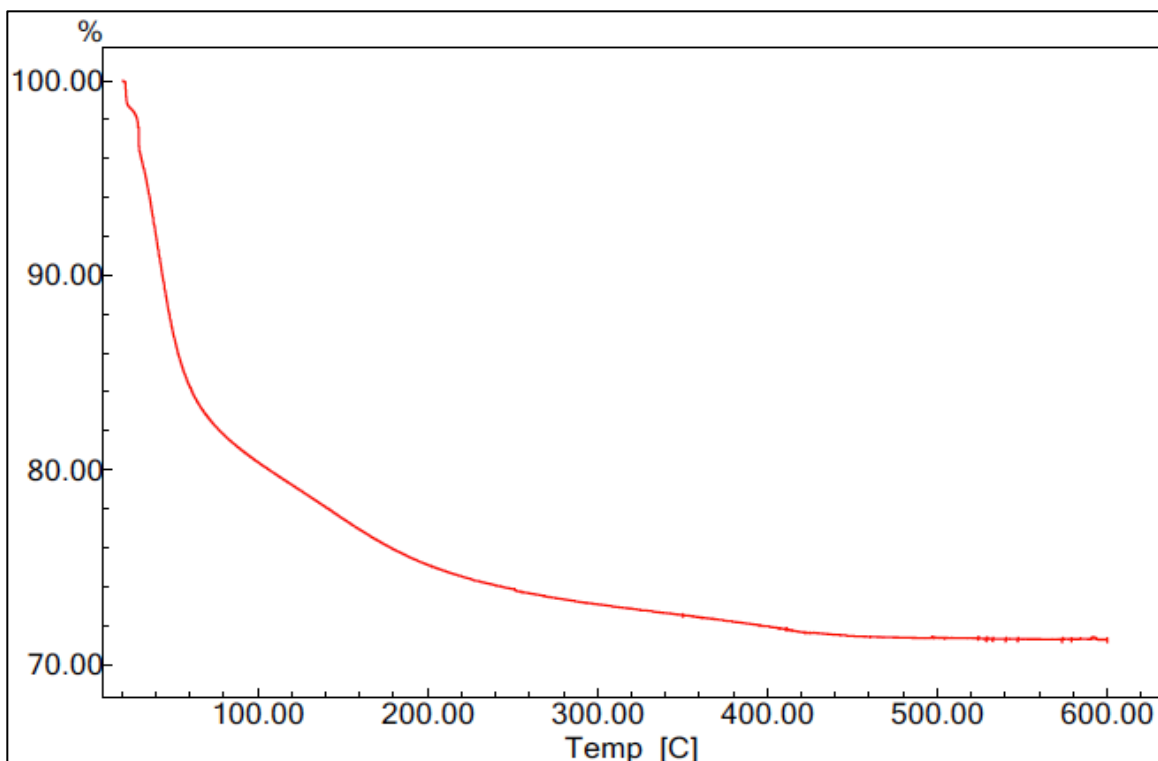
Figure 18. TGA curve of Zr(OH)₄.

3. N$_2$ Sorption Isotherms

      The Zr(OH)$_4$ material was analyzed prior to and after exposure to DMMP for

BET surface area and pore volume. The results showed that the BET surface area of the

native material was 462 m^2/g, much lower than the 530 m^2/g reported by Bandosz *et al.*[26]

Following exposure to DMMP the material was again analyzed showing an expected

significant decrease in surface area to 273 m^2/g from surface binding of the DMMP or its

reaction products. The isotherms for before and after, Figure 19, both exhibited type IV

curves containing a small hysteresis loop indicating some mesoporosity, 2-50 nm, present

in the sample, thus, subject to capillary condensation.[64-66] The total pore volume was

reduced ~30 % after exposure to DMMP. As evidence to the strength of the binding of

reacted DMMP to the Zr(OH)$_4$, it is useful to understand that in preparation for the N$_2$

36

isotherm measurements the material were heated to 150 $^{\circ}$C and held under ultrahigh

vacuum overnight.
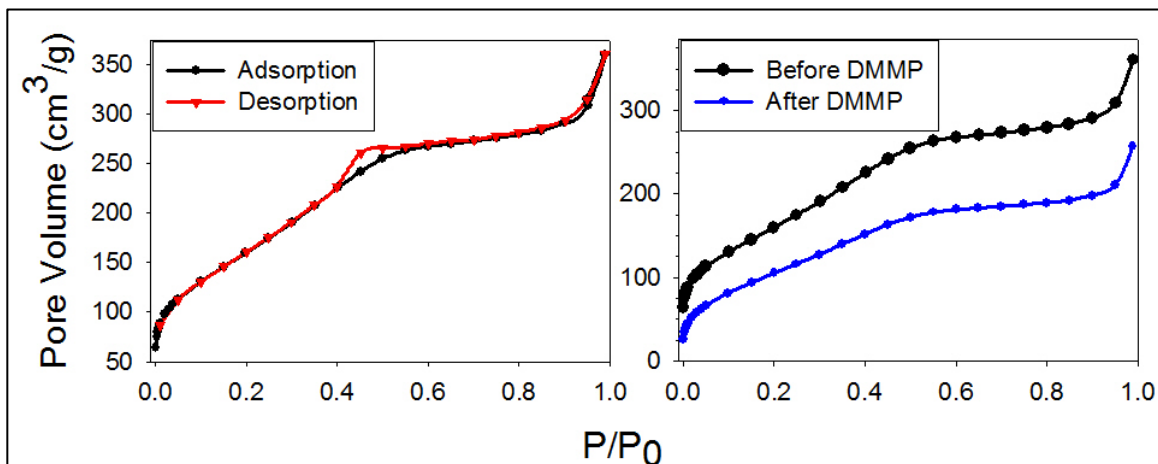
Figure 19. N$_2$ isotherms of Zr(OH)$_4$.

4. XRD and XPS

X-Ray diffraction characterization of the material was conducted to gain insight

into the material prior to conducting reactions with DMMP. PXRD diffraction pattern

was obtained to confirm the expected physical state of the Zr(OH)$_4$. Figure 20 shows that

the Zr(OH)$_4$ was absent of any significant crystallinity, which would be indicated by

well-defined sharp peaks in the diffraction pattern. XPS data confirmed the material was

composed of only zirconium, 31.31 % and oxygen, 68.69 %. The deconvoluted Zr3d

peaks, Figure 21, best fits 3 peaks at 182.4, 184.8, and 186.9 eV, assigned the large

characteristic peaks to Zr^{4+}, Zr-O sites, and the smaller peak to is likely due to charging

of the sample.[67-70]
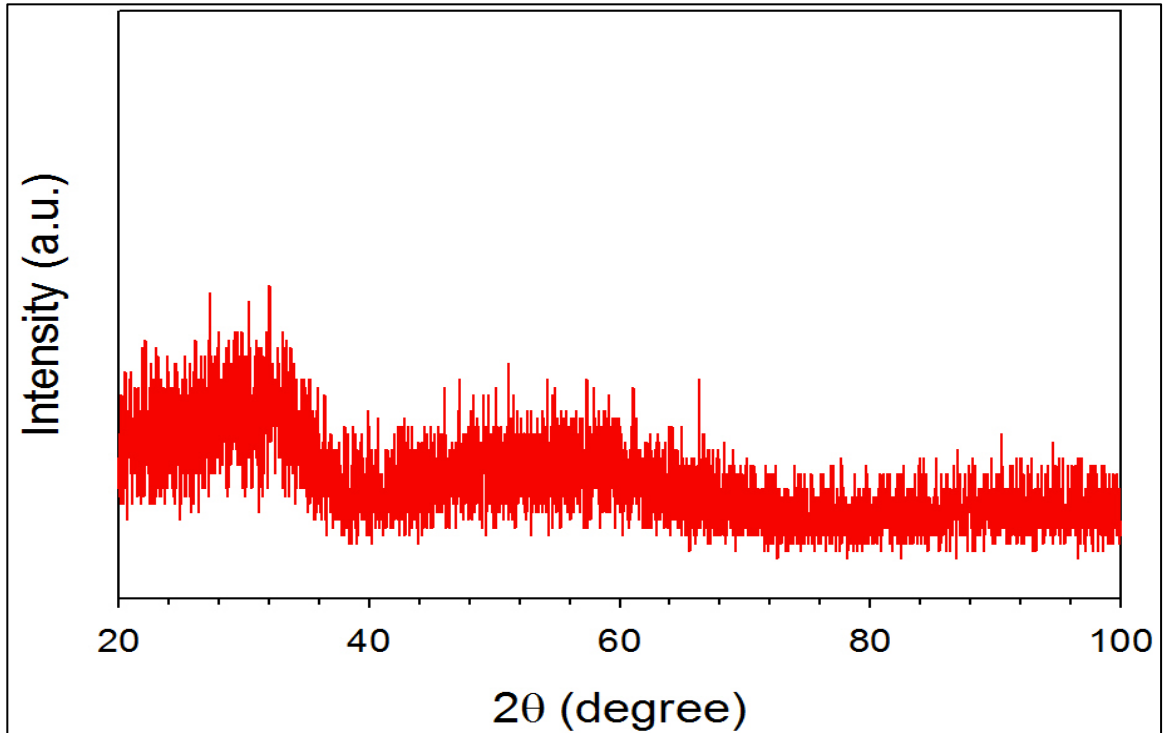
Figure 20. Zr(OH)₄ XRD diffraction pattern.
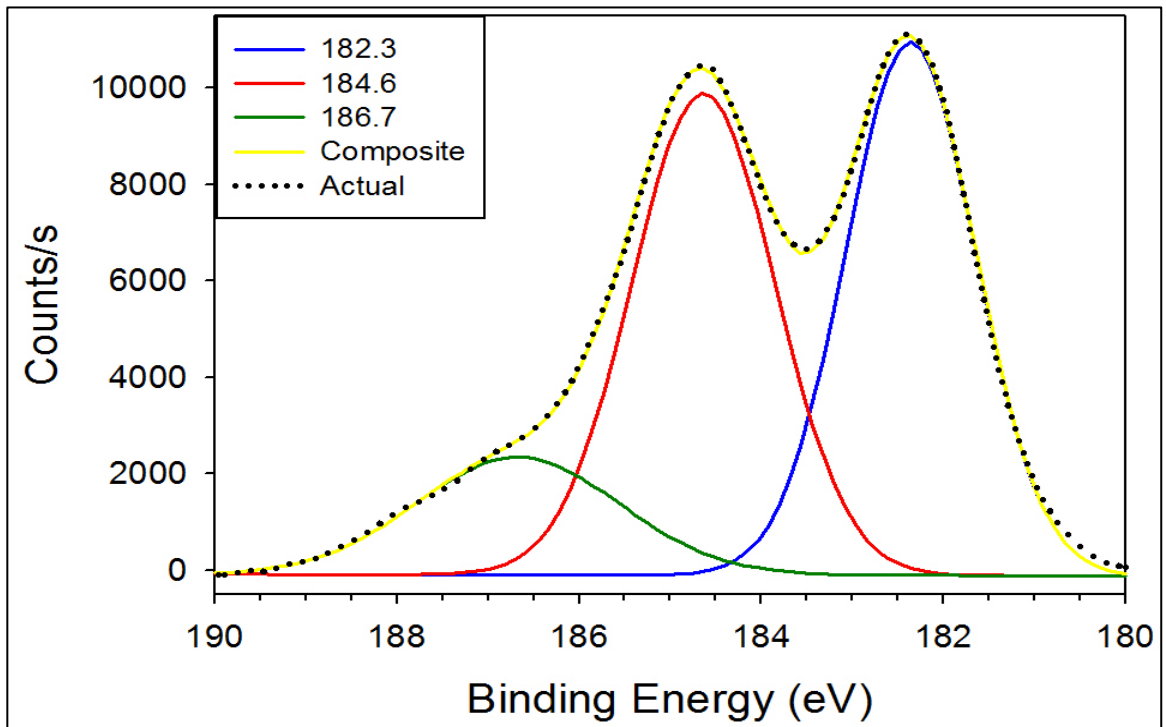
Figure 21. Deconvoluted Zr(OH)₄ Zr3d spectrum.

B. Room Temperature Reaction

  1. DRIFTS Results

    a. DMMP on a Reactive vs. Non-Reactive Material

        When DMMP adsorbs molecularly on solid surfaces, often via hydrogen-bond

formation between the phosphoryl oxygen and a surface hydroxyl, the adsorbed species

gives rise to a set of well-defined bands that are relatively easy to assign based on their

similarity to bands assigned in previous examinations of the vibrational modes of

molecular DMMP.[14, 71-75] This initial interaction of the phosphoryl oxygen and the

surface hydroxyl on Zr(OH)$_4$ was predicted using computational molecular dynamics by

Ivan Iordanov, shown Figure 22.[76] This initial interaction via the phosphoryl oxygen has

been seen many times previously in the interaction of DMMP with other metal

oxides.[14,17-18,20-21,75]
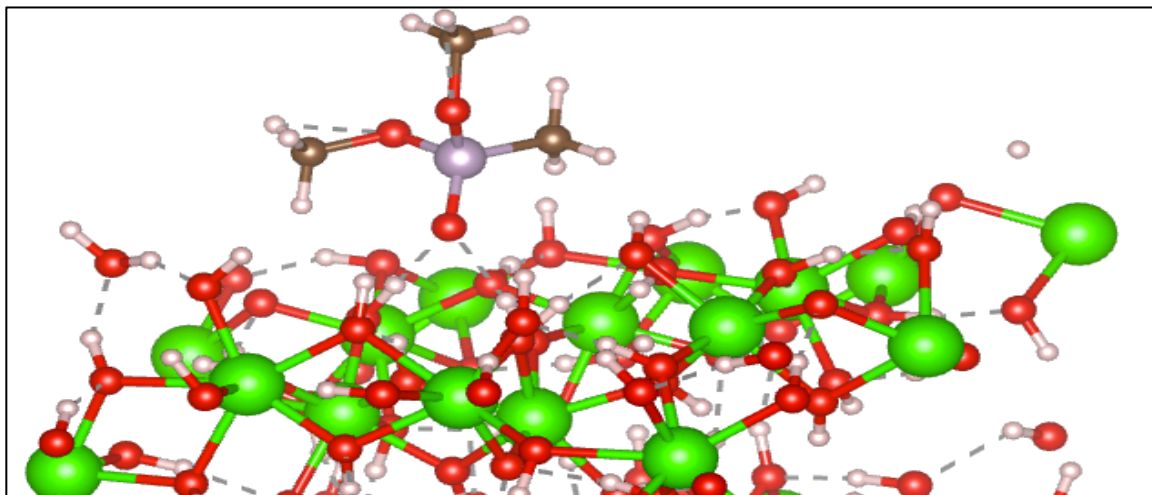
Figure 22. Molecular dynamics simulation of the initial interaction of DMMP with Zr(OH)$_4$.

        The four gas-phase DMMP C-H stretching bands that correspond to the two P-

OCH$_3$ groups at 2962 and 2858 cm^{-1} [v_a(P-OCH$_3$) and v_s(P-OCH$_3$)] and the P-CH$_3$ group

at 3007 and 2924 cm^{-1} [v_a(P-CH$_3$) and v_s(P-CH$_3$)] are not particularly susceptible to shifts

in frequency as the bonding environment of the phosphorous atom changes. Figure 23

demonstrates the frequency alignment of the C-H stretching bands for DMMP adsorbed on silica and on Zr(OH)$_4$. The bands of DMMP adsorbed on silica are due to molecularly adsorbed DMMP, while the DMMP adsorbed on Zr(OH)$_4$ has reacted to form a methyl methylphosphonate (MMP) species, with one methoxy group and one methyl group. This is apparent due to the relative intensity difference of the C-H stretching bands [P-O-CH$_3$]:[P-CH$_3$] being 2:1 and 1:1 for silica and Zr(OH)$_4$, respectively. Nonetheless, the frequencies of the C-H stretching vibrations of the DMMP adsorbed on the 2 different materials agree within 9 cm^{-1}, Zr(OH)$_4$→Silica exhibits a shift of 2852→2858; 2927→2931; 2954→2962; 2997→3006.
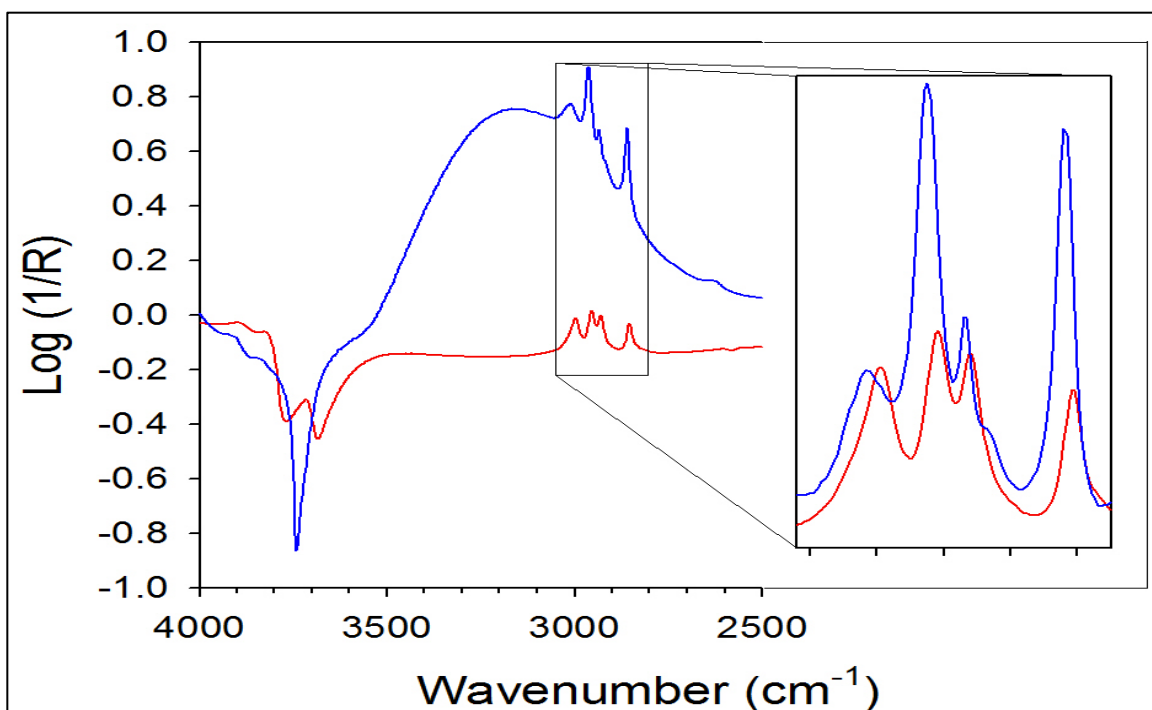
Figure 23. DRIFT spectra of silica (blue) and Zr(OH)$_4$ (red) exposed to 70 μmoles of DMMP, with the excerpt showing the comparison after baseline correcting.

As can be seen in the spectra displayed in Figure 23, there is a loss of O-H intensity as DMMP adsorbs on silica at 3750 cm^{-1}, which is replaced by a very broad O-H absorption that bands near 3100 cm^{-1}. This can be explained by hydrogen-bond formation between the P=O group of DMMP and surface OH groups, causing a

weakening of the O-H bond, leading to a red-shift and increased intensity for the hydrogen-bonded vibrational mode, as well as broadening of the O-H stretch absorption due to the number of different bonding environments. On the $Zr(OH)_4$ surface, the loss of O-H intensity is similarly observed, but far less corresponding hydrogen-bonded O-H vibration is observed. This is consistent with reaction of the adsorbed DMMP with the surface O-H groups to form methanol, which evolves from the surface, removing the O-H group instead of forming a hydrogen-bonded O-H species.
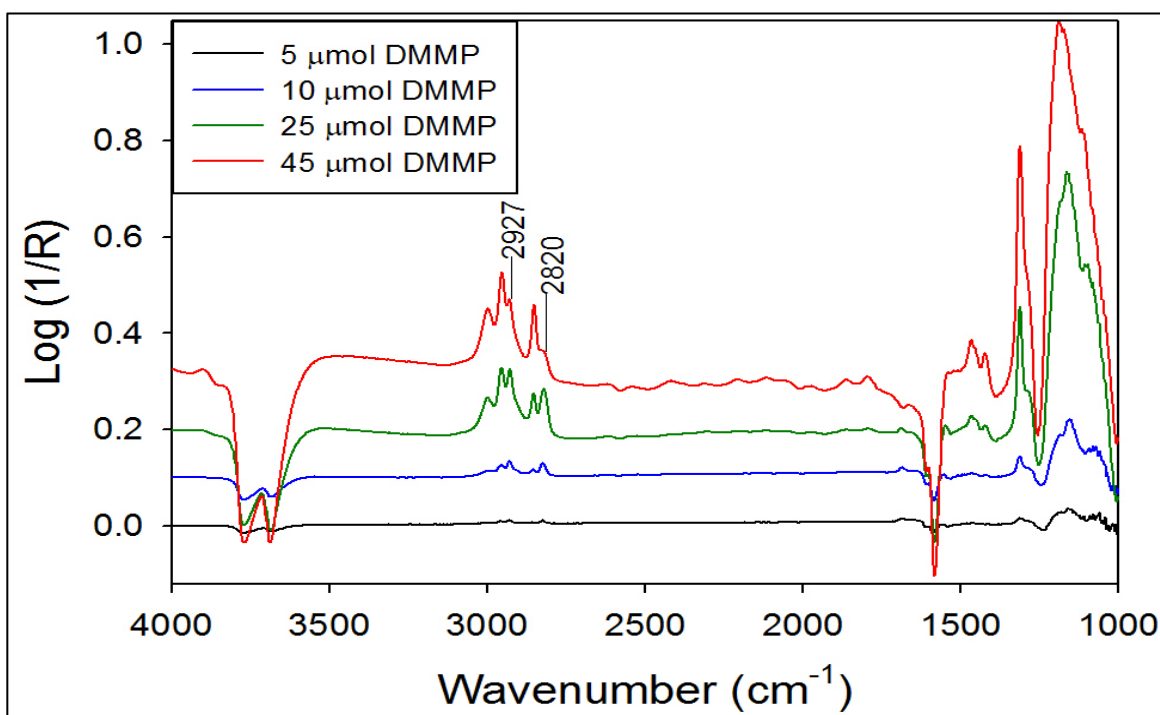
Figure 24. Evolution spectra of introducing DMMP to Zr(OH)$_4$ up to 45 μmol.

b. Zr(OH)$_4$ Exposed to 45 μmol DMMP

Figure 24 shows the evolution of the DRIFT spectrum of DMMP as it adsorbs and reacts with $Zr(OH)_4$. While the spectrum of DMMP on $Zr(OH)_4$ shown in Figure 23 was obtained after exposure of the solid to 70 μmoles of DMMP and then evacuating the cell to remove physisorbed and weakly chemisorbed species, the sequence of spectra shown

in Figure 24 was measured with a background pressure of approximately 3 torr of the

flowing DMMP/N$_2$ mixture in the cell. Table 3 shows the assignments of the absorptions

in Figure 24 to the various vibrational modes of DMMP, and were made by comparison

with detailed studies of DMMP and isotopically-labelled DMMP, and with results from

other studies of adsorbed DMMP.[71,72] Figure 24 provides additional evidence for the

interpretation of DMMP reaction on Zr(OH)$_4$ discussed earlier. Spectra corresponding to

the initial contact of the solid with DMMP clearly show a band at 2820 cm^{-1}, which does

not correspond to any C-H absorption of DMMP, and relative intensities that are not

expected for DMMP.

Table 3. Vibrational modes and wavenumbers of DMMP, absorbed and gas phase. ν: bond stretch δ: deformation

Vibrational Mode	Current work (cm^{-1})	Previous work[72] (cm^{-1})	Gas Phase DMMP[72] (cm^{-1})
ν_a (CH$_3$-P)	2997	3001	3014
ν_a (CH$_3$-O-P)	2954	2955	2962
ν_s (CH$_3$-P)	2929	2932	2924
ν_a (surface-OMe)	2929	-	-
ν_s (CH$_3$-O-P)	2853	2855	2860
ν_s (surface-OMe)	2820	2827	-
ν (P-H)	2425	-	-
δ_a (O-CH$_3$)	1466	1464	1467
δ_a (P-CH$_3$)	1423	1420	1423
δ_s (P-CH$_3$)	1313	1313	1315
ν (P=O)	1194	-	1276

Figure 25A shows the DRIFT spectra of DMMP on silica and Zr(OH)$_4$ after

exposure of the solid to 20 μmoles of DMMP, compared to the DRIFT spectrum of

Zr(OH)$_4$ after exposure to 10 μmoles of methanol. Comparison of the C-H stretching

regions of these three spectra provides a clear basis for assignment of the features

observed and their origin. The 2820 cm^{-1} band is assigned to the C-H symmetric stretch

of a surface bound methoxy. What the collected spectra indicate is that as DMMP comes

into contact with the Zr(OH)$_4$ it is decomposed into a methyl methylphosphonate and a

surface bound methoxy (surface-OMe), evidenced by the 5 strong well defined bands in

the C-H stretching region at 2997, 2954, 2929, 2853, and 2820 cm^{-1}. What can further be

noted from Figure 24, is that as the experiment proceeds there comes a change in the

spectra ~25 μmol of DMMP where the intensity of the v_s (surface-OMe) band, reaches a

maximum. The subsequent decrease of the v_s (surface-OMe) band continues until it

nearly disappears after the flow of DMMP is stopped and cell is evacuated. There are two

proposals as to what occured: 1) The surface bound methoxy group is initially formed

from the decomposition of DMMP (DMMP → surface-MMP + surface-OMe), occurring

only at specific reactive sites on the surface, likely the higher wavenumber terminal OH

site at 3771 cm^{-1} as noted by Bandosz et al.[26] Once these sites are exhausted it causes the

decomposition to slow/cease and subsequent DMMP adsorption displaces the surface-

OMe as gas phase MeOH. 2) DMMP decomposition occurs at a steady rate throughout

exposure at both active OH sites, 3771 and 3686 cm^{-1}, of which the DMMP has no

proclivity for which site physisorption or chemisorption can occur. MeOH however,

shows proclivity toward the higher wavenumber OH site at 3771 cm^{-1}, which can be seen

in Figure 25A where the 3771 cm^{-1} shows significantly more loss than the band at 3686

cm^{-1}, Ouyang et al. has also shown this preference.[77] In addition Ouyang showed that any

MeOH that did adsorb onto the lower wavenumber site, can migrate to the higher

wavenumber site.[77] Thus, when DMMP decomposes at the lower wavenumber OH site at

3686 cm^{-1}, the surface bound product either migrates to the higher wavenumber OH site,

or rather than forming a surface-OMe, the decomposition directly yields gas phase

MeOH, which is pulled through the sample via the vacuum pump. This direct conversion

to gas phase MeOH has been previously noted, first by Templeton et al.[12,13] Again in this

proposal it is suggested that surface-OMe that is formed is subsequently displaced by additional DMMP adsorption, and in support of both proposals, Ouyang *et al.* showed that the surface-OMe can be displaced by other organic species.[77]
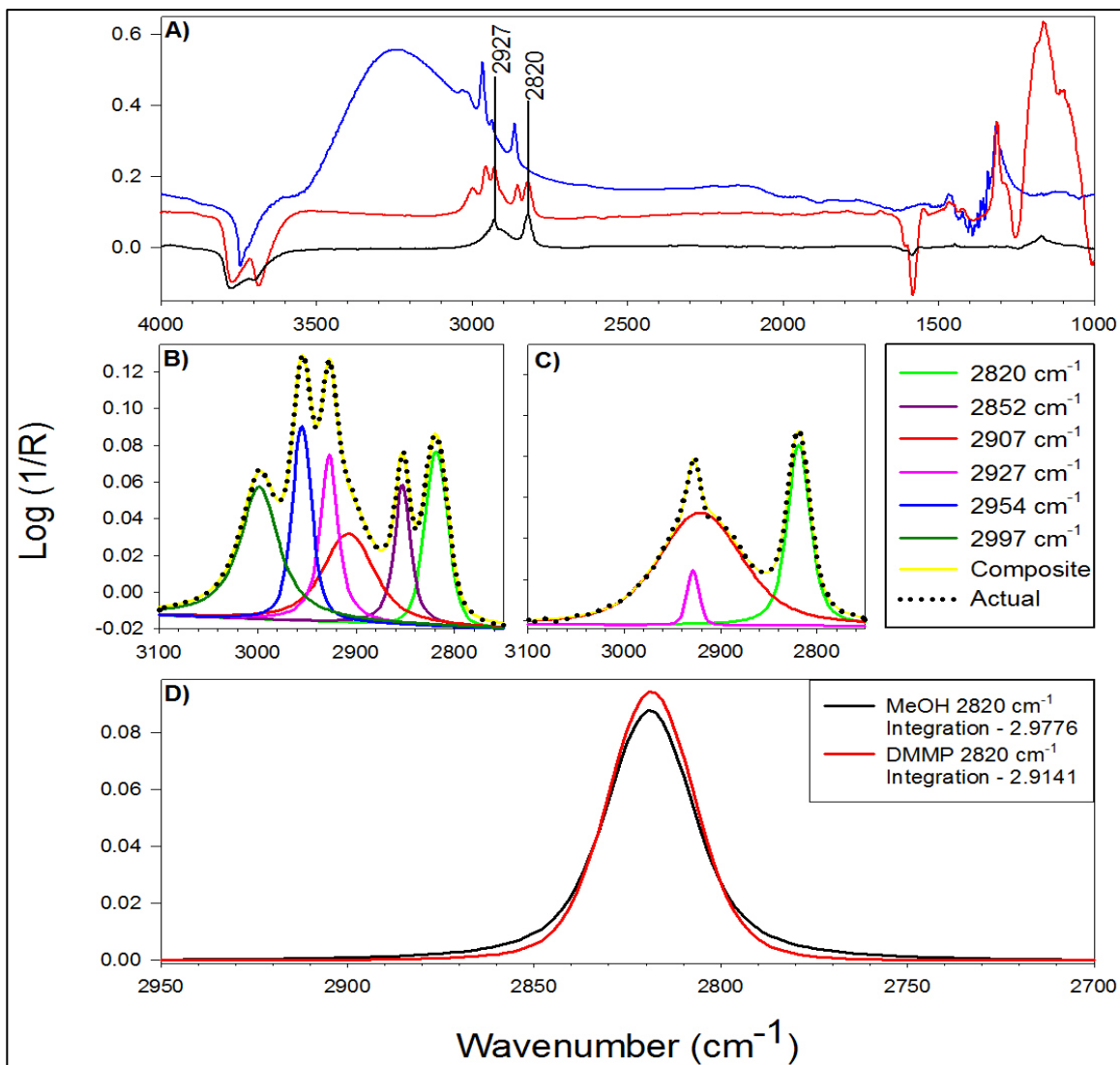
Figure 25. (A) Spectral comparison of Silica exposed to DMMP (blue), Zr(OH)$_4$ exposed to DMMP (red), and Zr(OH)$_4$ exposed to MeOH (black). (B) Deconvolution of 20 μmol of DMMP on Zr(OH)$_4$. (C) Deconvolution of 10 μmol MeOH on Zr(OH)$_4$. (D) Overlay of deconvoluted 2820 cm^{-1} bands from B and C.

The relative intensity of the 4 C-H stretching bands of DMMP are not in the 2:1 relative intensities of [P-O-CH$_3$]:[P-CH$_3$] expected for molecular DMMP, as with the silica, nor are they 1:1 as shown by the evacuated reacted 70 μmol DMMP on Zr(OH)$_4$ (surface-MMP), Figure 24. Understanding that after evacuation overnight the spectrum

44

reveals this 1:1 behavior is in support of the second proposal, where the DMMP is available to continually react producing both gas phase and surface-OMe, which is eventually displaced as gas phase MeOH.

Figure 25B and C show the deconvolution of the C-H stretching region, set to the same vertical and horizontal scale, of 20 μmol of DMMP and 10 μmol of MeOH on $Zr(OH)_4$, respectively. Figure 25 A, B, and C all confirm the assignment of the 2820 cm^{-1} band but also accounts to an extent for an discrepancy of the relative intensities of the DMMP bands observed, discussed above regarding that they are neither conclusive of MMP or DMMP adsorption. Namely, the relative intensity difference caused by the surface-OMe is due to the broad band at 2907 cm^{-1} and the sharp band aligning with the DMMP band, v_s (CH$_3$-P), at 2927 cm^{-1}, adding intensity spanning all 4 characteristic DMMP bands to varying degrees. An overlay of the deconvoluted 2820 cm^{-1} bands of DMMP on $Zr(OH)_4$ and MeOH on $Zr(OH)_4$, is shown Figure 25D. The integration of the v_s (surface-OMe) bands shows that 20 μmol of DMMP on the $Zr(OH)_4$ surface produces ~98 % of what is observed for 10 μmol of MeOH on the $Zr(OH)_4$ surface, indicating that either each DMMP is not decomposing, which could not lead to the end result of MMP after evacuation, or that the above proposal is correct in that gas phase MeOH is also able to be produced. Considering the hydroxyl group behavior when DMMP reacts with $Zr(OH)_4$, discussed in in more detail in the following section, which shows equivalent loss amounts of both OH bands, it is not unreasonable to consider that the DMMP is reacting at both OH sites, one yielding surface-OMe the other yeilding a mixture of gas phase MeOH and surface-OMe, which at both sites all surface-OMe is eventually displaced as gas-phase MeOH.
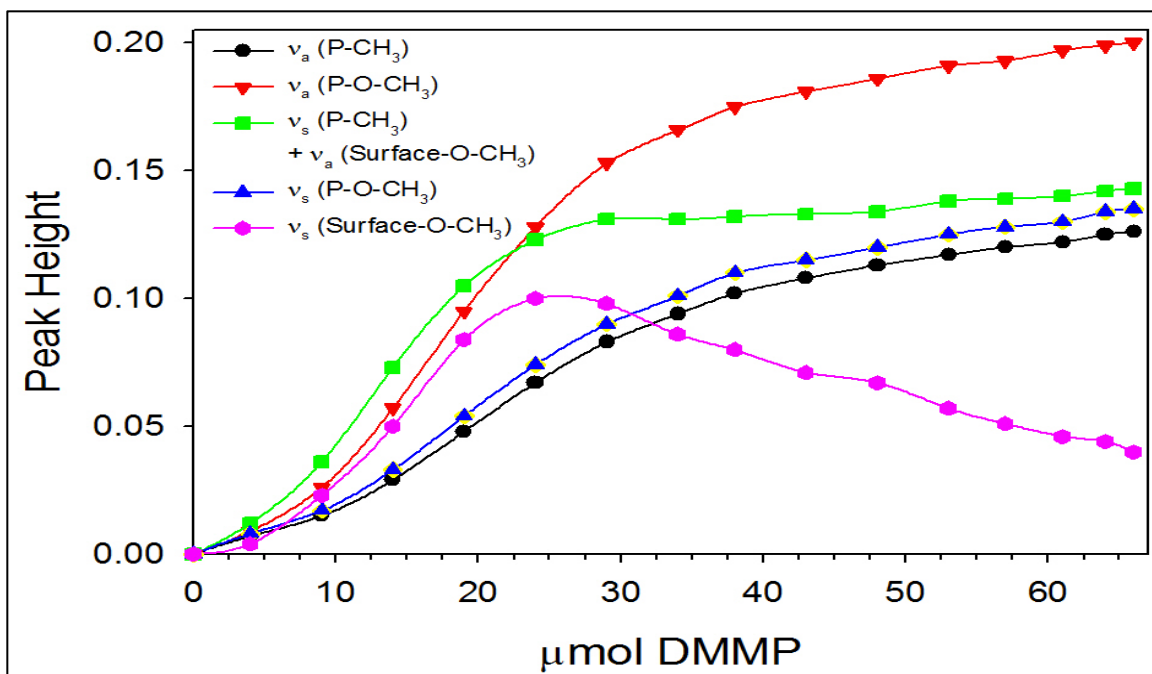
Figure 26. Evolution of C-H stretches in spectra of Zr(OH)₄ during DMMP exposure.

The graph of the peak heights of the CH stretching region are shown Figure 26. The v_s (surface-OMe) band increases until reaching a maximum ~25 μmol before decreasing back towards baseline. The v_s (CH$_3$-P) band appears to grow in and reach a semi-plateau more rapidly than the other bands corresponding to DMMP features. This is due to the combination of the DMMP feature and surface-OMe feature. The semi-plateau is seen to occur at the same time as the decrease in the v_s (surface-OMe) band is seen. The surface-OMe is being displaced by a DMMP molecule yielding ~1:1, [surface-OMe]:[CH$_3$-P], exchange causing this apparent plateau in the v_s (CH$_3$-P) band. There is some rise in the v_s (CH$_3$-P) due to DMMP adsorption in locations other than the ones where the surface-OMe is being displaced and once most of the surface-OMe has been removed the v_s (CH$_3$-P) returns to a similar increase rate as to what is seen from the other DMMP C-H bands. The other three features from DMMP show rapid initial uptake until

~30 μmol followed by slower uptake, simply due to lower number of available sites for the DMMP to adsorb as the surface is saturated.

c. Hydroxyl Group Behavior During Exposure

In coordination with the increase in intensity of DMMP bands are the expected losses of OH stretches. The two prominent negative-going bands at 3771 cm^{-1} and 3686 cm^{-1} are due to the loss of surface-bound OH groups with the corresponding bending mode losses at 1605 cm^{-1} and 1586 cm^{-1}. The bands at 3771 cm^{-1} and 3686 cm^{-1} to terminal (*t*-OH), and bridging (*b*-OH) OH sites respectively.[78,79] The OH stretching bands do not differ much in intensity at any given time, showing loss at almost identical rates Figure 27. There is no definitive evidence that either is solely responsible for the decomposition into methanol and MMP. Rather the evidence is support of the contrary that both sites are active in both adsorption and decomposition of DMMP.
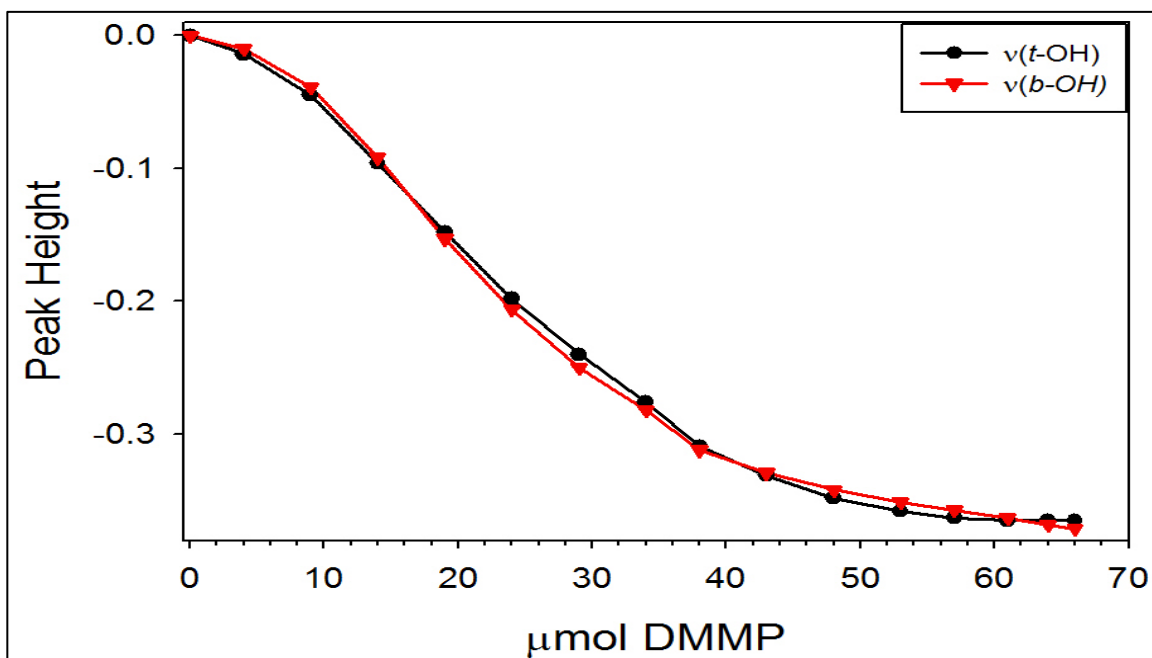
Figure 27. Loss of OH species on Zr(OH)₄ during exposure to DMMP.

d. Zr(OH)$_4$ Exposed to 70 μmol DMMP and Post-Exposure Evacuation

At higher exposures of DMMP to the solid, at ~40 μmol, a band emerges at 2425 cm^{-1} and continues to grow in intensity throughout the duration of exposure, shown Figure 28. This band continues to increase in intensity throughout the dosing and continues if the sample is evacuated with no additional DMMP introduced. A plot of peak height of the 2425 cm^{-1} band in comparison to the v_s (CH$_3$-O-surface), δ_a (P-O-CH$_3$), and δ_a (P-CH$_3$) bands is shown Figure 29. The 2425 cm^{-1} band is not seen in the MeOH experiment, previously discussed, even after being left for two days under vacuum. There are no combination or overtone bands that might give rise to this absorption so it was investigated as a characteristic vibrational mode. The only functional groups that have an absorption in this region of the spectrum, and could be constituted from the species in the sample, are a P-H or P-O-H bond.[80-83]
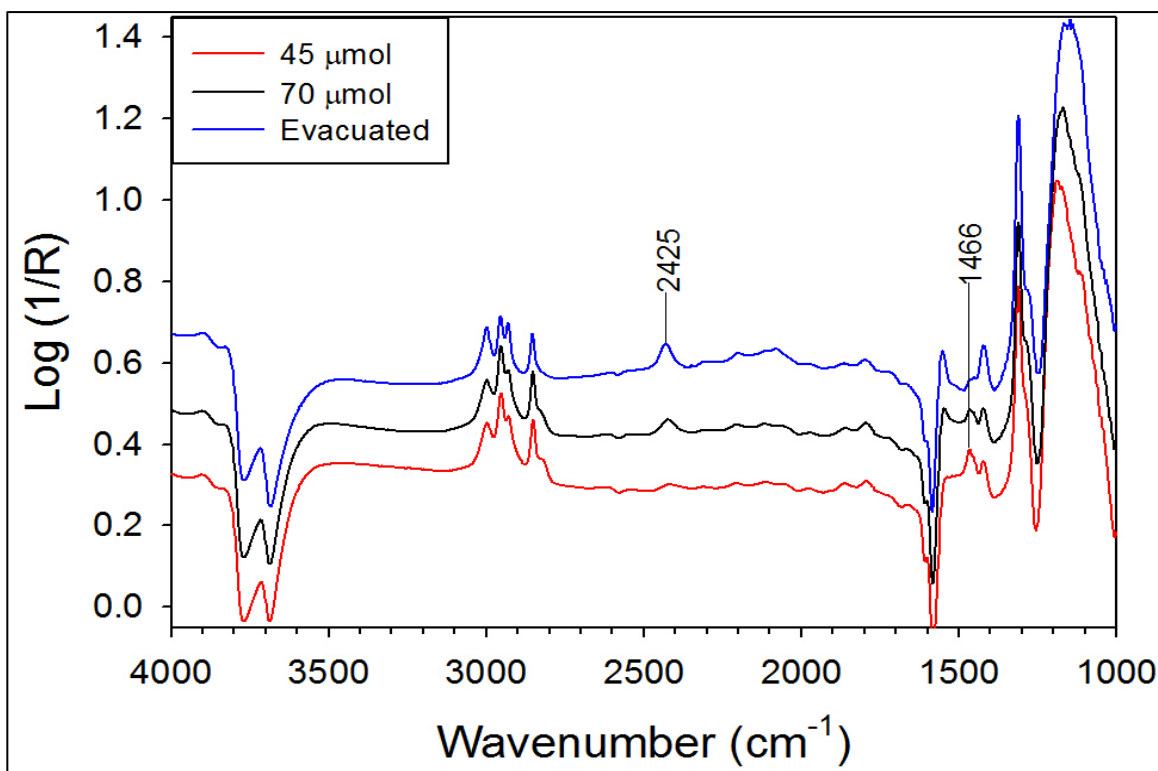
Figure 28. Evolution spectra of introducing DMMP to Zr(OH)$_4$ from 45 to 70 μmol and after evacuation of the sample.
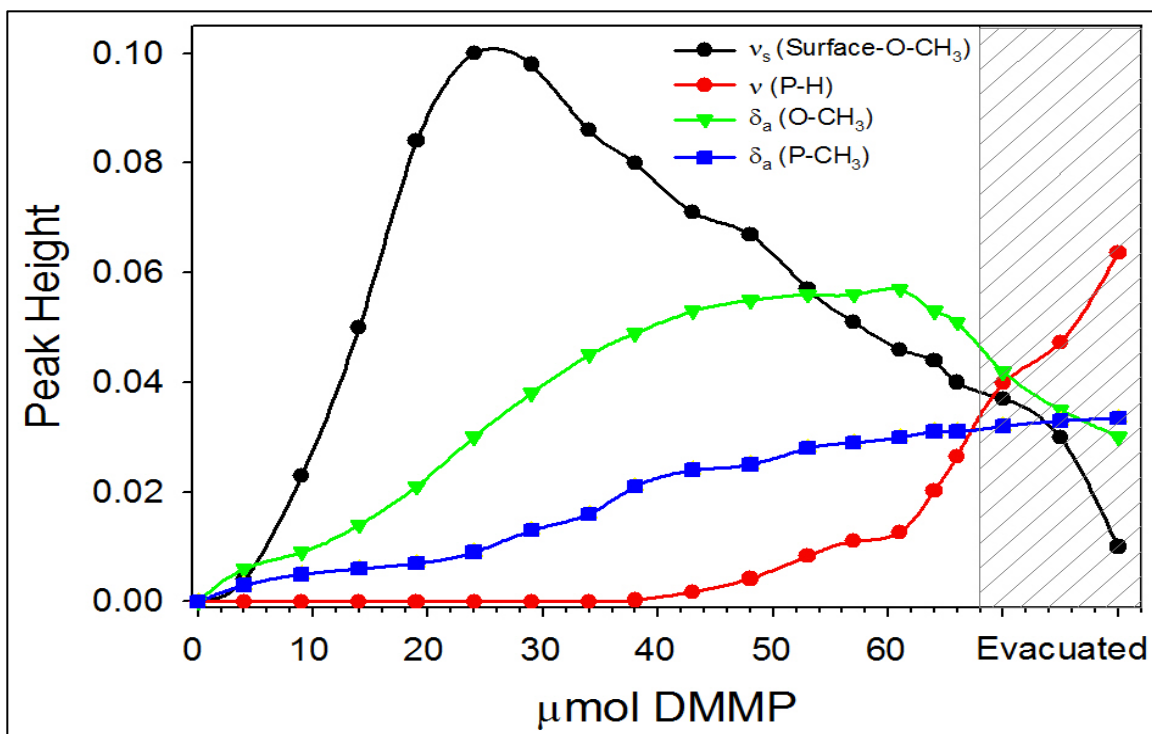
Figure 29. DRIFTS reaction analysis comparing profiles of δ_a (O-CH$_3$), δ_a (P-CH$_3$), v (P-H), and v_s (CH$_3$-O-surface).

i. Deuterated Zr(OH)$_4$

To confirm the proposed feature indeed was a P-H stretch, a deuterated sample of

Zr(OH)$_4$ was prepared, using the method inspired by Yamaguchi *et al.*[79] Rather than

simply introducing the evacuated sample to an static environment of D$_2$O at room

temperature, the sample here was heated to 80 ^{o}C with a flow of UHP N$_2$ assisted with a

vacuum pulling the N$_2$ through, and once the Zr(OH)$_4$ reached 80 ^{o}C the flow was

switched to pure D$_2$O vapor which was intermittently stopped allowing the cell to

evacuate before resuming flow of D$_2$O vapor. This was repeated until OH stretches

appeared to be absent from the single beam spectra and the sample was allowed to cool to

room temperature under flow of N$_2$ followed by evacuation overnight. Alternative less

effective methods of deuteration included: stirring in D$_2$O followed by boiling off,

refluxing in D$_2$O for multiple days followed by boiling off, and leaving Zr(OH)$_4$ in

DRIFTS cell at room temperature in atmosphere of pure D_2O three times for five minutes (50 % deuteration).

Figure 30 shows a comparison of the DRIFT spectrum obtained when the $Zr(OD)_4$ solid was exposed to 70 μmoles of DMMP and then evacuated overnight to that of $Zr(OH)_4$. The shift in the O-H loss features upon deuteration can easily be seen, The O-H loss features at 3768 cm^{-1} and 3689 cm^{-1} shift to 2780 cm^{-1} and 2727 cm^{-1}, respectively, for the deuterated species, which are similar to the values observed by Yamaguchi et al.[79] A comparison of the intensities of these features suggests that approximately 80 % of the O-H species are deuterated and that the deuteration process was non-discriminative between t-OH and b-O sites. The factor of 0.728 (1/1.374) shift is exactly what one would expect for replacing an O-H oscillator with an O-D oscillator, shifting 3768→2771 and 3689→2717 cm^{-1}. The same logic applied to the 2425 cm^{-1} band, assuming it is a harmonic P-H oscillator, would predict a shift of 0.718 (1/1.393), to 1750 cm^{-1}, upon replacement with a harmonic P-D oscillator. In confirmation of the predicted value a band begins to grow in at 1755 cm^{-1} after dosing with 45 μmol of DMMP, and continues to grow in through the remainder of the dosing and beyond, exactly as was seen for the 2425 cm^{-1} band of the non-deuterated $Zr(OH)_4$ sample. Since the $Zr(OH)_4$ was unable to be fully deuterated there is a slight band seen at 2425 cm^{-1} from the P-H stretch. The other features due to the DMMP adsorption and reaction are remarkably similar between the two solids. These results not only verify the nature of the band at 2425 cm^{-1} as being due to a P-H bond, but that the origin of the hydrogen attached to the phosphorous is surface hydroxyl groups.
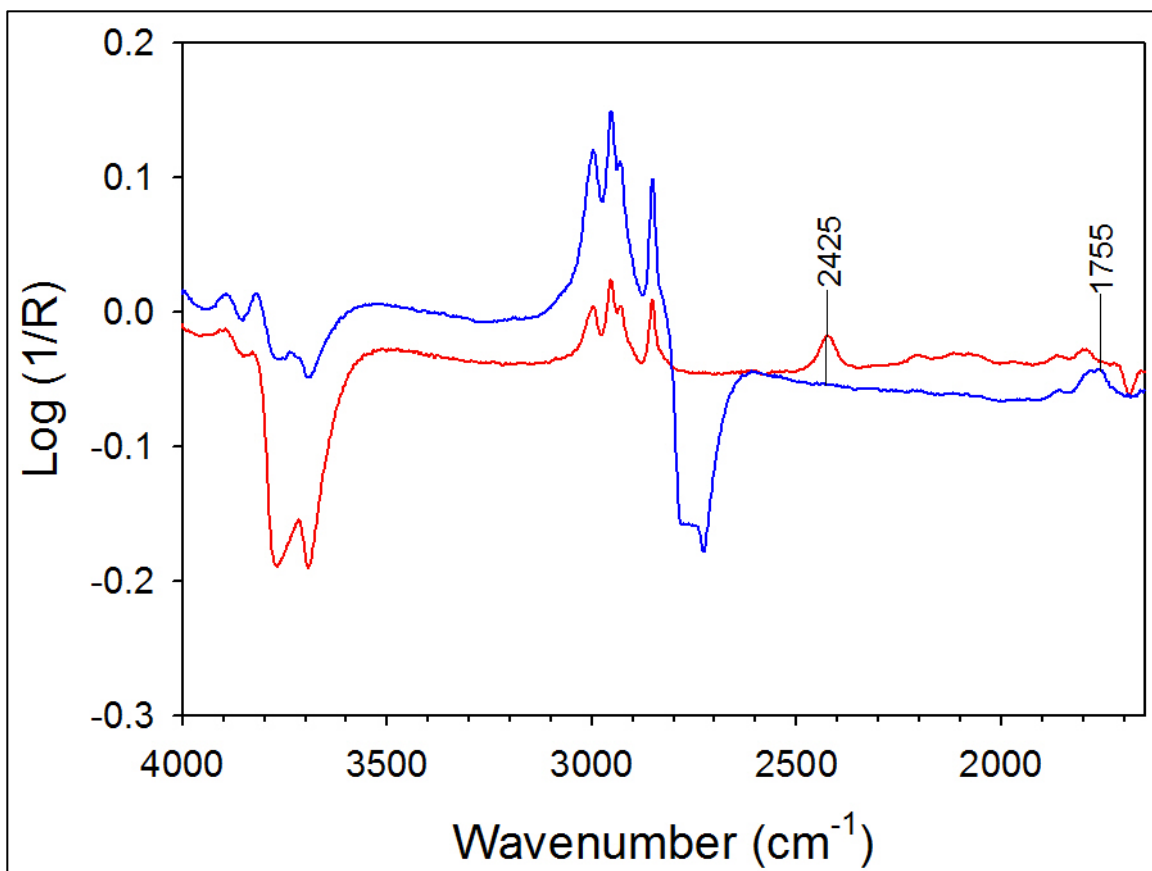
Figure 30. Spectral comparison of Zr(OH)₄ exposed to DMMP (red) and Zr(OD)₄ exposed to DMMP (blue).

<u>ii. Dimethyl Hydrogen Phosphite</u>

The other route taken to verify the assignment of the P-H bond formation was to dose a Zr(OH)$_4$ sample with dimethyl hydrogen phosphite (DMHP) in the same manner as in the DMMP experiments. The resulting spectrum compared with that from DMMP exposure, is shown Figure 31. The structural difference between DMHP and DMMP is that a hydrogen atom replaces the phosphyl-methyl in DMMP; structures compared Figure 27. When the DMHP initially adsorbs on the Zr(OH)$_4$ surface, the presence of a 2809 cm^{-1} band is noted, along with the expected P-H band at 2425 cm^{-1}. The frequency of the P-H stretch in DMHP adsorption validates the assignment of the P-H feature seen after long exposures of the solid to DMMP, and the presence of the 2809 cm^{-1} feature in

the DMHP exposure suggests that the DMHP species undergoes the same reaction with the zirconium hydroxide surface as seen with DMMP, i.e. cleavage of the P-OCH$_3$ bond to yield a surface bound bidentate phosphite in this case and a surface-OMe.
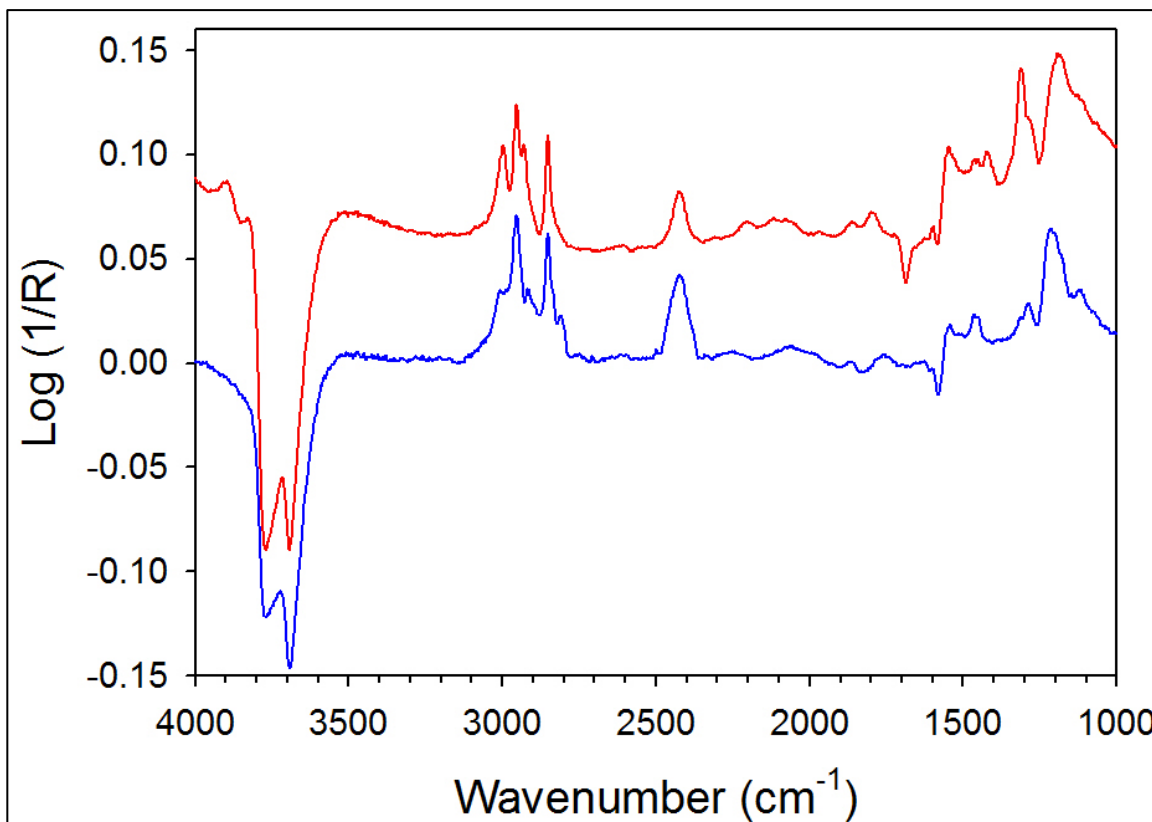
Figure 31. Spectral comparison of Zr(OH)$_4$ exposed to DMMP (red) and DMHP (blue).

iii. Time-Dependent vs. Coverage-Dependent Reaction

A final DRIFTS experiment was performed in order to elucidate more about the mechanism of the P-H formation during DMMP adsorption. In this test, a Zr(OH)$_4$ sample was prepared and dosed with DMMP in the same manner as previously explained, only with much less DMMP, 20 μmol instead of the 70 μmol used in earlier experiments, Figure 32. The result of this experiment show that DMMP adsorbs and reacts in the same manner as discussed above, with the last spectrum before evacuation, at 20 μmol, showing the five bands in the C-H stretching region. After evacuation the 2820 cm^{-1} band

52

has reduced in intensity but is still present, unlike with the higher exposure where this band is indistinguishable after evacuation. This is likely due to those surface-OMe species never competing over the site since there was a lower concentration of DMMP on the surface. The four DMMP bands are in the 1:1 ratio expected for MMP. There is no evidence for formation of a P-H containing species, even after sitting for three days under vacuum, indicating that the P-H formation is coverage-dependent rather than time dependent.
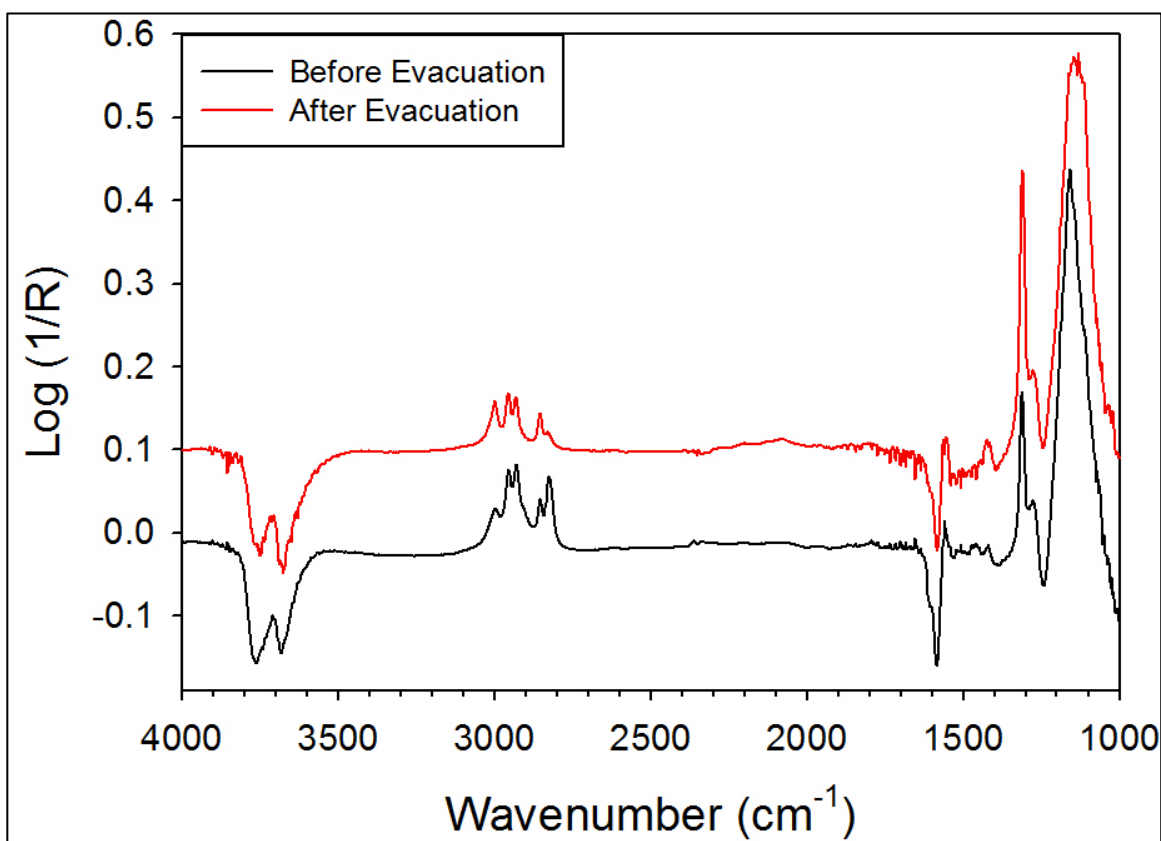
Figure 32. Low exposure of DMMP (~20 μmol) to Zr(OH)₄.

e. Reaction Products

Confirming that there is a P-H bond formation in the reaction leads to the necessary discussion of what product is being seen on the Zr(OH)$_4$ surface. Previous

studies have reported production of MMP and methylphosphonic acid (MPA), but nothing with a P-H bond.[14,19,23,71-73,84] The experiment using DMHP is in good agreement with the product seen to form from the DMMP exposure. To reiterate DMHP differs from DMMP by substitution of the P-CH$_3$ with a P-H. What this substitution would cause in the evolution spectra of Zr(OH)$_4$ exposed to DMMP is that as the v (P-H) band increases there would be a decrease in relative intensity of the v_a (CH$_3$.-P), v_s (CH$_3$.-P), δ_a (P-CH$_3$), and δ_s (P-CH$_3$) bands. The δ_a (P-CH$_3$), and δ_s (P-CH$_3$) bands do not exhibit the loss of intensity expected for a removal of the methyl group; the δ_a (P-CH$_3$) band is used as a representative in the graph above for both modes, Figure 29. The δ_a (P-CH$_3$) band exhibits the same behavior that was seen by the v_a (P-CH$_3$) and v_s (P-CH$_3$) discussed previously. However, it is evident that the δ_a (P-O-CH$_3$) band is seen to decrease in intensity with the growth of the P-H band, indicating that the DMMP has converted one of its P-O-CH$_3$ to P-H, leaving the product methyl methylphoshinate (MMPH) Figure 33. The P-H stretch is seen growing in prior to the decrease in the δ_a (P-O-CH$_3$), from 40-60 μmol, however, this is explained by additional adsorption of molecular DMMP. After the 60 μmol DMMP exposure is reached the v (P-H) and δ_a (P-O-CH$_3$) bands behave inversely relative to one another, including post exposure evacuation.

Figure 34 is a plot of the peak heights in the C-H stretching region, as used in Figure 26, but including post exposure evacuation. It is expressed as a function of exposure and emphasized the result seen with evacuation of the sample. All of DMMP C-H stretching bands show a significant reduction in rate of increase of peak height by 40 μmol DMMP exposure. This is simply due to the Zr(OH)$_4$ surface nearing saturation, which effectively reduces the probability the DMMP molecule will find a site on which

54

to adsorb. The change in the relative intensities of the C-H stretching bands from the highest exposure amount, 70 μmol, to the evacuated sample, are shown spectroscopically, in Figure 35 with an overlay (A), baseline corrected overlay of C-H stretching region (B), and side by side deconvolution (D and E). The C-H stretching region relative intensities after evacuation resolve as near 1:1 indicating the decomposition to MMP/MMPH. The behavior of the C-H stretching bands verifies the substitution of the phosphoryl-methoxy rather than the phosphoryl-methyl by hydrogen since the v_a (P-O-CH$_3$) and v_s(P-O-CH$_3$) bands show an obvious decrease in intensity where the v_a (P-CH$_3$) shows no decrease and the v_s (P-CH$_3$) shows only a slight decrease due to the loss of the remaining surface-OMe. The deconvoluted spectra, Figure 28D and E, are on the same vertical scale emphasizing that the bands corresponding to the surface-OMe are almost entirely absent and that the v_a (P-O-CH$_3$) and v_a (P-O-CH$_3$) bands have greatly reduced intensity, while the v_a (P-CH$_3$) and v_a (P-CH$_3$) bands remain similar to prior to evacuation.

It is noted here for clarification Figure 35C shows that integrating the v (P=O) stretch for exposure of 70 μmol during flow and after overnight evacuation yields 99.5 % correspondence indicating that no physiosorbed molecular DMMP has been removed from the Zr(OH)$_4$ surface rather that it has all reacted. There is also a notable shape change and shift since band is a combination of v (P=O) due to DMMP, MMP, and MMPH before evacuation, to MMP and MMPH, with little to no molecular DMMP, after evacuation. As an additional note it is possible that a MMP molecule could lose an additional methoxy leaving a highly surface coordinated methyl phosphonate (MP). However, this is believed to have occurred either at a very small amount or not at all in our reactions, as the v (P=O) would be expected to broaden to a much greater extent. The

DMMP would have to be present in order to keep the near 1:1 [P-O-CH$_3$]:[P-CH$_3$], since

if there were only MMP and MP species it would shift the ratio favorable to the [P-CH$_3$].
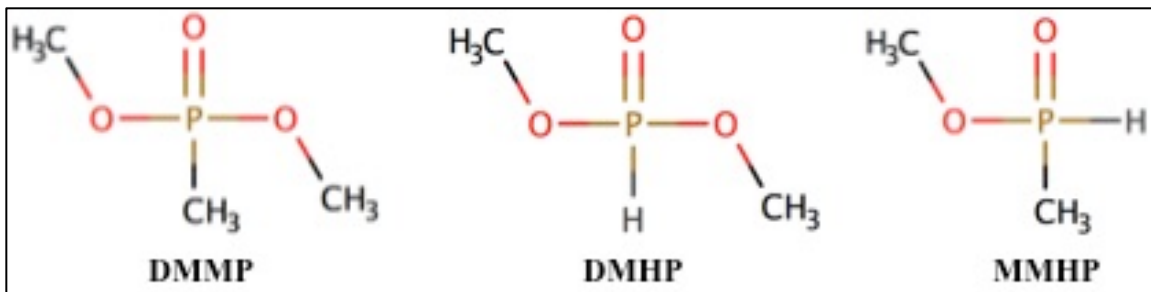
Figure 33. DMMP comparison to potential phosphonate/phosphite products with P-H stretch
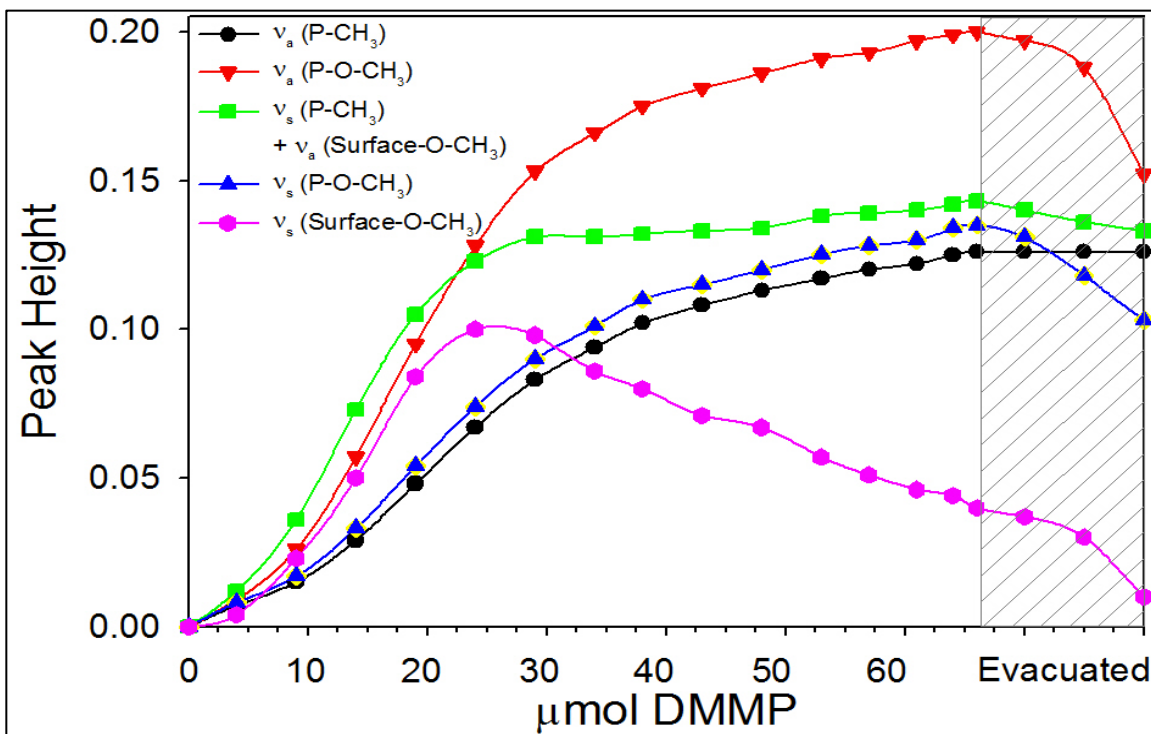
Figure 34. Evolution of C-H stretches in spectra of Zr(OH)$_4$ during DMMP exposure and after evacuation.
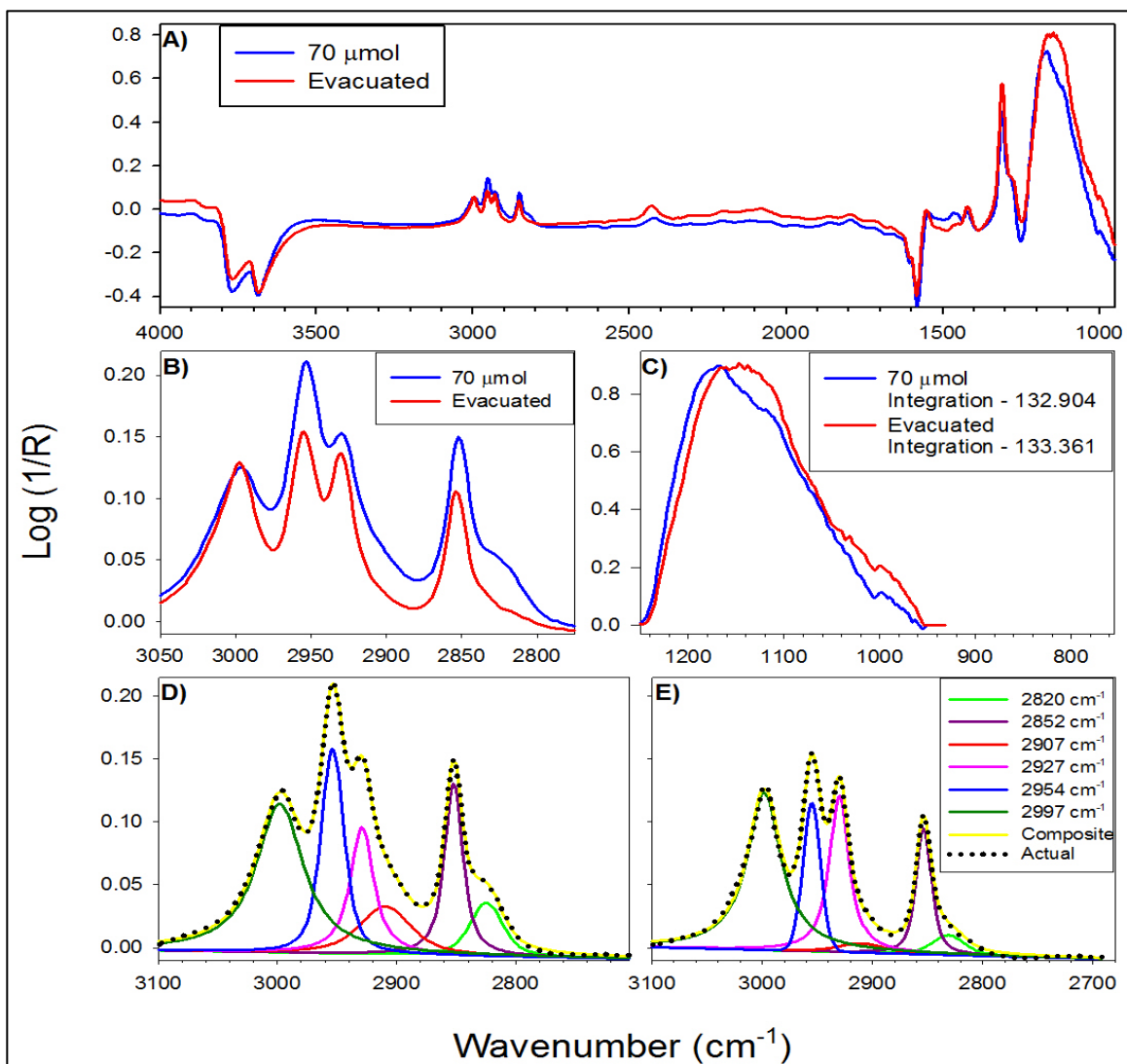
Figure 35. Comparison of before and after evacuation of 70 μmol of DMMP on Zr(OH)₄. (A) Raw data overlay. (B) Baseline corrected C-H stretching region overlay. (C) Baseline corrected ν(P=O) region. (D) Deconvolution of C-H stretching region before evacuation and (E) after evacuation.

i. Additional Products

In Figure 28, coinciding with the growth of the ν(P-H) band is the growth of a band at 1546 cm^{-1}. There is also slight growth of 2 other bands at 2078 cm^{-1} and 2198 cm^{-1} that would most likely be overlooked without the discussion later concerning post exposure heating. It is proposed here that these 3 bands are due to formation of carbon monoxide, which adsorbs to the surface. The 1546 cm^{-1} (1570 cm^{-1}) band is ascribed to a

bidenatate formate species by Ma *et al.* studying CO adsorption on zirconium polymorphs using DRIFTS.[85] Korhonen *et al.* proposed that the bidentate carbonate species comes from insertion of carbon monoxide or carbon dioxide into the terminal OH of monoclinic zirconia, Scheme 2.[86] Ma *et al.* also shows bands resembling the 2078 cm^{-1} and 2198 cm^{-1} in similar relative intensities ascribed to adsorbed linearly adsorbed CO at coordinatively unsaturated Zr^{4+} sites.[85] This is further validated by Li *et al.*[87] studying CO adsorption on CeO_2 who suggested that lower wavenumber emerges in greater intensity due to high amount of hydrogen bonding. These bands can also be seen in the low exposure experiment, Figure 32.
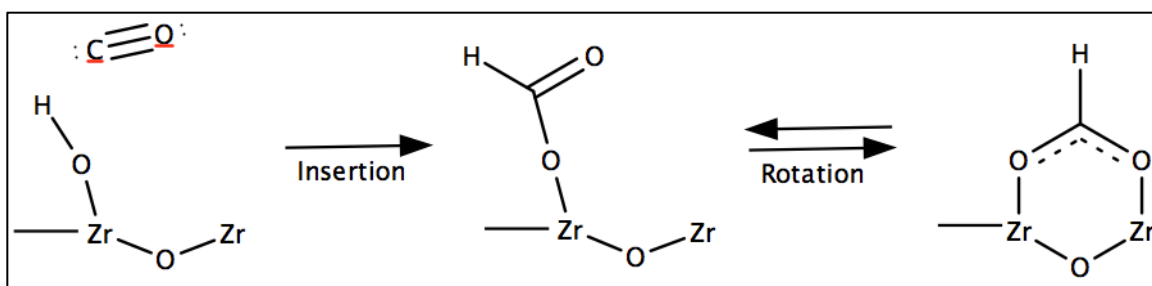
Scheme 4. Bidentate formate formation of Zr(OH)$_4$.[83]

The production of CO could possibly come from the decomposition of $CH_3OH \rightarrow CO + H_2$, which Croy *et al.* studied using Pt supported on various metal oxides. Their findings suggested that the results were dependent on the support used, and of the supports studied, ZrO_2 had the highest activity.[88] Matsumura *et al.* also studied this decomposition with Pd/ZrO_2, finding that at low temperatures it occurs with a low activation energy.[89] Due to both of these studies yielding a positive result with inclusion of ZrO_2 it is not unreasonable to suggest that ZrO_2 plays an important role. In a study by Ruiz-Rosas *et al.* electrospun zirconia nanofibers, prepared from a solution of zirconium (~16 %wt) acetate dilute in acetic acid with polyvinylpyrrolidone (6 %wt) added, were shown to active in MeOH decomposition yielding products, CO_2, CO, H_2, and H_2O.[90] We

suggest that due to the much higher reactivity of the $Zr(OH)_4$ over traditional ZrO_2,

coupled with the environment created by saturating the surface with

DMMP/MMP/MMPH catalyzes the methanol decomposition reaction.

2. Microreactor Studies

a. Methanol Production

The reaction profile curve is shown Figure 36. The concentration of MeOH in the

cell is the vertical axis and µmol of DMMP is the horizontal axis. The characteristic

reaction profile, described by Mitchell *et al.* includes an induction period, a rapid rise in

product concentration up to a maximum, followed by a slower decrease in the

concentration, which extends a relatively long period of time.[22] What is different and

interesting about using the $Zr(OH)_4$ substrate is that it virtually eliminates the induction

period. As soon as the DMMP flow is initiated, MeOH is seen spectroscopically. This is

an interesting phenomenon because what it infers is that the reaction proceeds at a rapid

rate, which is in good agreement with the work by Bandosz *et al.*, but also confirms as

discussed above that the $Zr(OH)_4$ substrate very weakly binds the methoxy, which

originates from the DMMP decomposition.[26] As a quantitative measure it is useful to

look at how many molecules of DMMP react per area of the substrate, synonymous with

molecules of methanol produced per nm^2, making the assumption each DMMP molecule

can lose one methanol. This value is calculated from integration of the methanol

production curve described in the experimental section. With a 30-minute N_2 purge of the

$Zr(OH)_4$ sample prior to DMMP exposure, it is seen that 0.85 molecules of DMMP react

per nm^2. $Zr(OH)_4$. With a 165-minute purge time this is increased to 1.1 molecules of

DMMP react per nm^2. Zr(OH)$_4$, compared to other various materials from a study by

Sheinker *et al.*, Table 4.[15]
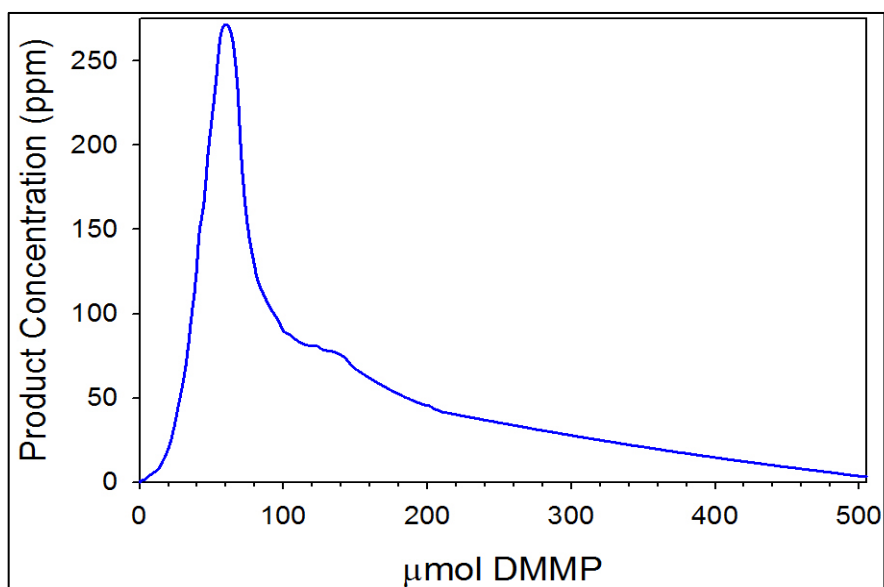
Figure 36. Gas phase methanol production profile from continual flow of DMMP through Zr(OH)$_4$.

Table 4. Comparison of volatile carbon products per unit area of various materials. *Sheinker *et al.*[15]

Sample	Surface Area (m^2/g)	Molecules Volatile Carbon nm^2 Zr(OH)$_4$
Zr(OH)$_4$	462	1.1
Sol-gel Alumina*	253	0.50
γ-alumina*	106	0.66
Alumina supported iron oxide*	74	0.76

b. DMMP Uptake

DMMP uptake was described using breakthrough testing, as the delay described

in the experimental section, with varying masses of Zr(OH)$_4$ in the microreactor. What

may be expected is that there would be a linear relationship between breakthrough

amount and mass. Figure 37 shows the breakthrough amount as a function the mass of

Zr(OH)$_4$, which does not appear linear. This is understandable as there is the additional

variable of diffusion through the powder as the mass (volume) of Zr(OH)$_4$ increases, as

with packed column chromatography. For the lower masses of $Zr(OH)_4$, which were used for determination of MeOH production, the DMMP uptake is 3-5 times the amount of total DMMP molecules decomposed.
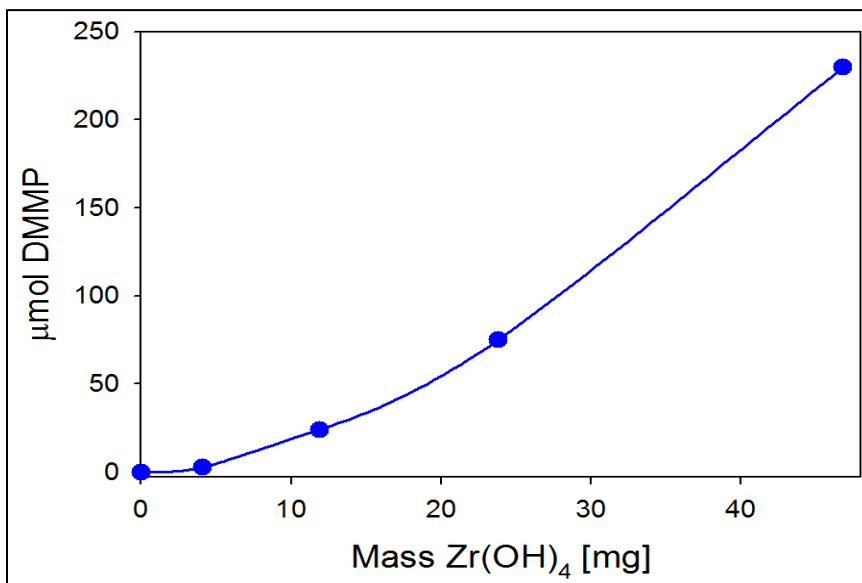
Figure 37. Effects of diffusion on DMMP uptake.

C. Temperature Effects

1. Pretreatment Temperatures

a. DRIFTS

The effects of pretreatment temperature, which is equivalent to surface dehydration, was examined in the next series of experiments. What is seen in the spectra Figure 38A, exposed to ~20 μmol DMMP, and Figure 38B, exposed to ~70 μmol DMMP, is that as pretreatment temperature increases the capacity of the $Zr(OH)_4$ to adsorb/decompose DMMP is greatly reduced. The lower capacity is evident even at the relatively low temperature of 80 ^{o}C. From previous TGA/DSC analysis it is known that most weakly bound H_2O and some chemisorbed H_2O species have been removed from the $Zr(OH)_4$ at this temperature. This implies the H_2O is a very important component in

61

the mechanism of both adsorption and decomposition of DMMP on the $Zr(OH)_4$ surface. The highest temperature pretreatment, 300 ^{o}C, yielded spectra indicating ~70 % reduction of the adsorption as was seen for room temperature. This value was obtained by integrating the C-H stretching region, as an average of low and high exposures in Figure 38. Additionally, surface-OMe showed a ~40 % reduction at 300 ^{o}C, obtained in a similar manner by integrating the v_s (surface-OMe) band.
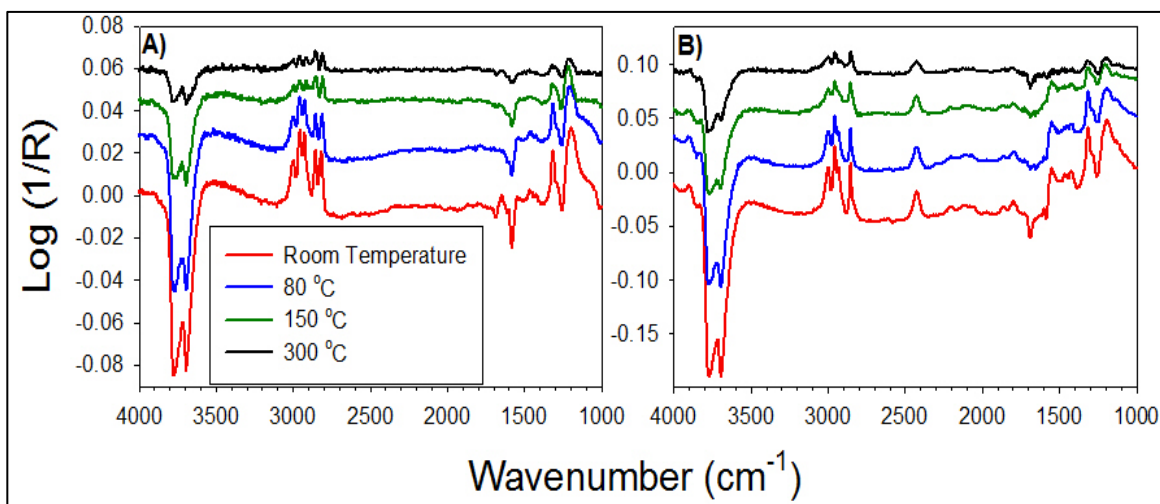
Figure 38. Effects of pretreatment temperatures on the ability of $Zr(OH)_4$ to adsorb/decompose DMMP. (A) Low exposure (~20 µmol). (B) High exposure (~70 µmol).

b. Microreactor Results and Comparison to DRIFTS

 The same procedure of was applied in the microreactor of applying different pretreatment temperatures to $Zr(OH)_4$. Samples were heated to the temperatures 21, 80, 150, and 300 ^{o}C with flow of N_2 at 10 mL/min for a 15-minute ramp time to the respective temperature with a hold for 2 hours, followed by a 30-minute cooling period prior to initiating flow of DMMP.

 The results of the DRIFTS experiment were compared with the microreactor in terms of methanol production as well as DMMP uptake, Tables 5 and 6, and Figure 39. For methanol production value in the DRIFTS the integrated area of the v_s (surface-OMe)

in the DRIFTS spectrum at each temperature was compared to the molecules of methanol produced per nm^2. Likewise, DMMP uptake values from the DRIFTS come from integration of the entire C-H stretching region was compared to the microreactor values from DMMP uptake per nm^2. There was <10 % difference between the two experiments in all cases.

From the results we can see that DMMP uptake is affected to a much greater extent than decomposition, ~70% reduction as compared to ~40 %, respectively. The heating of the $Zr(OH)_4$ has likely reduced the number of active sites by producing H_2O from the condensation of neighboring OH sites on the surface, responsible for the decomposition. Additionally this heating removed physiosorbed and chemisorbed H_2O species, which assist in H-bonding molecular DMMP. DMMP uptake involves both of these procedures where decomposition is only effected by loss of the active OH sites; thus, the DMMP uptake shows significantly more dependence of the pretreatment temperature.

It is interesting to note that with the longer purge time here, 165 minutes, a 30 % increase of MeOH production was seen over the previously discussed experiment with only a 30-minute purge time, from 0.85 to 1.1 reacted molecules of DMMP per nm^2. What was observed in the IR spectra during the N_2 purges is H_2O and CO_2. The CO_2 reaches very low levels by the end of either purge, where the H_2O concentration is still quite high, especially for the 30-minute purge. Weakly physiosorbed H_2O seems to be the species responsible for the lower levels of MeOH production with the shorter purge time, indicating that humidity could be an important factor in application in the field. It is then reasonable to conclude, since the MeOH production also decreases as the temperature

increases, not only are these weakly adsorbed H_2O molecules displaced but that condensation of neighboring surface OH sites, discussed in the TGA, has eliminated some active decomposition sites.

Table 5. MeOH production on Zr(OH)₄ at varying temperature in DRIFTS and microreactor.

Temperature (^{o}C)	RT	80	150	300
Molecules MeOH nm^2 Zr(OH)$_4$	1.1	0.93	0.87	0.68
Integrated 2820 cm^{-1} band	0.567	0.452	0.403	0.335

Table 6. DMMP uptake at varying temperature in the DRIFTS and microreactor.

Temperature (^{o}C)		RT	80	150	300
Molecules DMMP nm^2 Zr(OH)$_4$		3.4	2.8	1.6	1.1
Integrated CH Stretching Region	~20 μmol	5.108	3.961	1.682	1.127
	~70 μmol	7.201	5.215	4.324	2.695
	Average	6.184	4.588	3.003	1.961
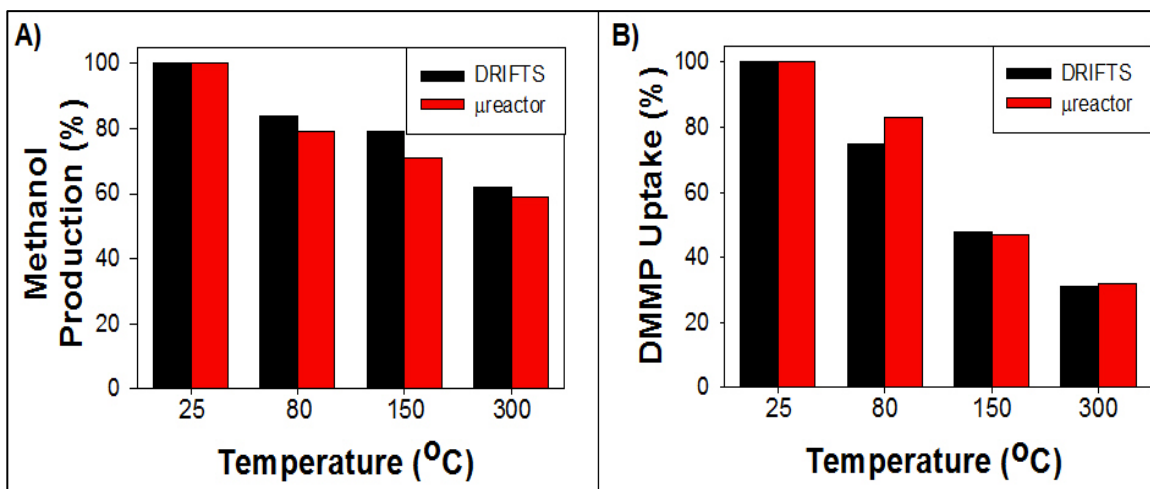
Figure 39. Comparison of results of DRIFTS and microreactor on pretreatment temperature effects on (A) methanol production and (B) DMMP uptake.

2. Post-exposure heating

        $Zr(OH)_4$ samples were saturated with DMMP and subsequently heated to discreet

temperatures in order to determine if further reaction could be induced. For both the

DRIFTS and microreactor setup the temperatures 25, 50, 100, 150, 200, 250, 300, 350,

and 400 $^{\circ}$C were investigated under constant flow of N_2.

a. DRIFTS

        For the DRIFTS experiment spectra, Figure 40, and plot of band intensities,

Figure 41, what was observed was that at 25 $^{\circ}$C no further reaction occurs. In the

transition between 25-50 $^{\circ}$C and clearly once 50 $^{\circ}$C is reached there is slight loss of

molecular DMMP, evidenced by the proportional decrease of intensity of all C-H

stretching bands, as well as 1466 cm^{-1}, 1423 cm^{-1}, 1315 cm^{-1}, and 1198cm^{-1}

corresponding to DMMP. Heating to 100 $^{\circ}$C yields greater loss of intensity in the C-H

stretching region in proportion with what would be expected for loss of a methoxy group

from the DMMP combined with additional molecular DMMP loss. The loss of the

methoxy is greatly supported by the much greater reduction in intensity of the δ_a (CH$_3$-O)

band over that of the δ_a (CH$_3$-P) band. A slight growth in the v_s (surface-OMe) band is

also seen, however, it is proposed that since there is an abundance of desorbed molecular

DMMP, which has been shown to readily displace MeOH, and there is added energy

from heating, the MeOH is likely to be eliminated from the site immediately upon

formation. This process continues in consistently increasing amounts from 100-250 $^{\circ}$C.

At 250 $^{\circ}$C the band at δ_a (CH$_3$-O) is completely gone and changes in relative intensities of

the C-H stretching bands become more apparent. Between 300-400 $^{\circ}$C the v_a (P-CH$_3$) and

v_s (P-CH$_3$) bands quickly become the dominant bands with significant loss of the v_a (P-O-CH$_3$) and v_s (P-O-CH$_3$) bands. In this temperature range, molecular DMMP is no longer desorbing and the only changes seen are due to loss of methoxy from adsorbed MMP species. At 400 °C the spectra show at least 50 % reduction of intensity of the v_a (P-O-CH$_3$) and v_s (P-O-CH$_3$) bands, indicating that all DMMP molecules have lost one of the methoxy groups as methanol and that many of the other methoxy groups from the MMP/MMPH species have been lost as well. At 300 °C there is an increase in intensity and sharpness of the v (P-H) band that continues until 400 °C. Also at 300 °C and continuing until 400 °C growth of two overlapping bands are observed at 2078 cm^{-1} and 2198 cm^{-1}, previously assigned to CO species. Throughout the heating the v (P=O) band steadily red shifts, and it is clearly evident by the 400 °C spectrum that the shape has changed, and as before this is attributed to change in speciation. The integration of this band at 400 °C showed ~15 % reduction indicating that some loss of phosphorous containing species did occur.
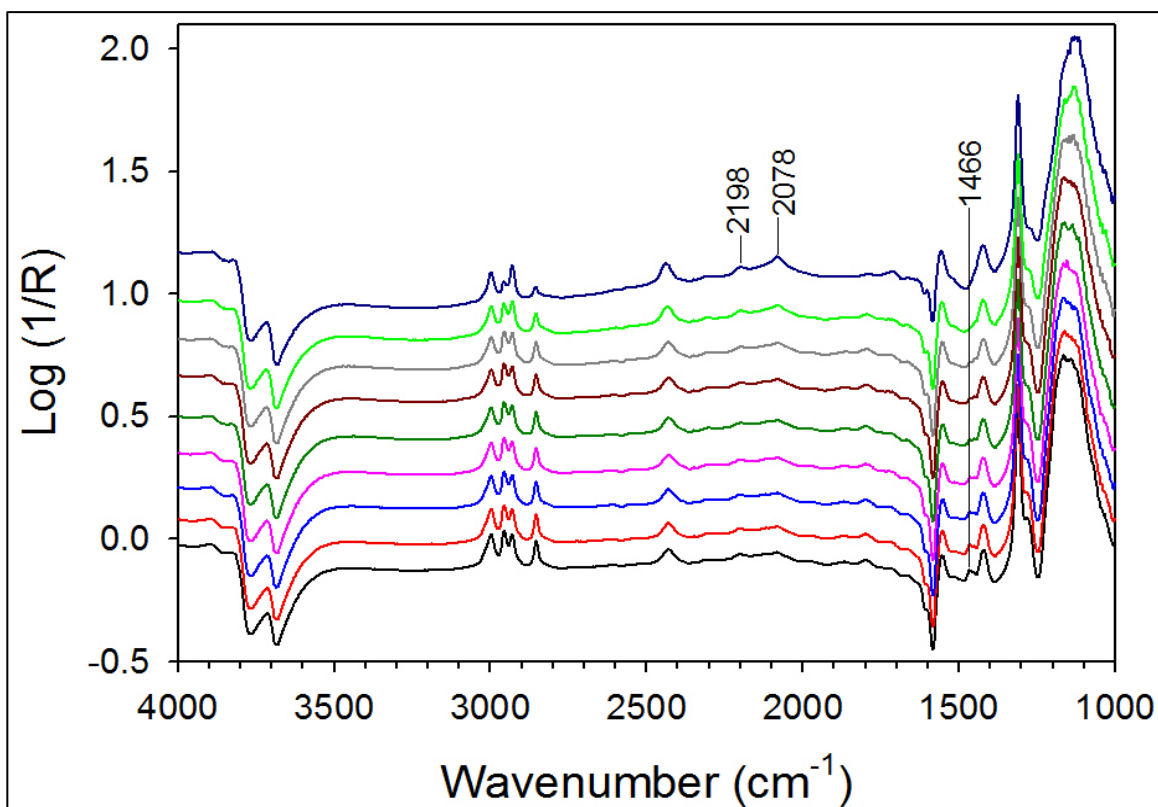
Figure 40. DRIFTS spectra evolution of post-exposure to DMMP heating of Zr(OH)$_4$. 25 (black), 50 (red), 100 (blue), 150 (pink), 200 (green), 250 (maroon), 300 (gray), 350 (lime), and 400°C (navy).
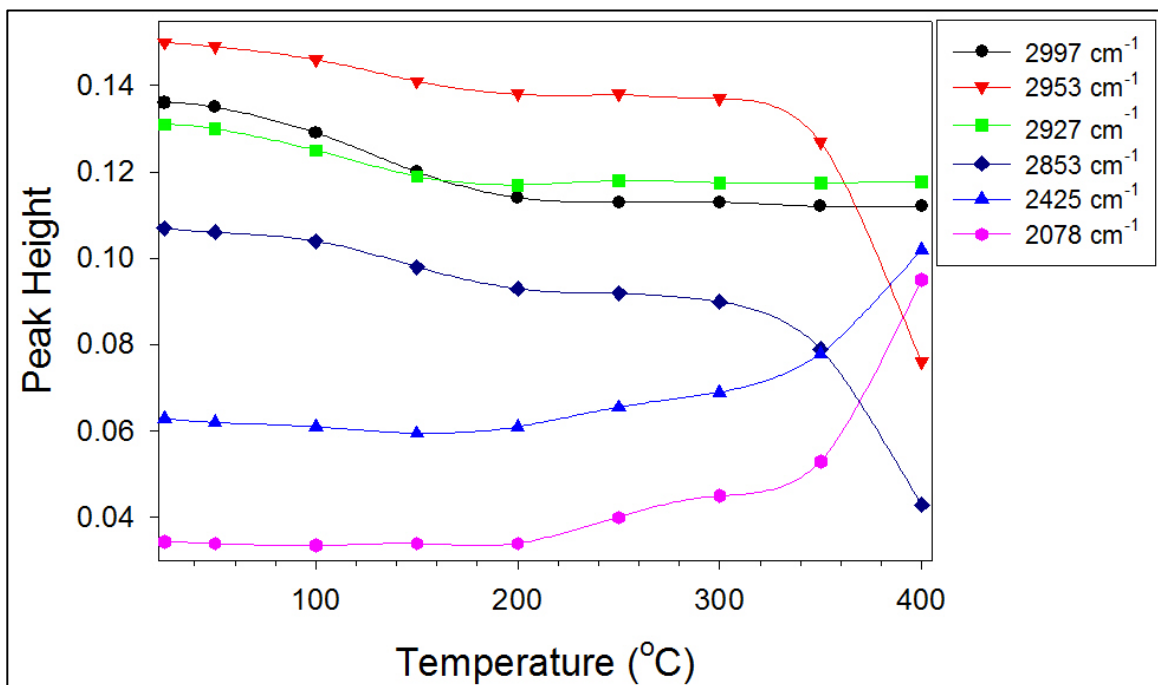
Figure 41. Various bands monitored from the DRIFTS spectra as a function of temperature for post exposure heating.

b. Microreactor

As before the micro reactor results are in agreement with what was observed in the DRIFTS experiment. Absorbances of emerging compounds are plotted as a function of temperature for each compound seen emerging into the IR cell, Figure 42. The absorbance of each compound, though concentration dependent, does not necessarily represent the compound that has the highest concentration due to the effects of different molar absorption coefficients (ε), in $A=\varepsilon bc$.

Molecular DMMP is seen in small amounts throughout the entire experiment starting at the interval between 25-50 $^{\circ}$C. MeOH production starts on the ramp from 50-100 $^{\circ}$C and reaches its peak intensity at 250 $^{\circ}$C. MeOH production from 250-400 $^{\circ}$C continually decreases but is still present. Between 250 and 300 $^{\circ}$C emergence of carbon monoxide is observed with bands centered at 2115 cm^{-1} and 2174 cm^{-1}, which confirms our prediction from the DRIFTS experiment. The CO band intensity reaches its maximum at 400 $^{\circ}$C, as it did in the DRIFTS experiment. A result not seen in the DRIFTS experiment is the formation of dimethyl ether, evidenced by the PQR branches from the symmetric rocking of the methyl groups at 1168 cm^{-1}, 1178 cm^{-1}, and 1191 cm^{-1}. Dimethyl ether first emerges between 50 and 100 $^{\circ}$C and reaches a maximum intensity at 300 $^{\circ}$C. The production of dimethyl ether then continually decreases, ceasing at 400 $^{\circ}$C. It is again proposed, as with the MeOH, that this product so weakly binds to the $Zr(OH)_4$ it is gone before it can be observed in the DRIFTS setup. Another notable difference in the micro reactor experiment is the continuous production of CO_2 and H_2O from the sample during heating. This is not seen in DRIFTS since they immediately leave as gas-phase products.
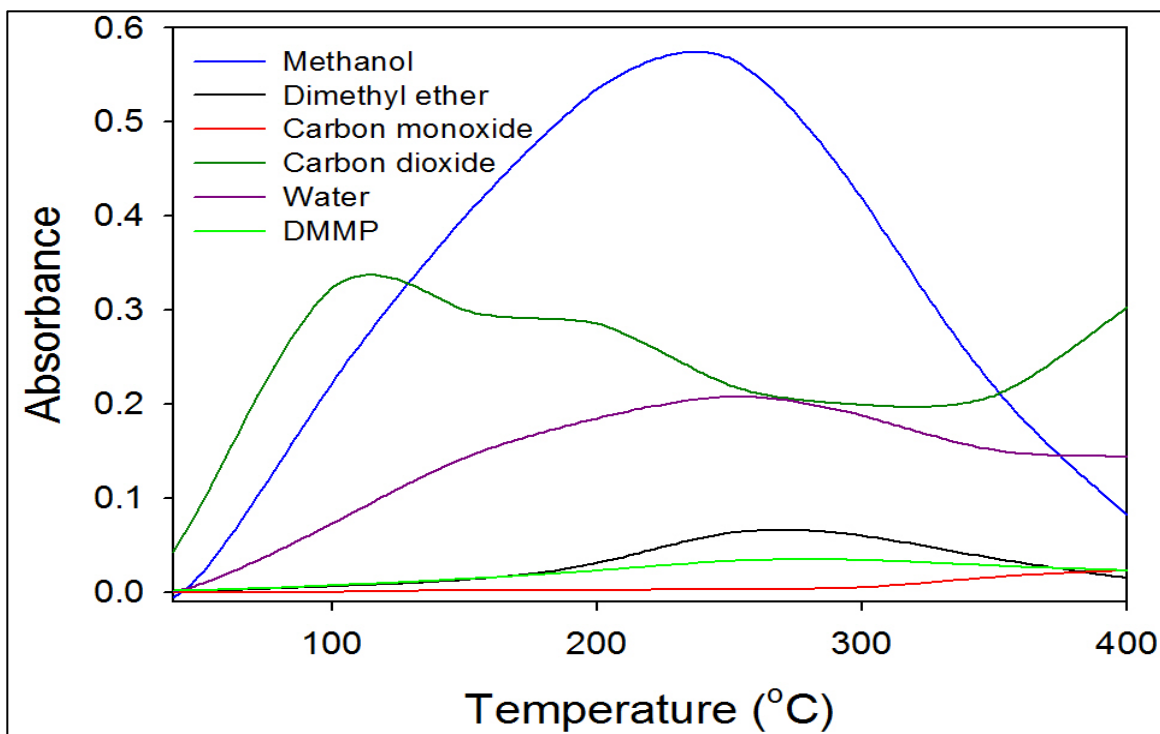
Figure 42. Products seen during post exposure heating of Zr(OH)$_4$ in microreactor, absorbance recorded as a function of temperature.

D. Nano-Zr(OH)$_4$

Two nano-zirconium hydroxide materials, commercial and a synthesized suspension, were assessed for increased or different activity from that discussed above. Both were tested using DRIFTS and showed the same reaction as discussed above for the 125 μm Type B Zr(OH)$_4$. The Type B Zr(OH)$_4$ was used to make the suspension Zr(OH)$_4$, thus, no different reaction was expected to occur, however, the commercial material had a potential due to different synthesis procedure. Neither of the nano-Zr(OH)$_4$ showed a different reaction from what was seen with the 125 μm Type B Zr(OH)$_4$. There is evidence in the spectra of extended activity of the commercial nano-Zr(OH)$_4$ seen by a shift of the inflection point of the v_s (surface-OMe) band, from ~25 μmol DMMP exposure to ~30 μmol DMMP exposure, Figure

69

43. The Zr(OH)$_4$ suspension appeared to show either prolonged MeOH production or increase in affinity for the MeOH, however, more Zr(OH)$_4$ suspension needs to be made and tested for confirmation. The microreactor results support the evidence seen in the DRIFTS study. The reaction profile of the nano-Zr(OH)$_4$ is the same as with 125 μm Zr(OH)$_4$, however, the total MeOH production of the nano-Zr(OH)$_4$ is much higher. The nano-Zr(OH)$_4$ produced 1.2 molecules of methanol produced per nm^2 with a 30 minute purge time where with the same purge time the 125 μm Zr(OH)$_4$ produced only 0.85 molecules of methanol produced per nm^2. This results also allows us to conclude that all MeOH produced from DMMP decomposition does not chemisorb to the surface since the DRIFTS shows ~25 % increase in surface-OMe, however, the microreactor shows over 40 % increase in methanol production per nm^2.
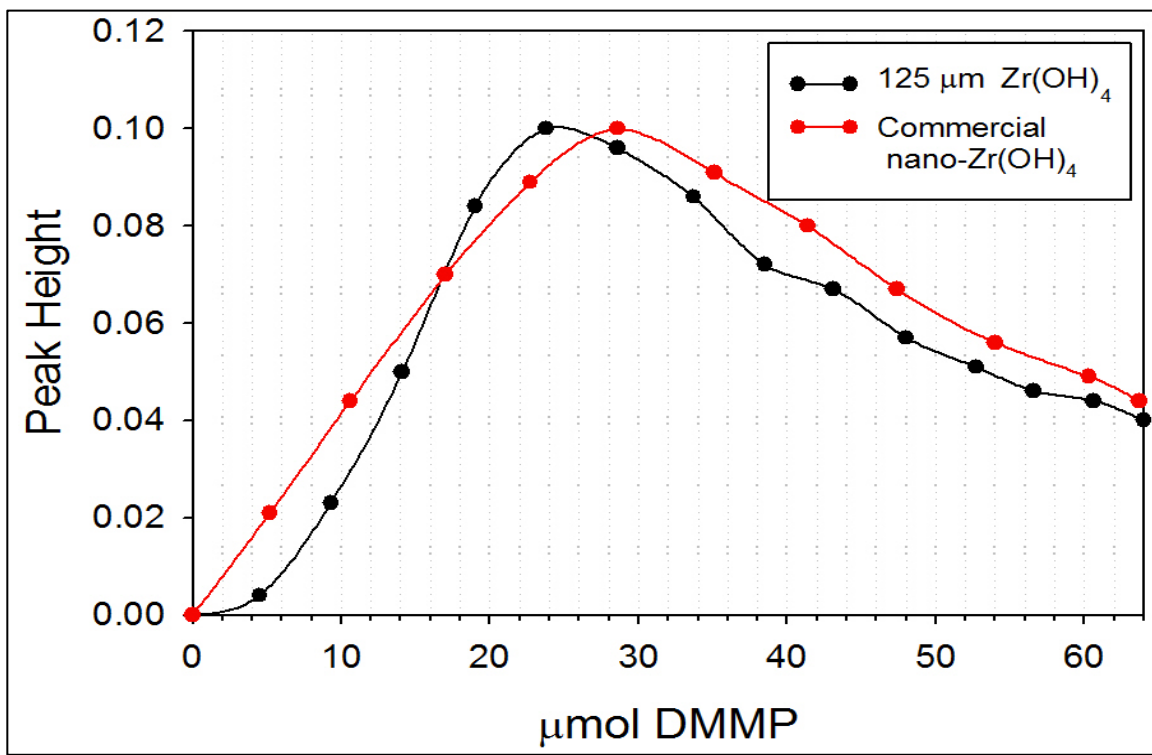
Figure 43. Comparison of the DRIFTS ν_s(surface-OMe) band profile from 125 μm Zr(OH)$_4$ and nano-Zr(OH)$_4$ as a function of exposure.

CHAPTER IV. METAL-ORGANIC FRAMEWORKS RESULTS

A. Thermogravimetric Analysis

The TGA thermograms, shown Figure 44, of the MOFs studied, UiO-66, UiO-66-NH$_2$, and UiO-67, were obtained to ensure structural integrity after long-term storage of the MOFs. The initial sharp loss seen to some extent in all three MOFs is due to loss of the solvent used in synthesis, dimethyl formamide (DMF).[91-94] UiO-66 and UiO-66-NH$_2$ show approximately 20 %mass loss from DMF, ~20 %, whereas the UiO-67 shows less than 10 %. This probably is due to the pore size of the MOFs. UiO-66 and UiO-66-NH$_2$ have very similar pore size due to using the same BDC linker, the later functionalized with an amine, where the UiO-67 with the BPDC linker greatly enhances the pore size. During the drying process of the MOFs after synthesis the more DMF is removed from UiO-67 than UiO-66 or UiO-66-NH$_2$ due to the larger pore size allowing easier diffusion out of the structure, thus, DMF present in smaller amounts in UiO-67 during TGA analysis. After the removal of the solvent the prolonged mass loss is due to removal of H$_2$O from the SBUs, dehydration, Zr$_6$O$_4$(OH)$_4$$\rightarrow$Zr$_6O_6$ + 2H$_2$O.[91,92] UiO-66-NH$_2$ exhibits an additional feature around 150 $^{\circ}$C which corresponds to "excess linker" burning.[91] UiO-66-NH$_2$ also exhibits lower thermal stability with complete breakdown nearly 100 $^{\circ}$C lower either UiO-66 or UiO-67, at 380 $^{\circ}$C rather than 480 $^{\circ}$C. In a study by Katz *et al*. UiO-66 and UiO-66-NH$_2$ exhibited similar thermal stability and it is unclear why the results here do not reflect that.[91]

The lower thermal stability has been attributed to synthesis temperature by Wiersum

when comparing their UiO-66 thermal stability to literature values.[93] It is clear from the

many studies including the TGA of the UiO family of MOFs that synthesis conditions

can greatly affect the stability since breakdown is seen from 450-600 °C.[91-94] Prior to

TGA the powders were white for UiO-66 and UiO-67, and yellow for UiO-66-NH$_2$, after

the heating all materials were blackened from the combustion of the linkers, shown

Figure 45.
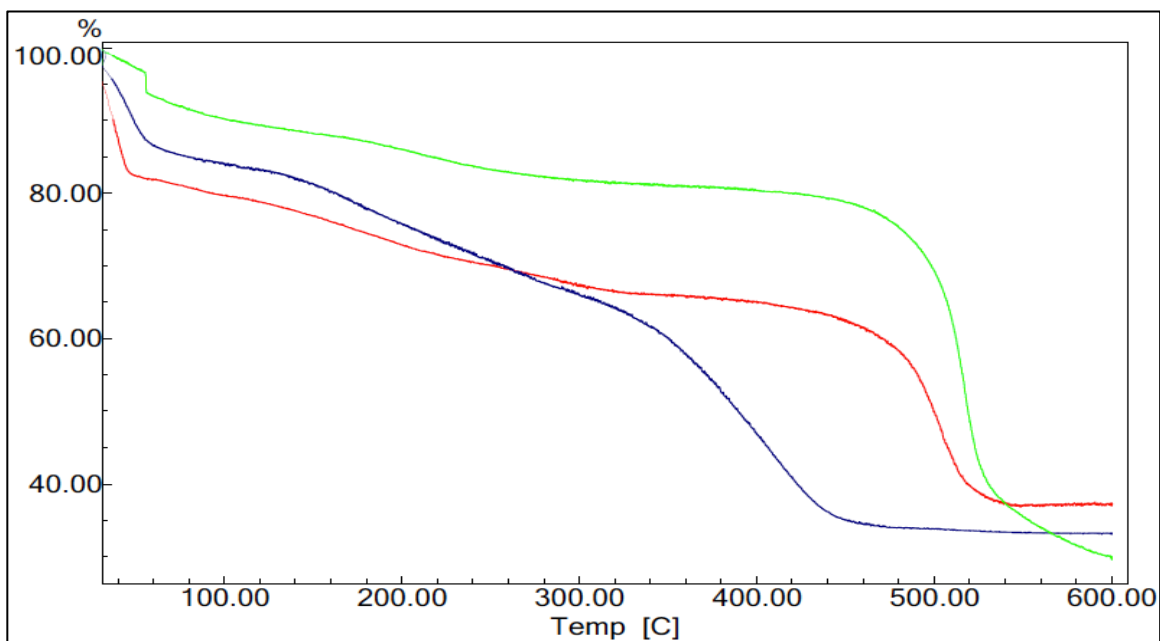
Figure 44. TGA curves of UiO-66 (red), UiO-66-NH$_2$ (navy), and UiO-67 (lime).
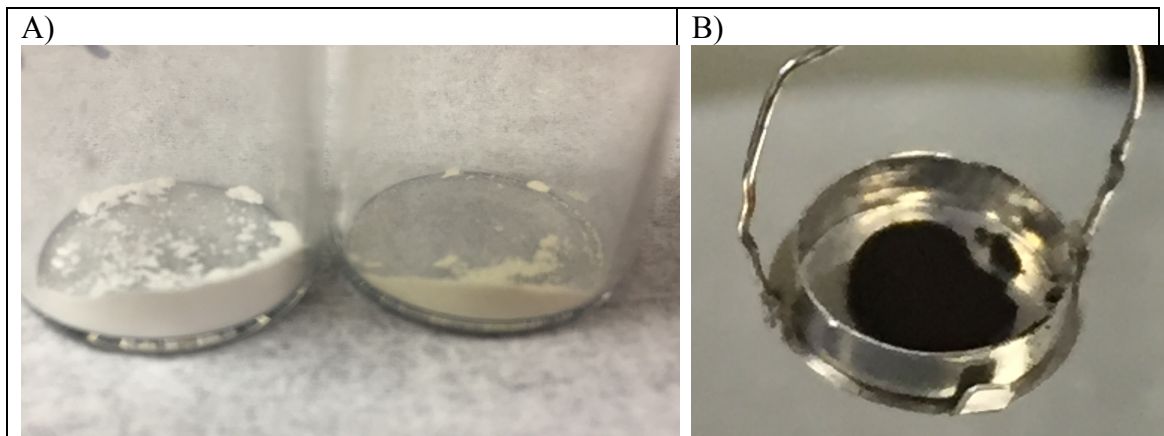
Figure 45. UiO-66 and UiO-66-NH$_2$ (A) and UiO-66 after heating in TGA (B).

B. Band Assignments

Much effort was expended between varying member of the ongoing collaboration funded by the Defense Threat Reduction Agency (DTRA), using theory, computation, experiment, and literature comparisons to assign vibrational modes to the Zr_6 based MOFs: UiO-66, UiO-67, and MOF-808, Table 7.[48,78,95-105] Wang *et al.* include these assignments in an article discussing reaction of DMMP on Zr_6 based MOFs.[51]

Table 7. Observed vibrational wavenumbers (cm^{-1}) for clean Zr_6-based MOFs and band assignments.
ν: bond stretching, ρ: rocking (in plane), δ: planar angle bending, β: in planar bending, γ: out-of-plane bending (wagging), ϕ: deformation, χ: aromatic ring breathing, i.P: in plane, o.o.p: out of plane, sh: shoulder[51]

Mode	UiO-66 cm^{-1}	UiO-67 cm^{-1}	MOF-808 cm^{-1}
ν(ZrO−H)$_{node, free}$	3674	3674	3674
ν(COO−H)$_{linker, free}$		3616	3585
ν(CH)$_{linker}$	3130 3083 3061	3075 3061 3048 3015	3087
Overtone	2800-2000	2800-2000	
ν(COZr)$_{bidentate}$+ν(COO)$_{i.p}$+ν(C=C)+β(CH)	1662-1520	1638-1471	1646-1500
β(CH)+ν(C=C)	1507		
ν(COZr)$_{bidentate}$+ν(COO)$_{o.o.p}$+δ(OH)+β(CH)	1477-1329	1471-1321	1500-1219
ν(C=C)+δ(C=C-C)	1320	1315	
ν(CO)	1300-1260	1269	
ν(C-C)+β(CCH)+ δ(OH)+γ(CCC)ϕ χ(ring)		1180	
β(CH)+δ(OH)+χ(ring)	1158	1154	
β(CH)+ν(C=C)+χ(ring)	1105	1121	1112
β(CH)+ν(C=C)+γ(CCC)ϕ χ(ring)		1106	
ν(CO)+δ(OH)	1088		
ν(CO)+δ(OH)	1058		
γ(CCC)ϕ+δ(OH)+χ(ring)	1019	1021	1054
χ(ring)+ γ(ring)		1007 974 964	942
ρ(CH)	885 824 816	876 856 843 801	823 804
ν(Zr-O)+γ(CCC)ϕ+ρ(CH)		771	790
ν(Zr-O)+γ(COO)ϕ+ρ(CH)		753	760

One experiment performed by myself at Virginia Tech for band assignment was the deuteration of UiO-66. This was performed on a UiO-66 sample pressed into a tungsten mesh that was then put into a stainless steel ultrahigh vacuum system equipped a Bruker IFS 66v/S spectrometer, in conjunction with a mercury cadmium telluride (MCT) detector, that were coupled to the UHV chamber via KBr view ports located on either side of the sample. Each of the spectra was collected at a resolution of 2 cm^{-1} with a 2 mm aperture for 100 scans. The spectra of MOFs were recorded by using a blank spot on the tungsten mesh as the background. The deuteration was accomplished by heating the evacuated UiO-66 sample in the UHV chamber to 300 $^{\circ}$C until the MOF was completely dehydrated, shown to occur in the TGA curve by 300 $^{\circ}$C, followed by dosing D_2O at 1 torr for 30 minutes, resulting spectra shown Figure 46. This OH→OD substitution was useful in determining that the bands at, 1477-1329, 1158, 1088, 1058, and 1019 cm^{-1} involved the OH species, rather than only the obvious ν (ZrO-H) at 3674 cm^{-1}
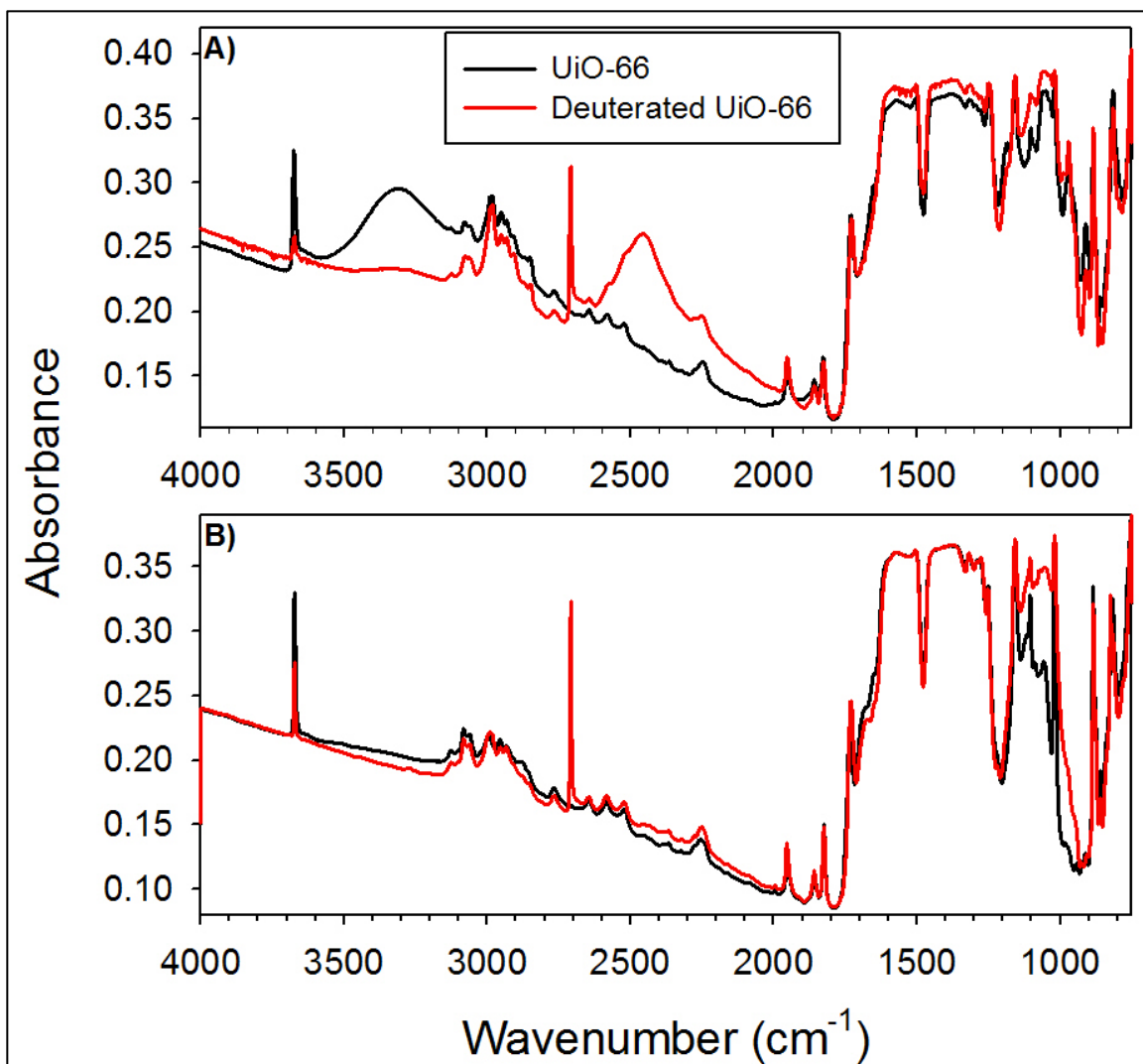
Figure 46. Transmission Infrared comparison of normal and deuterated UiO-66 with (A) and without (B) physiosorbed H₂O/D₂O.

C. DRIFTS

1. UiO-66

a. Pristine UiO-66 (Transmission Infrared Spectroscopy at Virginia Tech)

It has been proposed that decomposition of DMMP is only possible on UiO-66 in the presence of defect sites.[51-52,106,107] In the case of pristine UiO-66, as shown by Wang *et al.* there is no reaction seen with DMMP and it is solely able to physiosorb, which is easily removed by thermal treatment.[51] The spectra shown in Figures 47 and 48 were

collected using the stainless steel UHV system described above. The difference spectrum prior to thermal treatment, Figure 48, indicates that the DMMP is present as only molecular DMMP, not having undergone decomposition, since it maintains the 2:1, [P-O-CH$_3$]:[P-CH$_3$] intensity ratio. After heating, the spectrum returns to an almost perfect match of the original; indicating that all DMMP has been removed without decomposition, Figure 47.
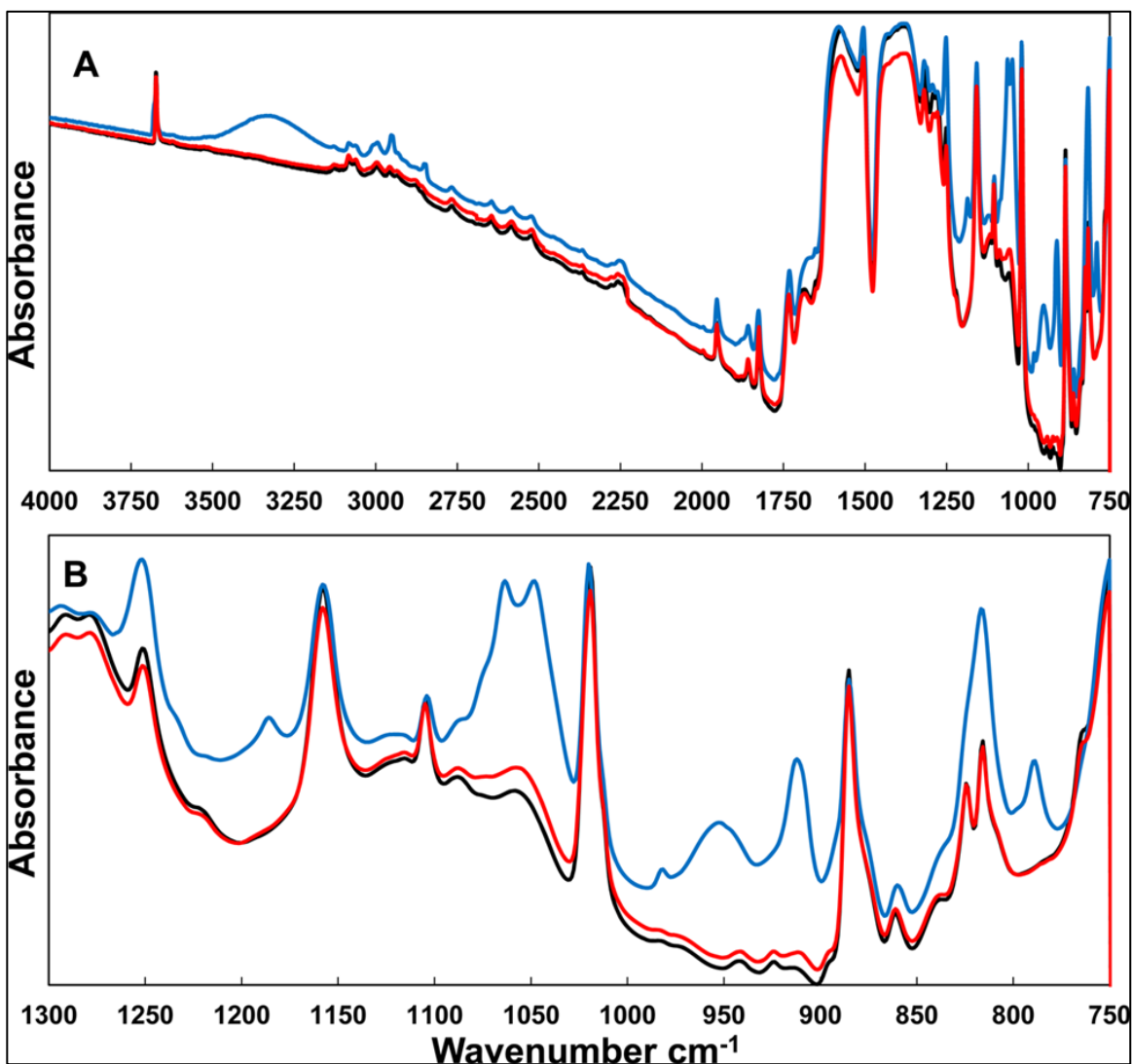
Figure 47. IR spectra for the mid-IR region (A) and the "fingerprint" region (B) of UiO-66 (top) before DMMP exposure (black), after DMMP exposure (blue), and after post exposure thermal treatment to 600K (red).[51]
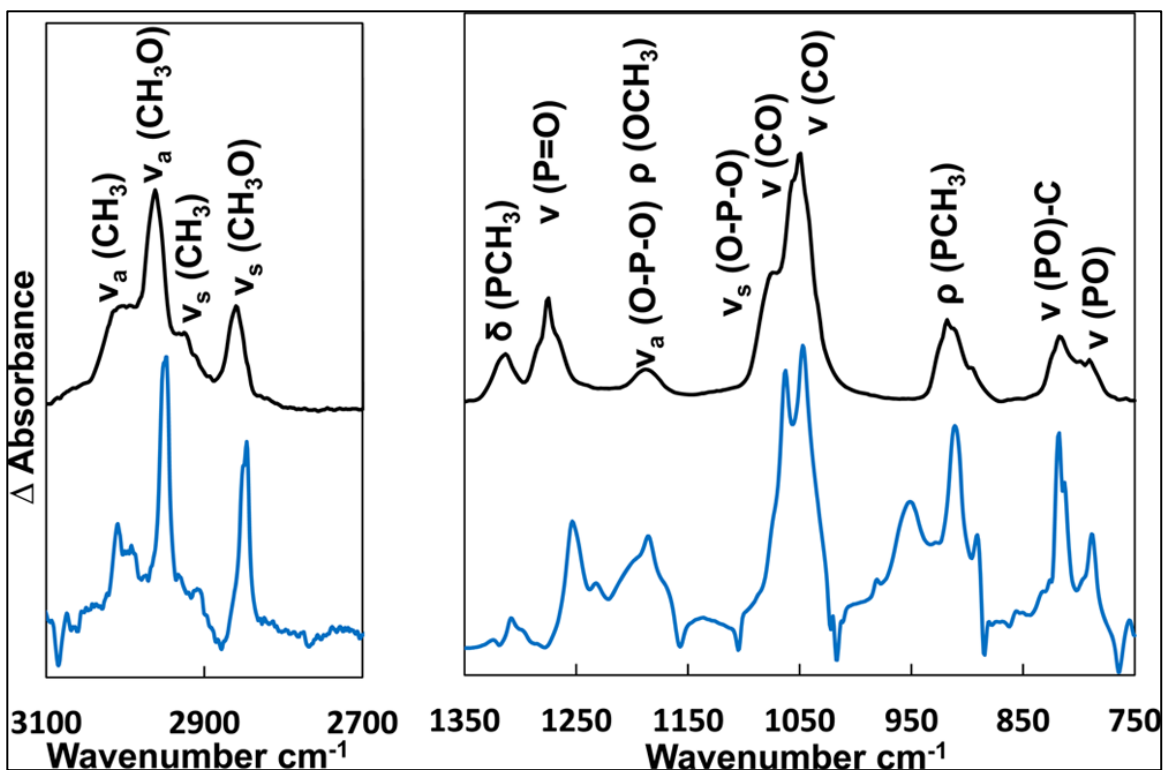
Figure 48. Gas phase DMMP (black) and difference spectra of DMMP adsorbed onto UiO-66 (blue) at C-H stretching region (left) and low wavenumber region (right).[51]

b. Reactive UiO-66 (DRIFTS at Kennesaw State University)

The spectra obtained at the end of exposing UiO-66 to 70 μmol DMMP and after evacuation, shown Figure 49, are rich in detail and seem to show a result similar to that seen with the $Zr(OH)_4$ work albeit with some stark differences including much higher amount of H-bonding occurring. The bands at 3011, 2955, 2907, and 2849 cm^{-1} are due to absorbances of the DMMP and appear, after overnight evacuation, to have relative intensities resembling MMP rather than DMMP. There are an additional two prominent bands in the C-H stretching region at 2820 and 2717 cm^{-1} that must be due to decomposition products.
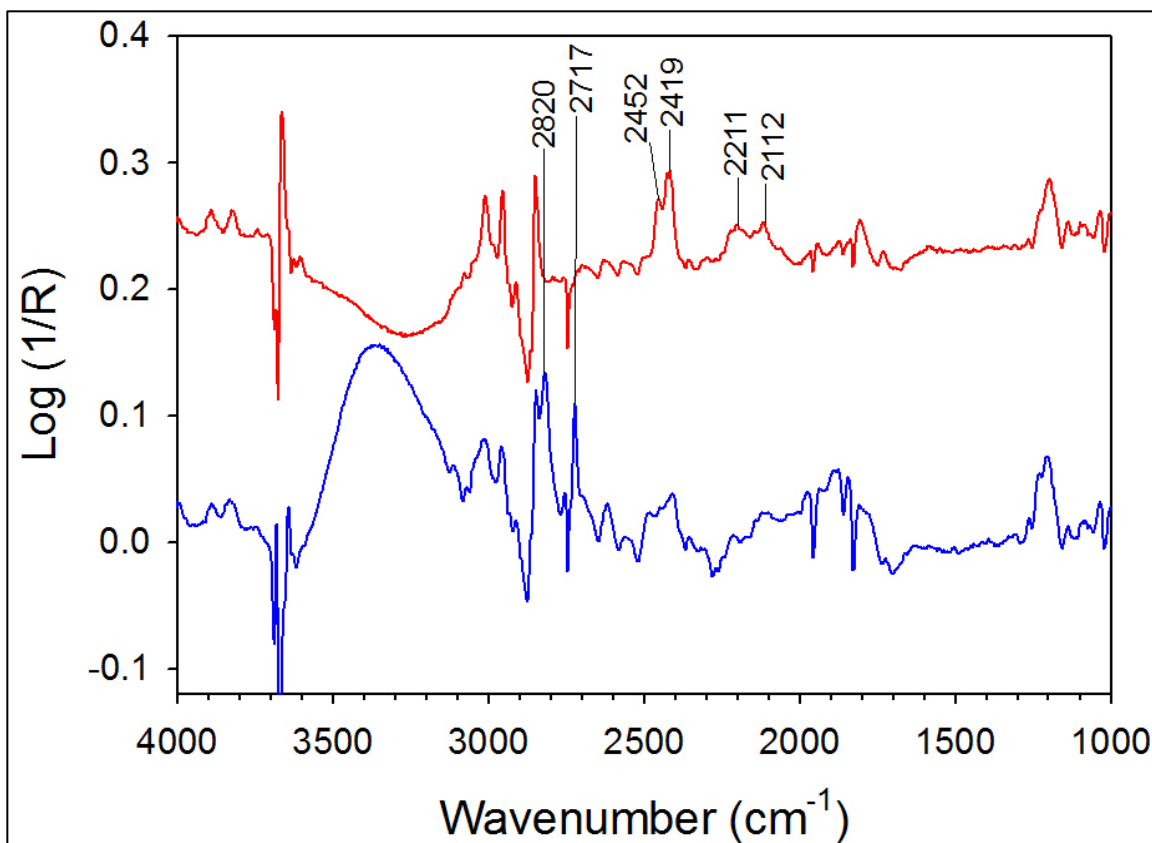
Figure 49. Spectra comparison of DMMP on UiO-66 before (red) and after overnight evacuation (blue).

The same procedure was used, as in the $Zr(OH)_4$ experiment, of dosing MeOH on

the UiO-66 as it is the expected decomposition product from this reaction. The spectral

comparison results did not confirm MeOH production, shown Figure 50, however, if the

UiO-66-DMMP spectra is compared to MeOH on the $Zr(OH)_4$, the 2820 cm^{-1} band aligns

exactly. The other band at 2717 cm^{-1} could not be correlated with MeOH adsorption. The

bands grow in together indicating they are from the same species, so MeOH is likely not

the product.

From the discussion above regarding the nature of pristine UiO-66, the material

used in the DRIFTS study was not expected to show any reactivity yet these definitive

bands not assigned to DMMP are present in the spectra. It is, however, unclear what

product is formed. The reaction and product may be dependent on the DMF solvent still

present in pores of the MOF and further studies are needed for confirmation of this as well as determination of the reaction product(s).
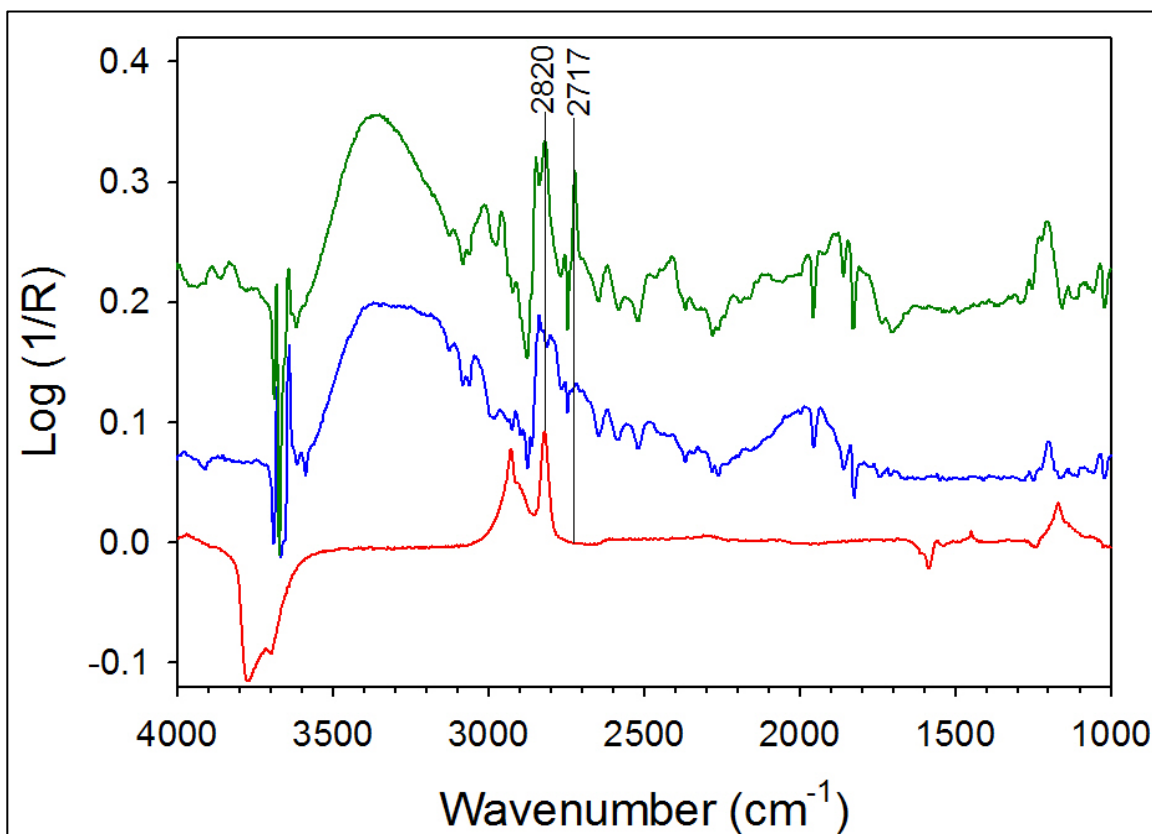
Figure 50. Spectra comparison of DMMP on UiO-66 (green), MeOH on UiO-66 (blue), and MeOH on Zr(OH)₄ (red).

In the work done at Kennesaw State University it is proposed that the UiO-66 sample has defect sites, thus, resulting in decomposition of the DMMP. The evidence that the bands of DMMP relative intensities of the v_a (P-CH$_3$) and v_a (P-O-CH$_3$) bands at 3011 and 2955 cm^{-1} appear 1:1, as expected for a MMP species rather than DMMP. There is the further evidence for reaction of the DMMP in the two distinct P-H bands seen in the spectra at 2451 and 2416 cm^{-1}, which could show either two distinct product formations or adsorption of the same product in distinct locations. As a side note, as with the Zr(OH)$_4$, there is evidence of carbon monoxide formation from the broad feature containing two bands from 2000- 2250 cm^{-1} with one distinct band at 2112 cm^{-1} and the

other less definite but ~2200 cm^{-1}, Figure 49, where the Zr(OH)$_4$ showed bands at 2078 and 2198 cm^{-1}.

UiO-66 shows evidence of enhanced reactivity as compared to the Zr(OH)$_4$ in the DRIFTS results. The unassigned bands reach a maximum point after exposure to ~60 μmol of DMMP as opposed to ~25 μmol, seen with the Zr(OH)$_4$. Since much of the structure of UiO-66 is the organic linker, this continual reactivity the MOF occurs with far fewer active sites than Zr(OH)$_4$, since the Zr(OH)$_4$ active sites can at each hydroxide location. Also, the production of the P-H bond is evident nearly immediately after the DMMP is introduced where it is seen emerging at much higher dosing on the Zr(OH)$_4$.

2. UiO-66-NH$_2$

DRIFTS results of introducing DMMP to the amine functionalized UiO-66 yielded an interesting result Figure 51. The band at 2793 cm^{-1}, presumed from decomposition as it does not correspond to a DMMP band, does not immediately emerge as was seen with the previous active materials, Zr(OH)$_4$ and UiO-66. The appearance of this additional band is still seen early, roughly 15 μmol into dosing, just not instantaneously. Another interesting difference is that this band does not diminish upon evacuation as the other materials have shown; rather the band reaches peak intensity after sitting under vacuum overnight, suggesting that the reaction on this MOF proceeds at a slower rate. The stability of the product must be due to the electron donating properties of the amine substitution, as this results is not seen with either the Zr(OH)$_4$ or UiO-66 . There is a single band corresponding to a P-H stretch at 2430 cm^{-1}. There is also a well-defined band at 1737 cm^{-1}, attributable by location to a C=O stretch, which grows in in

80

accordance with the 2793 cm^{-1} band. There is a similar feature also seen in UiO-66 though much less intense. It is proposed that the UiO-66-NH$_2$ material is not as riddled with defect sites, if at all, like the UiO-66 is, and operates using a different mechanism.
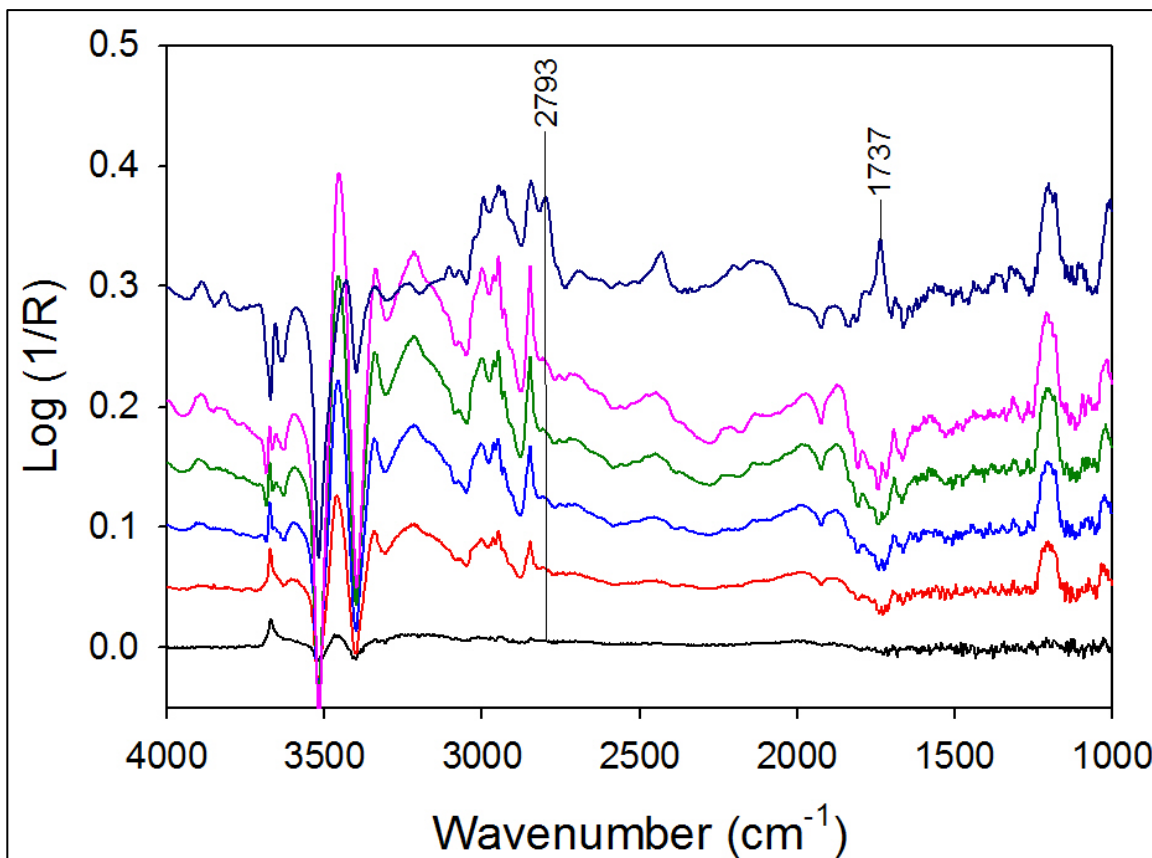
Figure 51. Spectra evolution of DMMP on UiO-66-NH$_2$ from 0-70 µmol (black –pink) and following evacuation (navy).

3. UiO-67

Exposure of DMMP to the UiO-67 MOF structure in the DRIFTS cell yielded spectra, Figure 52, which resembles that seen for the previously discussed silica sample. There are primarily four bands seen in the C-H stretching region at 2992, 2953, 2929, and 2848 cm^{-1} in the approximate proportions expected for molecular DMMP. There are two small bands at 2821 and 2722 cm^{-1}, discussed above with UiO-66, showing that there is a small amount of the same reaction proceeding. An interesting note is that when a MeOH

81

sample was used for comparison very weak intensity spectra were able to be obtained, this is presumably because the larger pores of UiO-67 allowed fast dispersion of the MeOH throughout and through the MOF to the vacuum before they could be analyzed. This MeOH diffusion result may be a small constituent in the difference seen between the UiO-66 and UiO-67, however, it is apparent that the majority of the DMMP in contact with the UiO-67 stays DMMP. After sitting overnight under vacuum the DMMP bands have decreased greatly and the additional products bands are completely absent. This indicates that the majority of the DMMP is solely physiosorbing on the MOF. There is the evidence of some reaction and the residual DMMP structure after overnight evacuation may be due to these products. There is no clear band able to be ascribed to a P-H bond, an expected result if there is no or little reaction.
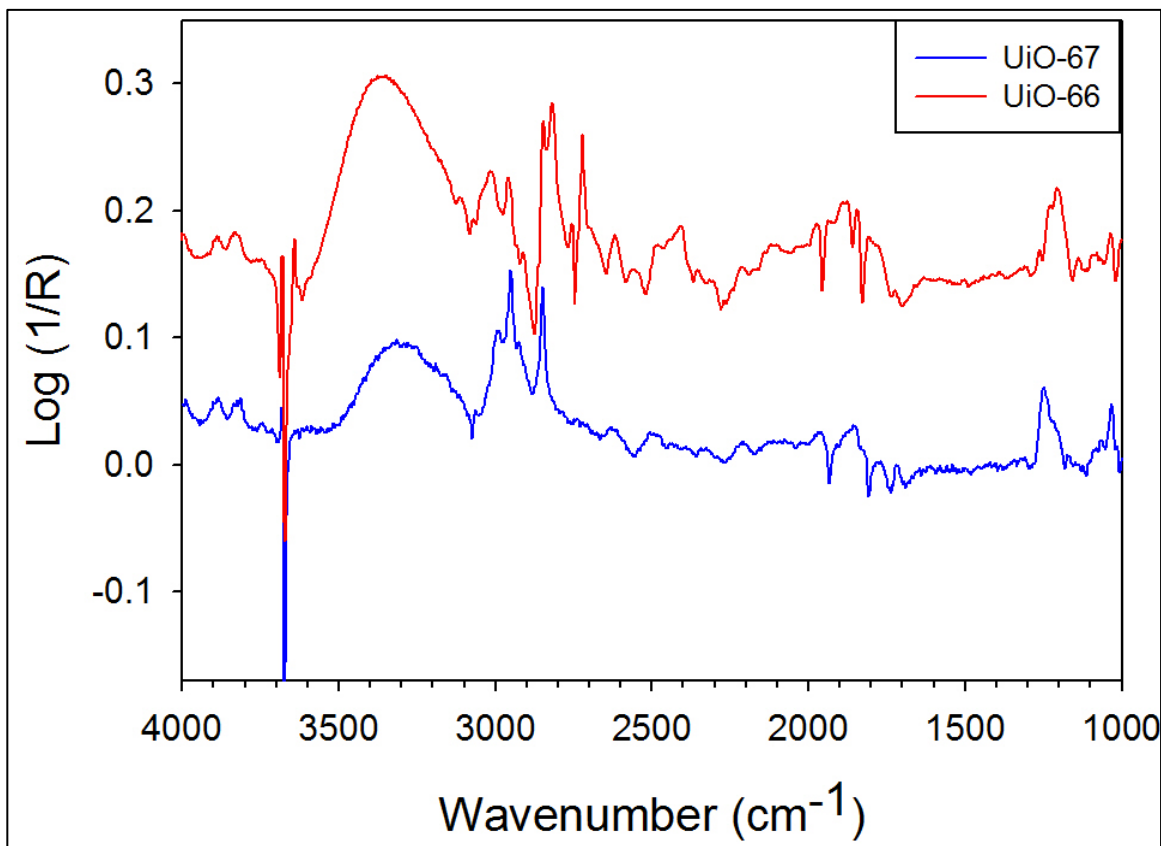
Figure 52. Spectra comparison of DMMP on UiO-66 vs. UiO-67.

D. Microreactor

 1. UiO-66

The results of flowing DMMP through UiO-66 that had not been thermally activated showed no reactivity. The only molecules seen to elute were molecular DMMP and DMF, which from the TGA data is known to be present in the pores of the MOF. The breakthrough amount for the UiO-66 sample is compare to the other MOFs, Table 8 and Figure 53. The results show that UiO-66 adsorbs more DMMP than all the other MOFs. Where noted, thermal activation of the MOF refers to heating the UiO-66 to 100 ^{o}C under flow of N_2 at 10 mL/min for two hours before cooling the sample still with flow, followed by flowing DMMP mixture. The results of the pretreatment from the spectra show appearance of a small amount of MeOH, which ends quickly, late into the experiment far after the DMMP is seen. This is a notable difference from the results in the DRIFTS experiment as decomposition product should appear and last much longer, than what was observed. It is expected that allowing the MOFs to sit under vacuum overnight acted as a better activation procedure than the thermal treatment and flow. Though thermally activating the UiO-66 seems slightly increase the reactivity, the DMMP uptake is reduced by ~35 %. This is likely due to the removal of some DMF and dehydration of the SBU.

 2. UiO-66-NH$_2$

The results of flowing DMMP through amine functionalized UiO-66 that had not been thermally treated was the same as what was seen for the standard UiO-66, only with reduced uptake of DMMP. The only molecules seen to elute from the system were

molecular DMMP and DMF, which again supports the conclusion from the TGA data that DMF remains within the pores of the MOFs after synthesis. With thermal treatment of the UiO-66-NH$_2$, as with the UiO-66, there is evidence of MeOH production far after the emergence of molecular DMMP. The yield of MeOH from both the UiO-66 and UiO-66-NH$_2$ are negligible in comparison to that of the Zr(OH)$_4$ substrate. Thermally activated UiO-66-NH$_2$ also exhibits a reduction in DMMP uptake by ~35 %, as was seen with the UiO-66.

3. UiO-67

The results of flowing DMMP through UiO-67 showed no sign of reaction as the only compounds observed in the infrared cell were molecular DMMP and H$_2$O, displaced from the SBU. There was little to no evidence of DMF emerging, which corresponds well to the previously discussed TGA results that very little DMF remains in the pores of the UiO-67. The experiment was performed without thermal activation for consistency with the DRIFTS experiment and a thermally treated sample could not be attempted as a limited amount of sample was supplied.

Table 8. Comparison of DMMP uptake on MOFs. *Cmarik et al.[107] §Cavka et al.[46]

Sample	Mass (mg)	Breakthrough Amount (μmol DMMP)	Surface Area (m²/g)	DMMP uptake (molecules/nm²)
UiO-66	11.6	18	1105*	.85
Thermally Activated UiO-66	9.1	9	1105*	.54
UiO-66-NH$_2$	14.5	15	1123*	.56
Thermally Activated UiO-66-NH$_2$	14.8	10	1123*	.36
UiO-67	12.0	4	3000§	.06

Figure 53. Comparison of uptake of DMMP per unit area of MOF.

E. DMMP uptake of MOFs compared to $Zr(OH)_4$

In comparison with the results from the MOFs, $Zr(OH)_4$ seems show the highest adsorptivity, shown Table 9 and Figure 54, showing over 3 times the adsorption capacity with the highest adsorbing MOF. This is likely due to the higher porosity of the MOFs allowing DMMP easier movement throughout the material due to having a lower number of metal oxide adsorption sites as well as a clear path created by the supramolecular structure.

Table 9. Comparison of DMMP uptake of Zr(OH)$_4$ and MOFs. *Cmarik *et al.*[107] §Cavka *et al.*[46]

Sample	Mass (mg)	Breakthrough Amount (µmol DMMP)	Surface Area (m²/g)	DMMP uptake (molecules/nm²)
Zr(OH)$_4$	11.9	26	462	2.85
UiO-66	11.6	18	1105*	.85
Thermally Activated UiO-66	9.1	9	1105*	.54
UiO-66-NH$_2$	14.5	15	1123*	.56
Thermally Activated UiO-66-NH$_2$	14.8	10	1123*	.36
UiO-67	12.0	4	3000§	.06

Figure 54. Comparison of uptake of DMMP per unit area of material.

CHAPTER V. CONCLUSION

Zirconium hydroxide was found to be an excellent reactive substrate for the adsorption and decomposition of the chemical warfare agent simulant DMMP at room temperature. The reaction appears to be non-selective towards the active OH site, occurring at either terminal or bridging OH sites (*t*-OH or *b*-OH). The reaction produces MeOH and MMP as decomposition products as well as a novel product from this decomposition, MMPH. The MMPH formation is not seen to occur until higher exposures of DMMP to the $Zr(OH)_4$ material, indicating that it is a concentration rather than time-dependent reaction. It is also apparent that the phosphorous-bound hydrogen comes from the surface of the material. The MeOH product is seen to form directly as gas phase MeOH as well as an intermediate surface-OMe species, which is readily displaced as gas phase MeOH by further adsorption of DMMP. The overall yield of decomposition of $Zr(OH)_4$ was at least 45 % higher than other materials previously studied.[15] Additionally $Zr(OH)_4$ was seen to immediately decompose DMMP producing gas phase MeOH, unlike previous materials where there has is typically an induction period before seeing products.[15]

Applying heat to either the pretreatment of the $Zr(OH)_4$ or after the $Zr(OH)_4$ sample has been completely saturated has notable effects. Pretreatment temperature to 300 ℃ reduces the reactivity of the material with DMMP nearly 40 % and the absorptivity of DMMP nearly 70 %. Post exposure heating of the sample

saturated with DMMP shows additional reaction yielding products: methanol, dimethyl ether, carbon monoxide, and MMP/DMMP. The carbon monoxide production is thought to be a reduction of methanol to carbon monoxide and hydrogen, and is noted in small amount even in the room temperature DRIFTS reaction. Even after heating the material to 400 °C the majority of the phosphorous atoms still remain on the surface, showing that the material is acting as a reactive adsorbent which experiences surface poisoning from exposure to DMMP.

The results in this study show that on the surface of UiO-66 and UiO-66-NH$_2$ in vacuum conditions there is apparent reaction with the DMMP. However, in the flow reactor system there is little to evidence of molecules eluting besides the synthesis solvent, DMF, and molecular DMMP. It is believed that the preparation in the vacuum system, allowing vacuum overnight acts as a better activation for these materials than heating the material with a flow of N$_2$, as used in the flow reactor. Pristine UiO-66 has been shown to be non-reactive with DMMP, and thus, we conclude that the UiO-66 used in the current study must have a degree of defects.[51] UiO-67 appears to have little to no reaction, showing that DMMP primarily physiosorbs to the material.

Zr(OH)$_4$ in comparison to the MOFs in this work and various other materials shows both superior reactivity as well as adsorptivity.[15] None of the materials in this work show characteristics of a true catalyst, rather in the case of reaction the phosphorous containing species is seen to poison the surface until no further adsorption or reaction is able to occur. The heating of the Zr(OH)$_4$ after exposure to

DMMP not sufficiently removing the phosphorous containing species even at 400 ^{o}C is clear evidence the material is not be reusable. This is especially true considering that reactivity of the material is reduced by nearly 40 % by heating to 300 ^{o}C prior to exposure. Despite the shortcoming of being non-catalytic heterogeneous gas-solid reaction, compiling this study with the liquid-solid reaction study performed by Bandosz *et al*. yields $Zr(OH)_4$ as arguably the most effective and versatile nerve agent reactant to date.

REFERENCES

1. Sun, Y.; Ong, K.Y. *Detection technologies for chemical warfare agents and toxic vapors*. CRC Press, 2004.

2. Ganesan, K.; Raza, S. K.; and Vijayaraghavan, R. Chemical Warfare Agents. *Journal of Pharmacy and Bioallied Sciences*. **2010,** *2(3),* 166–178.

3. Segall, Y.; Quistad, G. B.; Sparks, S. E.; Casida, J. A. Major intermediates in organophosphate synthesis (PCl3, POCl3, PSCl3, and their diethyl esters) are anticholinesterase agents directly or on activation. *Chemical Research in Toxicology.* **2003,** *16(3)*, 350-356.

4. Makhaeva, G. F.; Aksineko, A. Y.; Sokolov, V. B.; Serebryakova, O. G.; Racharson, R. J. Synthesis of organophosphates with fluorine-containing leaving groups as serine esterase inhibitors with potential for Alzheimer disease therapeutics. *Bioorganic and Medicinal Chemistry Letter.s* **2009,** *19(19),* 5528-5530.

5. Rigterink, R. H.; Kenaga, E. E. Synthesis and Insecticidal Activity of Some O, O-Dialkyl 0-3, 5, 6-Trihalo-2-pyridyl Phosphates and Phosphorothioates. *Journal of Agricultural and Food Chemistry.* **1966,** *14(3),* 304-306.

6. Reesor, J. B.; Perry, B. J.; Sherlock, E. The synthesis of highly radioactive isopropyl methylphosphonofluoridate (sarin) containing P32 as tracer element. *Canadian Journal of Chemistry.* **1960,** *38(9),*1416-1427.

7. Sidell, F. R.; Hurst, C. G. Long-term health effects of nerve agents and mustard. *Medical Aspects of Chemical and Biological Warfare.* **1917,** 41(2), 229.

8. Holmstedt, B. O. Pharmacology of organophosphorus cholinesterase inhibitors. *Pharmacological reviews.* **1959,** *11(3),* 567-688.

9. Grob, D.; Harvey, A. M. The effects and treatment of nerve gas poisoning. *The American Journal of Medicine.* **1953,** *14(1)*, 52-63.

10. Jonas, L. A.; Rehrmann, J. A. The kinetics of adsorption of organo-phosphorus vapors from air mixtures by activated carbons. *Carbon.* **1972,** *10(6),* 657-663.

11. Conforti, P. F.; Braunstein, M.; Dodd, J. A. Energetics and Dynamics of the Reactions of O(^{3}P) with Dimethyl Methylphosphonate and Sarin. *The Journal of Physical Chemistry A.* **2009,** *113(49),* 13752-13761.

12. Templeton, M. K.; Weinberg, W.H. Adsorption and decomposition of dimethyl methylphosphonate on an aluminum oxide surface. *Journal of the American Chemical Society.* **1985,** *107(1)*, 97-108.

13. Templeton, M. K.; Weinberg, W.H. Decomposition of phosphonate esters adsorbed on aluminum oxide. *Journal of the American Chemical Society.* **1985,** *107(4),* 774-779.

14. Mitchell, M. B.; Sheinker, V. N.; Mintz, E. A. Adsorption and decomposition of dimethyl methylphosphonate on metal oxides. *The Journal of Physical Chemistry B.* **1997,** *101(51),* 11192-11203.

15. Sheinker, V. N.; Mitchell, M. B. Quantitative study of the decomposition of dimethyl methylphosphonate (DMMP) on metal oxides at room temperature and above. *Chemistry of Materials.* **2002,** *14(3),* 1257-1268.

16. Li, Y. X.; Klabunde, K. J. Nano-scale metal oxide particles as chemical reagents. Destructive adsorption of a chemical agent simulant, dimethyl methylphosphonate, on heat-treated magnesium oxide. *Langmuir.* **1991,** *7(7),* 1388-1393.

17. Quenneville, J.; Taylor, R. S.; van Duin, A. C. T. Reactive molecular dynamics studies of DMMP adsorption and reactivity on amorphous silica surfaces. *The Journal of Physical Chemistry C.* **2010,** *114(44),* 18894-18902.

18. Kanan, S. M.; Tripp, C. P. An infrared study of adsorbed organophosphonates on silica: a prefiltering strategy for the detection of nerve agents on metal oxide sensors. *Langmuir*. **2001,** *17(7),* 2213-2218.

19. Obee, T. N.; Satyapal, S. Photocatalytic decomposition of DMMP on titania. *Journal of Photochemistry and Photobiology A.* **1998,** *118(1),* 45-51.

20. Panayotov, D. A.; Morris, J. R. Uptake of a chemical warfare agent simulant (DMMP) on TiO2: Reactive adsorption and active site poisoning. *Langmuir.* **2009,** *25(6),* 3652-3658.

21. Tesfai, T. M.; Sheinker, V. N.; Mitchell, M. B. Decomposition of dimethyl methylphosphonate (DMMP) on alumina-supported iron oxide. *The Journal of Physical Chemistry B.* **1998,** *102(38),* 7299-7302.

22. Mitchell, M. B.; Sheinker, V. N.; Tesfamichael, A. B.; Gatimu, E. N.; Nunley, M. Decomposition of dimethyl methylphosphonate (DMMP) on supported cerium and iron co-impregnated oxides at room temperature. *The Journal of Physical Chemistry B*. **2003,** *107(2),* 580-586.

23. Mitchell, M. B.; Sheinker, V. N.; Cox, W. W.; Gatimu, E. N.; Tesfamichael, A. B. The room temperature decomposition mechanism of dimethyl methylphosphonate (DMMP) on alumina-supported cerium oxide-Participation of nano-sized cerium oxide domains. *The Journal of Physical Chemistry B*. **2004,** *108(5),* 1634-1645.

24. Mitchell, M. B.; Sheinker, V. N.; Cox, W. W. Room temperature reaction of ozone and dimethyl methylphosphonate (DMMP) on alumina-supported iron oxide. *The Journal of Physical Chemistry C*. **2007,** *111(26),* 9417-9426.

25. Mitchell, M. B.; Sheinker, V. N.; Cox, W. W.; Hardcastle, K. Sustained Room Temperature Decomposition of Dimethyl Methylphosphonate (DMMP) by O_3 on Alumina-Supported MnO_x. *The Journal of Physical Chemistry C*. **2011,** *115(23),* 11514-11524.

26. Bandosz, T. J.; Laskoski, M.; Mahie, J.; Mogilevsky, G.; Peterson, G. W.; Rossin, J. A.; Wagner, G. W. Reactions of VX, GD, and HD with Zr $(OH)_4$: Near instantaneous decontamination of VX. *The Journal of Physical Chemistry C*. **2012,** *116(21),* 11606-11614.

27. Peterson, G. W.; Karwacki, C. J.; Feaver, W. B.; Rossin, J. A. Zirconium hydroxide as a reactive substrate for the removal of sulfur dioxide. *Industrial and Engineering Chemistry Research*. **2009,** *48(4)*, 1694-1698.

28. Peterson, G. W.; Karwacki, C.J.; Surface chemistry and morphology of zirconia polymorphs and the influence on sulfur dioxide removal. *The Journal of Physical Chemistry C*. **2011,** *115(19),* 9644-9650.

29. Peterson, G. W.; Wagner, G. W.; Keller, J. H. Rossin, J. A. Enhanced cyanogen chloride removal by the reactive zirconium hydroxide substrate. *Industrial and Engineering Chemistry Research*. **2010,** *49(22)*, 11182-11187.

30. Peterson, G. W.; Rossin, J. A. Removal of chlorine gases from streams of air using reactive zirconium hydroxide based filtration media. *Industrial and Engineering Chemistry Research*. **2012,** *51(6),* 2675-2681.

31. Southon, P. D.; Barlett, J. R.; Woolfrey, J. L.; Ben-Nissan, B. Formation and characterization of an aqueous zirconium hydroxide colloid. *Chemistry of Materials*. **2002,** *14(10)*, 4313-4319.

32. Guo, G. Y.; Chen, Y. L.; Ying, W. J. Thermal, spectroscopic and X-ray diffractional analyses of zirconium hydroxides precipitated at low pH values. *Materials Chemistry and Physics*. **2004,** *84(2),* 308-314.

33. Davies, L. E.; Bonini, N. A.; Locatelli, S.; Gonzo, E. E. Characterization and catalytic activity of zirconium dioxide prepared by sol-gel. *Latin American Applied Research*. **2005,** *35(1),* 23-28.

34. Chitrakar, R.; TEzuka, S.; Sonoda, A.; Sakane, K.; Ooi, K.; Hirotsu, T. Selective adsorption of phosphate from seawater and wastewater by amorphous zirconium hydroxide. *Journal of Colloid and Interface Science*. **2006,** *297(2),* 426-433.

35. DeCoste, J. B.; Peterson, G. W. Metal-Organic Frameworks for Air Purification of Toxic Chemicals. *Chemical Reviews*. **2014,** *114(11),* 5695-5727.

36. Han, S. S.; Mendoza-Cortés, J. L.; Goddard, W. A. Recent advances on simulation and theory of hydrogen storage in metal–organic frameworks and covalent organic frameworks. *Chemical Society Reviews*. **2009,** *38(5),* 1460-1476.

37. Suh, M. P.; Park, H. J.; Prasad, T. K.; Lim, D. W. Hydrogen storage in metal–organic frameworks. *Chemical Reviews*. **2011,** *112(2),* 782-835.

38. Millward, A. R.; Yaghi, O. M. Metal-organic frameworks with exceptionally high capacity for storage of carbon dioxide at room temperature. *Journal of the American Chemical Society*. **2005,** *127(51),* 17998-17999.

39. Getman, R. B.; Bae, Y. S.; Willmer, C. E.; Snurr, R. Q. Review and analysis of molecular simulations of methane, hydrogen, and acetylene storage in metal–organic frameworks. *Chemical Reviews*. **2011,** *112(2)*, 703-723.

40. Lee, J. Y.; Omar, K. F.; Roberts, J.; Scheidt, K. A.; Nquyen, S. T.; Hupp, J. T. Metal–organic framework materials as catalysts. *Chemical Society Reviews*. **2009,** *38(5),* 1450-1459.

41. Wu, C. D.; Hu, A.; Zhang, L.; Lin, W. A homochiral porous metal-organic framework for highly enantioselective heterogeneous asymmetric catalysis. *Journal of the American Chemical Society*. **2005,** *127(25),* 8940-8941.

42. Alaerts, L.; Seguin, E.; Poelman, H.; Thibault-Starzyk, F.; Jacobs, P. A.; De Vos, D. E.; Probing the Lewis Acidity and Catalytic Activity of the Metal–Organic Framework [Cu3 (btc) 2](BTC= Benzene-1, 3, 5-tricarboxylate). *Chemistry–A European Journal*. **2006,** *12(28),* 7353-7363.

43. Li, J. R.; Sculley,J.; Zhou, H. C. Metal–organic frameworks for separations. *Chemical Reviews*. **2011,** *112(2),* 869-932.

44. Kreno, L. E.; Leong, K.; Farha, O. K.; Allendorf, M.; Van Duyne, R. P.; Hupp, J. T. Metal–organic framework materials as chemical sensors. *Chemical Reviews.* **2011,** *112(2),* 1105-1125.

45. Kickelbick, G.; Schubert, U. Oxozirconium Methacrylate Clusters: Zr6 (OH) 4O4 (OMc) 12 and Zr4O2 (OMc) 12 (OMc= Methacrylate). *Chemische Berichte.* **1997,** *130(4).* 473-478.

46. Cavka, J. H.; Jakobsen, S.; Olsbye, U.; Guillou, N.; Lamberti, C.; Bordiga, S.; Lillerud, K. P. A new zirconium inorganic building brick forming metal organic frameworks with exceptional stability. *Journal of the American Chemical Society.* **2008,** *130(42),* 13850-13851.

47. Wu, H.; Yildirim, T.; Zhou, W. Exceptional mechanical stability of highly porous zirconium metal–organic framework UiO-66 and its important implications. *The Journal of Physical Chemistry Letters.* **2013,** *4(6),* 925-930.

48. Planas, N.; Mondloch, J. E.; Tussupbayev, S.; Borycz, J.; Gagliardi, L.; Hupp, J. T.; Farha, O. K.; Cramer, C. J. Defining the proton topology of the Zr6-based metal–organic framework NU-1000. *The Journal of Physical Chemistry Letters*. **2014,** *5(21),* 3716-3723.

49. Moon, S. Y.; Liu, Y.; Hupp, J. T.; Farha, O. K. Instantaneous Hydrolysis of Nerve-Agent Simulants with a Six-Connected Zirconium-Based Metal–Organic Framework. *Angewandte Chemie International Edition.* **2015,** *54(23),* 6795-6799.

50. Kandiah, M.; Nilsen, M. H.; Ussegilo, S.; Jakobsen, S.; Olsbye, U.; Tilset, M.; Larabi, C.; Quadrelli, E. A.; Bonino, F.; Lillerud, K. P. Synthesis and stability of tagged UiO-66 Zr-MOFs. *Chemistry of Materials.* **2010,** *22(24),* 6632-6640.

51. Wang, G.; Sharp, C.; Plonka, A. M.; Frankel, A. I.; Guo, W.; Hill, C.; Smith, C.; Kollar, J.; Troya, D.; Morris, J. R. Mechanism and Kinetics for Reaction of the Chemical Warfare Agents Simulant, DMMP(g), with Zirconium(IV) MOFs: An Ultrahigh-Vacuum and DFT Study. *The Journal of Physical Chemistry C.* **2017,**

52. Vandichel, M.; Hajek, J.; Vermoortele, F.; Waroquier, M.; De Vos, D.; Van. Speybroek, V. Active site engineering in UiO-66 type metal–organic frameworks by intentional creation of defects: a theoretical rationalization. *CrystEngComm.* **2015,** *17(2),* 395-406.

53. Wu, H.; Chua, Y. S.; Krunglevclute, V.; Tyagi, M.; Chen, P.; Yildrim, T.; Zhuo, W. Unusual and highly tunable missing-linker defects in zirconium metal–organic framework UiO-66 and their important effects on gas adsorption. *Journal of the American Chemical Society.* **2013,** *135(28)*, 10525-10532.

54. Vermoortele, F.; Bueken, B.; Bars, G. L., Van de Voorde, B.; Vandichel, M.; Houthoofd, K.; Vimont, A.; Daturi, M.; Waroquier, M.; Van Speybroeck, V.; Kirschhock, C.; De Vos, D. Synthesis modulation as a tool to increase the catalytic activity of metal–organic frameworks: The unique case of UiO-66 (Zr). *Journal of the American Chemical Society*. **2013,** *135(31)*, 11465-11468.

55. Liang, W.; Chevreau, H.; Ragon, F.; Southon, P. D.; Peterson, V. K.; D'Alessandro, D. M. Tuning pore size in a zirconium–tricarboxylate metal–organic framework. *CrystEngComm*. **2014,** *16(29),* 6530-6533.

56. Plessers, E.; Fu, G.; Tan, C. Y. X.; De Vos, D. E.; Roeffaers, M. B. Zr-Based MOF-808 as Meerwein–Ponndorf–Verley Reduction Catalyst for Challenging Carbonyl Compounds. *Catalysts.* **2016,** *6(7),* 104.

57. Wendlandt, W.; Hecht, H. *Reflectance Spectroscopy.* New York: Interscience Publishers, 1966. Print.

58. Sirita, J.; Phanichphant, S.; Meunier. F. C. Quantitative analysis of adsorbate concentrations by diffuse reflectance FT-IR. *Analytical Chemistry*. **2007,** *79(10)*, 3912-3918.

59. Olinger, J. M.; Griffiths, P. R. Quantitative effects of an absorbing matrix on near-infrared diffuse reflectance spectra. *Analytical Chemistry.* **1988,** *60(21),* 2427-2435.

60. Štefanić, G.; Popović, S.; Musić, S. The effect of mechanical treatment of zirconium (IV) hydroxide on its thermal behaviour. *Thermochimica Acta.* **1995,** *259(2),* 225-234.

61. Sato, T.; Ozawa, F.; Nakamura, T.; Watanabe, H.; Ikoma, S. Thermal decomposition of zirconium hydroxide. *Thermochimica Acta.* **1979,** *34(2)*, 211-220.

62. Štefanić, G.; Musić, S.; Sekulić, A. Influence of precipitation chemistry and ball-milling on the thermal behavior of zirconium hydroxide. *Thermochimica Acta.* **1996,** *273,* 119-133.

63. Huang, C.; Tang, Z.; Zhang, Z. Differences between zirconium hydroxide (Zr (OH) 4· nH2O) and hydrous zirconia (ZrO2· nH2O). *Journal of the American Ceramic Society.* **2001,** *84(7),* 1637-1638.

64. Selim, S. A.; El-Akkad, T. M. Thermal decomposition, pore structure and heats of immersion of zirconia gel. *Journal of Chemical Technology and Biotechnology*. **1977,** *27(1),* 58-66.

65. Hornebecq, V.; Knofel, C.; Boulet, P.; Kuchta, B.; Llewellyn, P. L. Adsorption of carbon dioxide on mesoporous zirconia: microcalorimetric measurements, adsorption isotherm modeling, and density functional theory calculations. *The Journal of Physical Chemistry C*. **2011,** *115(20),* 10097-10103.

66. Sing, K. S. W. Reporting physisorption data for gas/solid systems with special reference to the determination of surface area and porosity. *Pure and Applied Chemistry*. **1985,** *57(4),* 603-619.

67. Roustila, A.; Chêne, J.; Séverac, C. XPS study of hydrogen and oxygen interactions on the surface of zirconium. *Journal of Alloys and Compounds*. **2003,** *356,* 330-335.

68. Brenier, R.; Mugnier, J.; Mirica, E. XPS study of amorphous zirconium oxide films prepared by sol–gel. *Applied Surface Science*. **1999,** *143(1),* 85-91.

69. Wong, P. C., Li, Y. S.; Zhou, M. Y.; Mitchell, K. A. R. XPS investigations of the interactions of hydrogen with thin films of zirconium oxide I. Hydrogen treatments on a 10 Å thick film. *Applied Surface Science*. **1995,** *89(3),* 255-261.

70. Ding, J.; Guo, D.; Deng, C.; Zhu, H.; Yu, C. Low-temperature synthesis of nanocrystalline ZrC coatings on flake graphite by molten salts. *Applied Surface Science*. **2017,** *407,* 315-321.

71. Rusu, C. N.; Yates, J. T. Photooxidation of dimethyl methylphosphonate on TiO2 powder. *The Journal of Physical Chemistry B*. **2000,** *104(51),* 12299-12305.

72. Moss, J. A.; Szczenpankiewicz, S. H.; Park, E.; Hoffman, M. R. Adsorption and photodegradation of dimethyl methylphosphonate vapor at TiO2 surfaces. *The Journal of Physical Chemistry B*. **2005,** *109.42,* 19779-19785.

73. Panayotov, D. A.; Morris, J. R. Uptake of a chemical warfare agent simulant (DMMP) on TiO2: Reactive adsorption and active site poisoning. *Langmuir*. **2009,** *25(6)*, 3652-3658.

74. Kiselev, A.; Mattson, A.; Andersson, M.; Palmqvist, A. E. C.; Osterlund, L. Adsorption and photocatalytic degradation of diisopropyl fluorophosphate and dimethyl methylphosphonate over dry and wet rutile TiO 2. *Journal of Photochemistry and Photobiology A: Chemistry*. **2006,** *184(1),* 125-134.

75. Panayotov, D. A.; Morris, J. R. Thermal decomposition of a chemical warfare agent simulant (DMMP) on TiO2: Adsorbate reactions with lattice oxygen as studied by infrared spectroscopy. *The Journal of Physical Chemistry C*. **2009,** *113(35),* 15684-15691.

76. Barlow, D.; Balow, R.; Lundon, J.; Wynne, J. H.; Ng, A.; Stoud, R.; Bermudez, V. M.; Gordon, W.; Iordanov, I.; Knox, C.; Karwacki, C. J.; Wagner, G. W.; Peterson, G. W.; Pehrsson, P. Structure of Zirconium(IV) Hydroxide Materials for Chemical Warfare Agent Decomposition. Proceedings of the 251st ACS National Meeting & Exposition, Sand Diego, CA, United States, March 13-17, 2016.

77. Ouyang, F.; Kondo, J. N.; Maruya, K.; Domen, K. Site Conversion of Methoxy Species on ZrO_2. *The Journal of Physical Chemistry B*. **1997,** *101(25),* 4867-4869.

78. Ouyang, F.; Nakayama, A.; Tabada, K.; Suzuki, E. Infrared Study of a Novel Acid− Base Site on ZrO2 by Adsorbed Probe Molecules. I. Pyridine, Carbon Dioxide, and Formic Acid Adsorption. *The Journal of Physical Chemistry B*. **2000,** *104(9),* 2012-2018.

79. Yamaguchi, T.; Nakano, Y.; Tanabe, K. Infrared study of surface hydroxyl groups on zirconium oxide. *Bulletin of the Chemical Society of Japan*. **1978,** *51(9),* 2482-2487.

80. Bett, J. A. S.; Christner, G.; Hall, K. Studies of the Hydrogen Held by Solids. XII. Hydroxyapatite Catalysts. *Journal of the American Chemical Society*. **1967**, *89(22),* 5535-5541.

81. Turner, A. M.; Abplanalp, M. J.; Chen, S. Y.; Chen, Y. T.; Chang, A. H. H.; Kaiser, R. I. A Photoionization Mass Spectroscopic Study on the Formation of Phosphanes in Low Temperature Phosphine Ices. *Physical Chemistry Chemical Physics*. **2015**, *17,* 27281-27291.

82. Dayanand, C.; Bhikshamaiah, G.; Jaya Tyagaraju, V.; Salagram, M. Review Structural Investigations of Phosphate Glasses: A Detailed Infrared Study of the x(PbO)-(1ix) P_2O_5 Vitreous System. *Journl of Materials Science*. **1996,** *31,* 1945-1967.

83. Carter III, R. O.; Gierczak, C. A.; Dickie, R. A. The Chemical Interaction of Organic Materials with Metal Substrates. Part II: FT-IR Studies of Organic Phosphate Films on Steel. *Applied Spectroscopy.***1986,** *40(5),* 649-655.

84. Cao, L.; Segal, S. R.; Suib, S. L.; Tang, X. Satyapal, S. Thermocatalytic oxidation of dimethyl methylphosphonate on supported metal oxides. *Journal of Catalysis*. **2000,** *194(1),* 61-70.

85. Ma, Z. Y.; Yang, C.; Wei, W.; Li, W. H.; Sun, Y. H. Surface properties and CO adsorption on zirconia polymorphs. *Journal of Molecular Catalysis A: Chemical*. **2005,** *227(1),* 119-124.

86. Korhonen, S.T.; Calatayud, M.; Krause, A. O. I. Structure and Stability of Formates and Carbonates on Monoclinic Zirconia: A Combined Study by Density Functional Theory and Infrared Spectroscopy. *The Journal of Physical Chemistry C.* **2008,** *112,* 16096-16102.

87. Li, C.; Sakata, Y.; Arai, T.; Domen, K.; Maruya, K.; Onishi, T. Carbon monoxide and carbon dioxide adsorption on cerium oxide studied by Fourier-transform infrared spectroscopy. Part 1.-Formation of carbonate species on dehydroxylated CeO_2, at room temperature. *Journal of the Chemical Society, Faraday Transactions 1: Physical Chemistry in Condensed Phases.* **1989,** *85(4),* 929-943.

88. Croy, J. R.; Mostafa, S.; Liu, J.; Sohn, Y.; Heinrich, H.; Cuenya, B. R. Support dependence of MeOH decomposition over size-selected Pt nanoparticles. *Catalysis Letters.* **2007,** *119(3),* 209-216.

89. Matsumura, Y.; Okumura, M.; Usami, Y.; Kagawa, K.; Yamashita, H.; Anpo, M.; Haruta, M. Low-temperature decomposition of methanol to carbon monoxide and hydrogen with low activation energy over Pd/ZrO_2 catalyst. *Catalysis Letters.* **1997,** *44(3),*189-191.

90. Ruiz-Rosas, R.; Bedia, J.; Rosas, J. M.; Lallave, M.; Loscertales, I. G.; Rodriguez-Mirasol, J. Methanol decomposition on electrospun zirconia nanofibers. *Catalysis Today.* **2012,** *187(1),* 77-87.

91. Katz, M. J.; Brown, Z. J.; Colon, Y. J.; Siu, P. W.; Scheidt, K. A.; Snurr, R. Q.; Hupp, J. T.; Farha, O. K. A Facile Synthesis of UiO-66, UiO-67, and their derivatives. *Chemical Communications.* **2013,** *49(82),* 9449-9451.

92. Valenzo, L.; Civalleri, B.; Chavan, S.; Bordiga, S.; Nilsen, M. H.; Jakobsen, S.; Lillerud, K. P.; Lamberti, C. Disclosing the complex structure of UiO-66 metal organic framework: a synergic combination of experiment and theory. *Chemistry of Materials.* **2011,** *23(7),* 1700-1718.

93. Wiersum, A. D.; Soubeyrand-Lenoir, E.; yang, Q.; Moulin, B.; Guillerm, V.; Yahia, M. B.; Bourrelly, S.; Vimont, A.; Miller, S.; Vagner, C.; Daturi, M.; Clet, G.; Serre, C.; Maurin, G.; Llewellyn, P. L. An Evaluation of UiO-66 for Gas-Bassed Applications. *Chemistry-An Asian Journal.* **2011,** *6(12),* 3270-3280.

94. Shearer, G. C.; Chavan, S. M.; Ethiraj, J.; Lillerud, K. P. Tuned to perfection: ironing out the defects in metal-organic framework UiO-66. *Chemistry of Materials.* **2014,** *26(14),* 4068-4071.

95. Bensitel, M.; Moravek, V.; Lamotte, J.;Saur, O.; Lavalley, J. C. Infrared Study of Alcohols adsorption on zirconium oxide: reactivity of alkoxy species towards CO_2. *Spectrochimica Acta Part A.* **1987,** *43(12)*, 1487-1491.

96. Sharma, A.; Kaur, S; Mahajan, C. G.; Tripathi, S. K.; Saini, G. S. S. Fourier Transform Infrared Spectral Study of N,N'-dimethylformamide-water-rhodamine 6G mixture. *Molecular Physics*. **2007,** *105(1),* 117-123.

97. Yamamoto, H.; Yano, H.; Kouchi, H.; Obora, Y.; Arakawa, R.; Kawasaki, H. N,N'-dimethylformamide-stabilized gold nanoclusters as a catalyst for the reduction of 4-nitrophenol. *Nanoscale*. **2012,** *4(14),* 4148-4154.

98. Tellez, C. A.; Hollauer, E.; Mondragon, M. A.; Castano, V. M. Fourier transform Infrared and Raman spectra, Vibrational Assignment and Ab Initio Calculations of Terephthalic Acid and Related Compounds. *Spectrochimica Acta Part A*. **2001,** *57(5)*, 993-1007.

99. Lee, M. W.; Kim, M. S.; Kim, K. Infrared and Raman Spectroscopic Study of Terephthalic Acid Adsorbed on Silver Surfaces. *Journal of Molecular Structure*. **1997,** *415(1-2),* 93-100.

100. Zerbi, G.; Sandroni, S. Fundamental Frequencies and Molecular Configuration of Biphenyl-II Normal Coordinated. *Spectrochimica Acta Part A*. **1968,** *24(5)*, 511-528.

101. Kaliszewski, M. S.; Heuer, A. H. Alcohol Interaction with Zirconia Powders. *Journal of the American Ceramic Society*. **1990,** *73(6),* 1504-1509.

102. Bensitel, M.; Saur, O.; Lavalley, J. C.; Mabilon, G. Acidity OF Zirconium-Oxide and Sulfated ZrO_2 Samples. *Material Chemistry and Physics*. **1987,** *17(3),* 249-258.

103. Hertl,W. Surface-Chemistry of Zirconia Polymorphs. *Langmuir*.**1989,** *5*, 96-100.

104. Dang, Z.; Anderson, B. G.; Amenomiya, Y.; Morrow, B. A., Silica-Supported Zirconia 1. Characteization by Infrared-Spectroscopy, Temperature-Programmed Desorption, and X-Ray-Diffraction. J. Phys. Chem. **1995**, *99(39),* 14437-14443.

105. Troya, D. Reaction Mechanism of Nerve-Agent Decomposition with Zr-Based Metal Organic Frameworks. *The Journal of Physical Chemistry C*. **2016,** *120(51),* 29312-29323.

106. Shearer, G. C.; Chavan, S.; Bordiga, S.; Svelle, S.; Olsbye, U.; Lillerud, K. P. Defect Engineering: Tuning the Porosity and Composition of the Metal–Organic Framework UiO-66 via Modulated Synthesis. *Chemistry of Materials*. **2016,** *28(11),* 3749-3761.

107. Cmarik, G. E.; Kim, M.; Cohen, S. M.; Walton, K. S. Tuning the Adsorption Properties of UiO-66 via Ligand Functionalization. *Langmuir,* **2012,** *28(44),* 15606-15613.

APPENDIX A. DRIFTS STANDARD OPERATING PROCEDURE

Starting Vacuum Pumps

1. Make sure bellows valve from DRIFTS cell to vacuum pumps is closed.
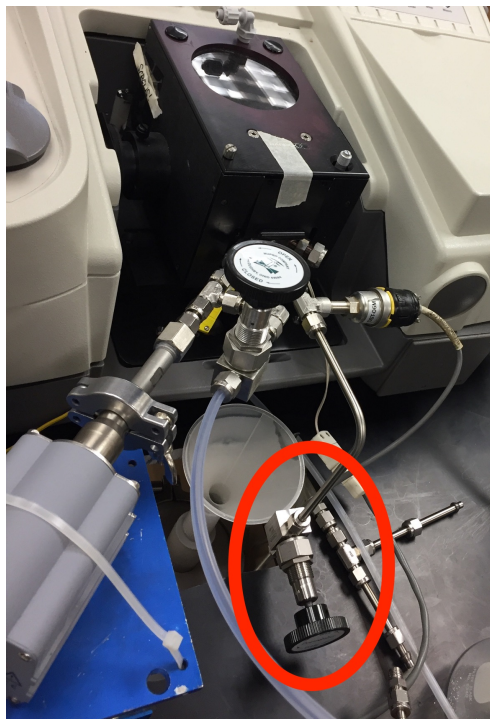
2. Check oil in mechanical pump.
3. Fill aerosol trap with liquid nitrogen (LN_2)

Aerosol Trap
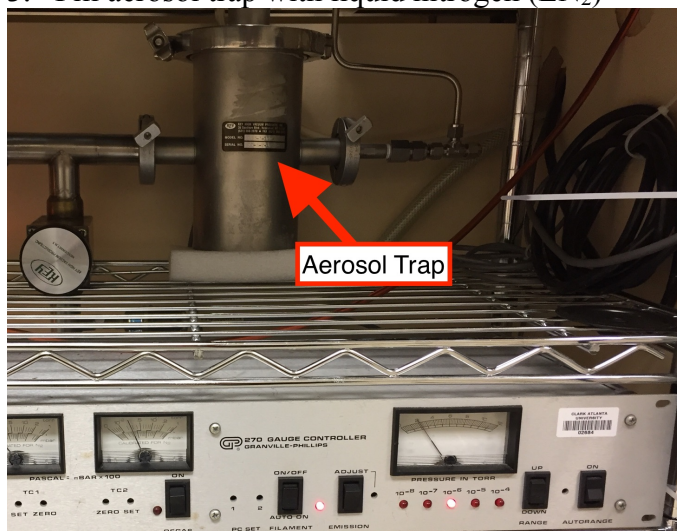
4. Ensure pneumatic valves "HIGH" and "LOW" are both down (closed).

5. Start mechanical pump with ON/OFF switch.

6. Allow system to pump down to below .5 Pascal in TC1 and TC2 windows.

7. Open divergent valve.
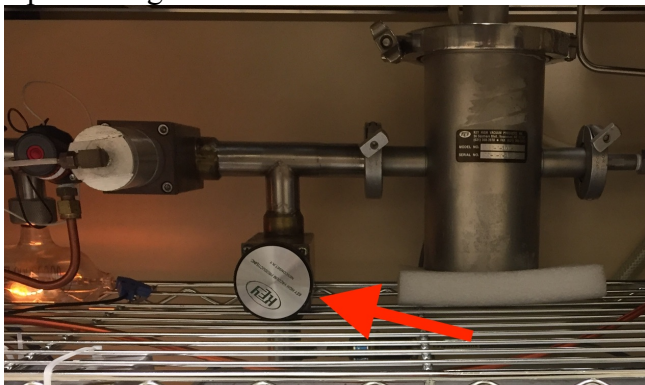
8. Again allow system to reduce pressure below .5 Pa for TC1 and TC2.
9. Close divergent valve.
10. Switch "LOW" pneumatic valve switch to the up (open) position and allow pressure to reduce back to below .5 Pa.

11. Turn Ion gauge filament on.

12. Start Turbotronik turbo-molecular vacuum pump and allow to fully activate, denoted by green LED indicating "NORMAL".
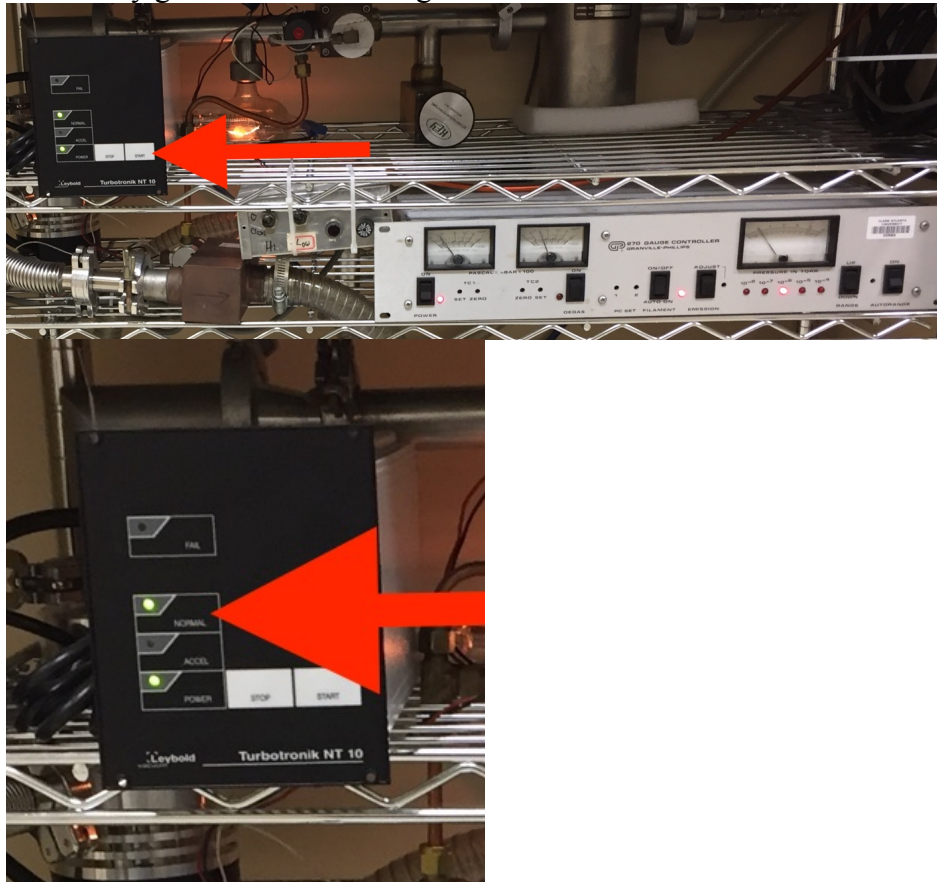
13. Switch "HIGH" pneumatic valve switch to the up (open) position and allow pressure to reduce back to below .5 Pa.
14. Ion gauge filament should remain on and ion gauge pressure should be reducing.
    a. If it does not, work backward from step 12→8, and allow mechanical pump more time to work then try again, 8→13.

Preparing a new sample

1. Wear gloves.
2. Close bellows valve from DRIFTS cell to vacuum pumps.
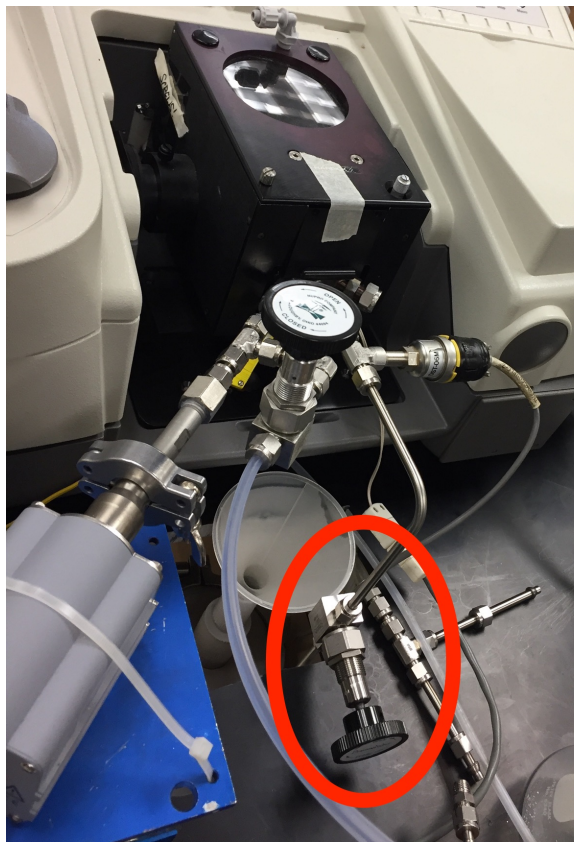
3. Using 3/32 (yellow) hex bit driver loosen and remove (4) bolts for tightening (2) brackets around stainless steel dome on sample stage.
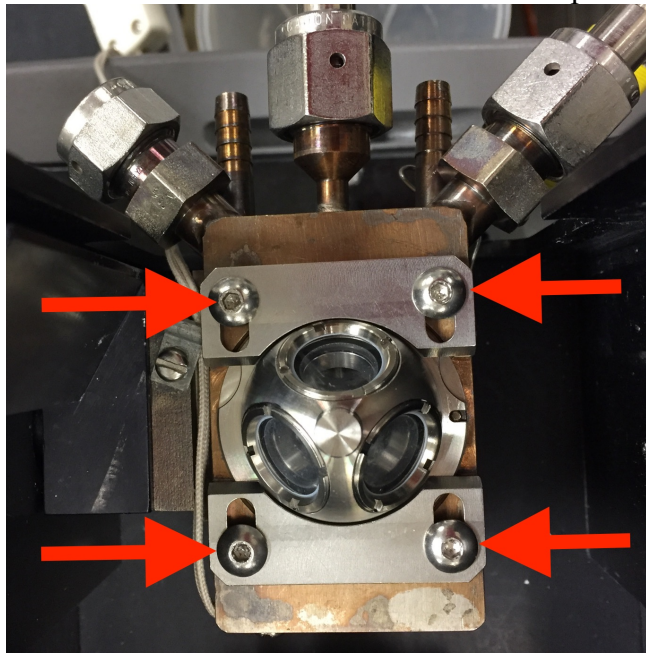
4. If previous sample is under vacuum, return atmospheric pressure using vacuum manifold, **Making a Gas Mixture** section.
5. Remove stainless steel dome and place on Kimwipe. **BE SURE TO NOTE WHICH WINDOW GOES TO WHICH SLOT AS TWO OF WINDOWS ARE SALT AND THE OTHER IS QUARTZ.**

a. Remove windows from dome using "tool", shown below.

b. Inspect all O-ring for any damage.
    i. If damaged, replace.
    ii. If OK, clean gently with H_2O.
    iii. Place on separate Kimwipe as not to lose.

6. Using bench top vacuum, gently remove sample from sample cup.
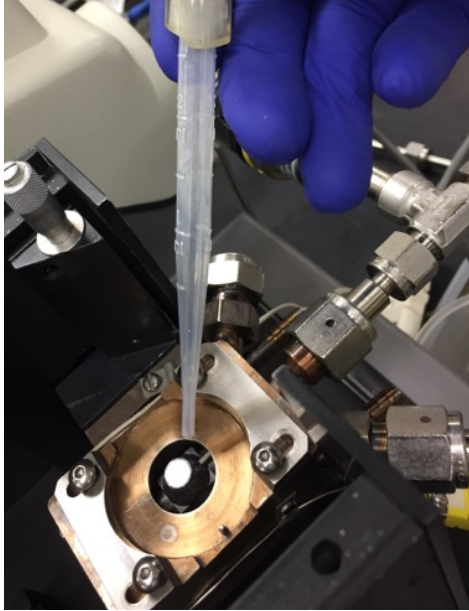
7. Remove entire stage by:
   a. Loosen and remove nuts from stage using 11/16 wrench.
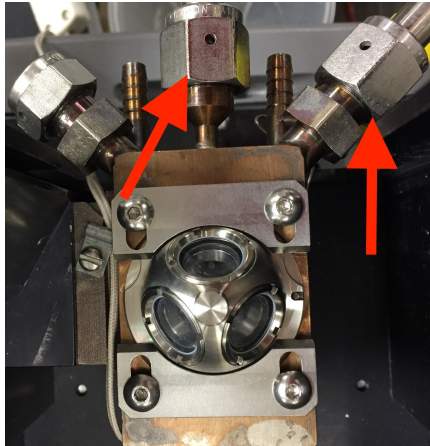
   b. Loosen and remove retention screw on the far side of the stage, located outside of DRIFTS box.
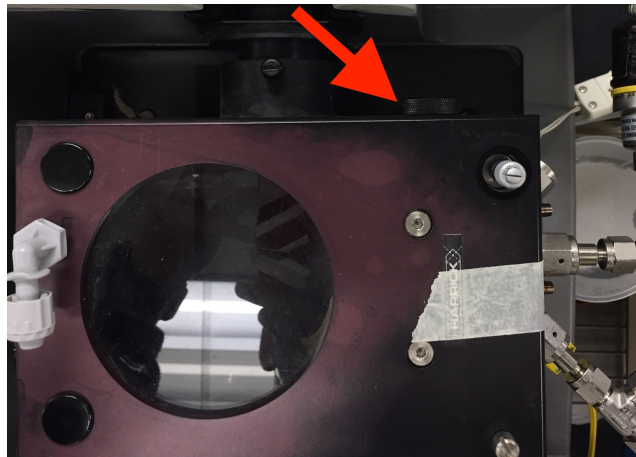
8. Disassemble sample stage using 3/32 hex bit driver careful not to lose any O-rings.
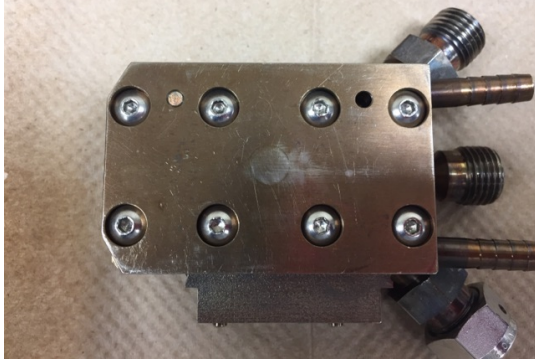
9. Remove all O-rings from stage, 3 large from the bottom of the stage and 2 small from the front of the stage, and inspect for any damage and set them to the side.
    a. If damaged, replace.
    b. If OK, clean gently with H_2O.

10. Remove screen from sample cup.
11. Remove thermocouple and heating cartridge from the backside of the stage.
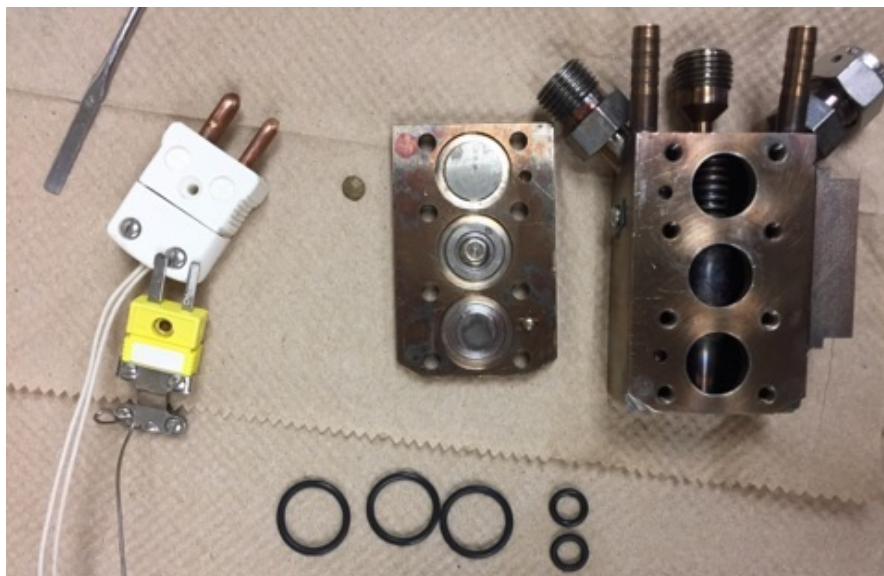
12. Rinse dome, stage pieces, and screen, **NOT THE WINDOWS OR O-RINGS,** thoroughly with acetone.
13. Rinse stage pieces and screen, **NOT THE WINDOWS,** thoroughly with H_2O.
14. Place dome, stage pieces, and screen into 1 L beaker, fill with H_2O and sonicate, using ultrasonic cleaner for 1 hour.
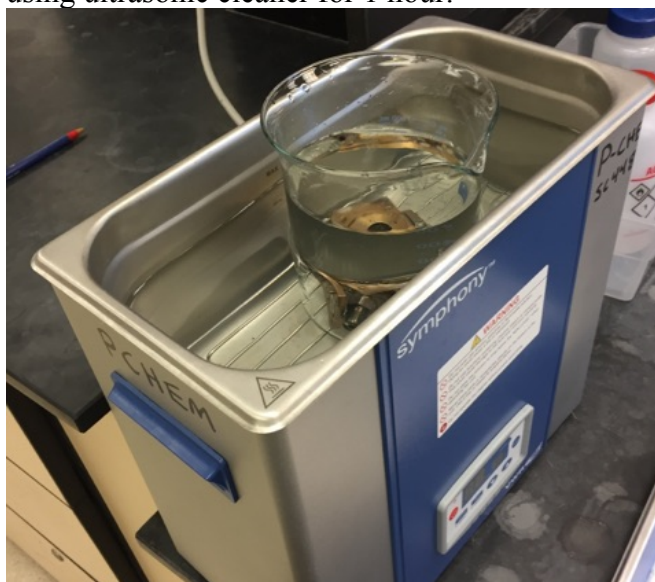
15. Dry stage pieces and screen using bench top air
16. Allow dry thoroughly by either sitting out or placing in oven at 150°C.
17. Once stage is dry (and cool), reassemble ensuring again all O-rings are not damage and are set right.
18. Bolt the bottom of the stage together using a spiral tightening sequence.
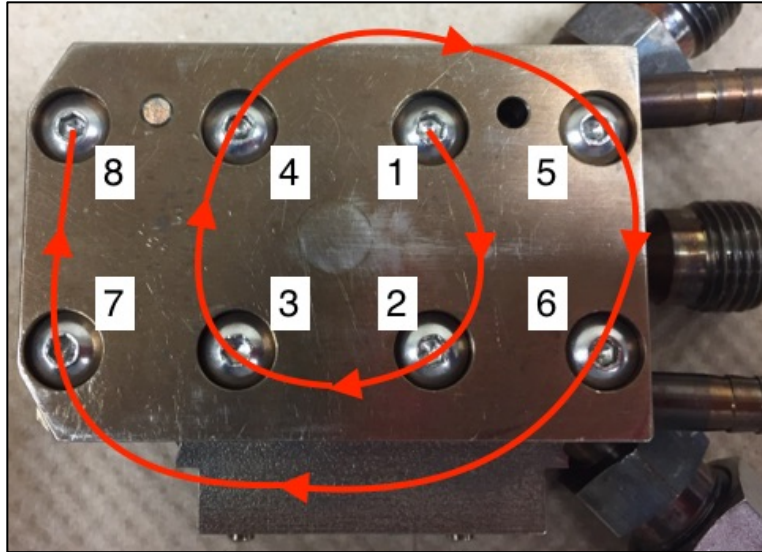
19. Return screen to sample cup.
20. Place powder sample into sample cup using spatula, lightly compacting to ensure no voids in the bulk and additionally that the surface is smooth.
21. Replace brackets and bolts onto the stage but do not tighten.
22. Reassemble stainless steel dome using "tool" ensuring all O-rings are situated correctly. **Do not over tighten windows.**
23. Carefully replace stage into DRIFTS box:
    a. Attach and tighten retention screw on the far side of the stage, located outside of DRIFTS box.
    b. Attach and tighten nuts to stage using 11/16 wrench.
24. Replace dome on sample stage, ensuring O-ring is seated correctly and tighten the brackets down using the bolts using a criss-cross sequence.
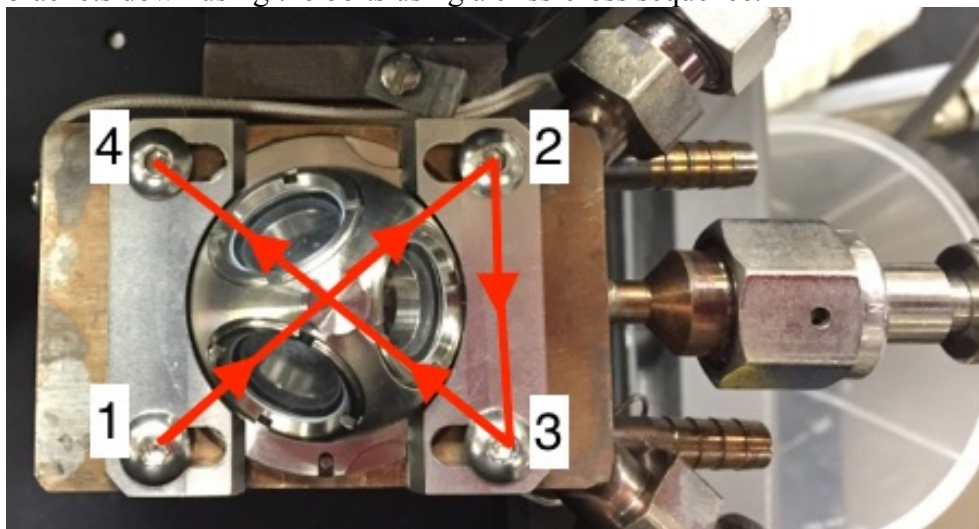
25. Fill vacuum manifold with UHP N_2 and open glass valve on backside of manifold and needle valve all the way. See section _____ for information on filling manifold.
26. With the vacuum system on: **If vacuum system is off see Staring Vacuum Pumps section.**

a. Fill aerosol trap with LN$_2$.
b. Flip "HIGH" pneumatic switch down (closed).
c. Flip "LOW" pneumatic switch down (closed).

d. Open divergent valve to direct flow directly to mechanical pump.

27. Slowly open bellows valve to the vacuum system.
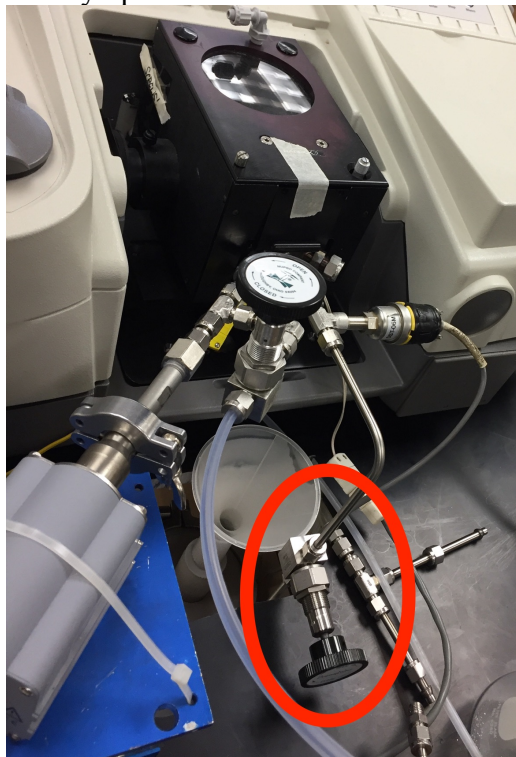
28. Once pressure in cell starts reducing, monitored on the PC:
    a. Slowly and simultaneously continue opening the bellows valve to the vacuum while opening the bellows valve to the vacuum manifold, maintaining a slow decrease in the pressure in the DRIFTS cell.
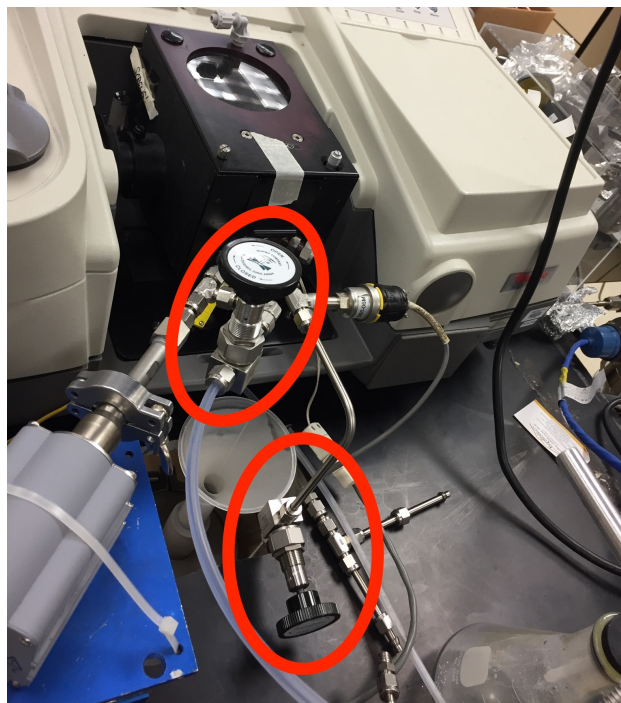
      b.   Refill vacuum manifold as needed with additional UHP N_2.

29. Once both bellows valves are entirely open, maintain a flow pressure of UHP N_2 through the sample of 20-50 torr with needle valve, monitored on PC, for 1-2 hours, depending on how absorbent the material is with atmospheric gasses, to help expel these gasses from the sample.

30. Slow flow of N_2 using needle valve on vacuum manifold until all the way closed.

31. Look at sample:
      a.   If it has collapse, open DRIFTS cell back up as before and add more powder sample.
      b.   If it is intact, continue.

32. Close bellows valve to vacuum manifold and again observe sample.

33. Pressure on PC should drop below 50 mtorr, if it has not:
      a.   Sample may need more purge time.
      b.   There may be a leak in the system somewhere.
           i.   This is likely not the case if ion guage pressure is below 1E-5 torr.

34. If it pressure drops below 50 mtorr, check TC1 and ensure it is below .5 Pa.

35. If so:
      a.   Refill aerosol trap with LN_2.
      b.   Close divergent valve
      c.   Make sure ion gauge filament is one
      d.   Flip "LOW" pneumatic switch up (open).
      e.   Flip "HIGH" pneumatic switch up (open).
      f.   Pressure for ion gauge should rise quickly then drop quickly back below 1E-5 torr.

36. Allow sample to evacuate overnight.
      a.   Should be 1-5 mtorr in cell [PC readout] after overnight evacuation.
      b.   Ion Guage should be 1E-6 to 1E-7 torr range.

Using the Spectrometer and OMNIC

1. Prepare sample as described in Section ___.
2. From "Collect" menu in toolbar select "Experiment Setup".
3. In Tab "Collect".
    a. Choose:
        i. File Format: Single Beam.
        ii. Number of scans
        iii. Resolution
    b. Select "OK"
4. From "Collect" menu in toolbar select "Experiment Setup".
5. In Tab "Bench"
    a. Values for parameters should be:
        i. Sample Compartment: Main
        ii. Detector: _____
        iii. Beamsplitter: KBr
        iv. Source: IR – Turbo
        v. Accessory: None
        vi. Window: None
        vii. Max range limit: 4000
        viii. Min range limit: 350
        ix. Gain: Autogain
        x. Velocity: 0.6329
        xi. Aperture: 74
    b. Observe, "Peak value".
    c. This value should be maximized by adjust the mirrors inside of the DRIFTS box.
        i. Remove plastics tabs coverings adjustment screws
        ii. Using 3/32" hex bit driver adjust screws to maximize peak value.
            1. Inner screw on each side (closest to middle of the box) is for course adjustment.
            2. The outer screw on each side (closest to the edge of the box) is for fine adjustment.
        iii. Once peak value is maximized select "OK".
6. Collect background by one of three methods:
    a. From "Collect" menu in toolbar select "Collect Background"
    b. Use small icon in toolbar "Col Back"
    c. Using keyboard "Ctrl+B"
7. Collect spectrum by one of three methods:
    a. From "Collect" menu in toolbar select "Collect Spectrum"
    b. Use small icon in toolbar "Col Spec"
    c. Using keyboard "Ctrl+S"
8. Reprocess singlebeam spectra collected by:
    a. Selecting spectrum/spectra to be reprocessed.
    b. From "Process" menu in toolbar select "Reprocess…"
    c. In Reprocess box up box:

  i. Select resolution to match what the spectrum/spectra was collected using.

  ii. Apodization: Happ-Genzel.

  iii. Phase correction: Mertz.

  iv. Zero filling: None.

  v. Final Format: Log(1/R)

  vi. Correction: None

  vii. Saved spectral range: 4000-349

  viii. Background file: select using "Browse" option

   1. Background selected should match the condition of spectrum/spectra being ratioed. Due to distortion caused by change in environment alone due to refractive index change. Shown below, where the nitrogen gas is the only thing used to cause the change.

    a. If spectrum/spectra is under vacuum the background should be under vacuum.

    b. If spectrum if during flow the background should also be during flow. (Typically during *in situ* experiments the first spectrum collected after flow is initiated is used as the background for the rest of the spectra collected during flow.)
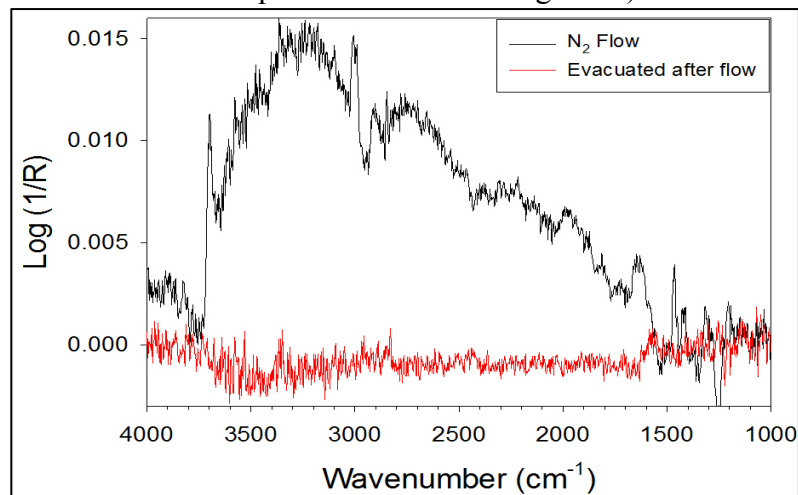
  d. Select "OK".

9. Zoom in on select regions by:

  a. Drawing box on screen by left clicking and hold and moving cursor.

  b. Click inside of drawn box.

10. OMNIC can identify peaks by either:

  a. From "Analyze" menu in toolbar select "Find Peaks…".

  b. Using keyboard "Ctrl+k".

11. Peak Resolve (Deconvolution).

  a. From "Analyze" menu in tollbar select "Peak Resolve".

Making a Gas Mixture

1. Close bellows valve from vacuum manifold to DRIFTS cell.
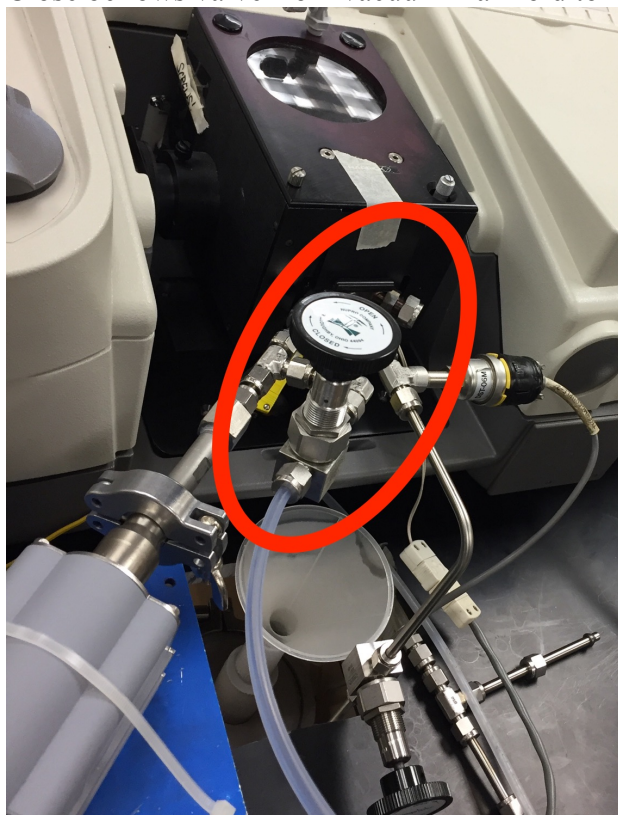
2. Make sure needle valve is all the way open and glass valve on backside of manifold is open.
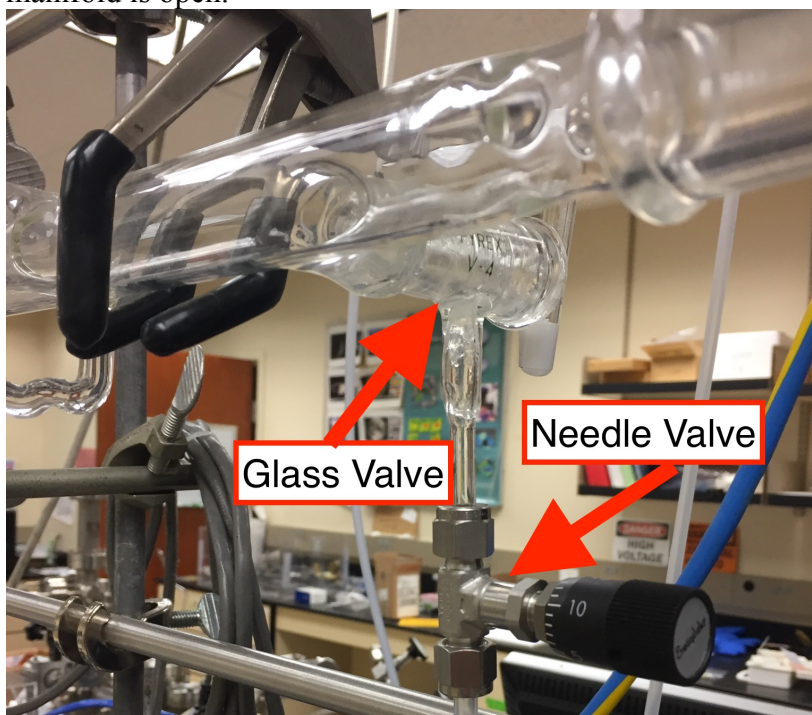
3. All valves to sample tubes or mixture bulb should be open.
    a. Sample tube themselves should be closed.
4. Valve to cajon fitting (where gas from cylinders is introduced) should be closed.
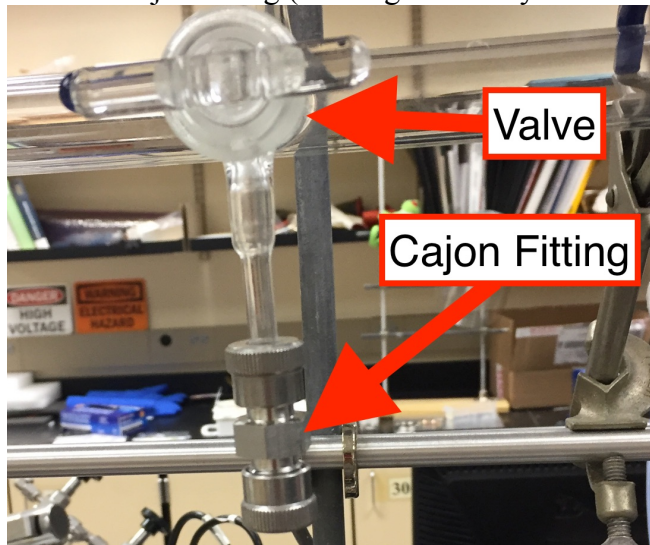
5. If not already done, evacuate manifold using mechanical pump, by turning vacuum pump on and opening glass valves to pump: 1) on side on glass aerosol trap and 2) on top of the manifold (the only one that the valve that faces downward).
    a. Typically only the one on top of the manifold is closed.

6. Once evacuated leak check the manifold by closing the valve on top of the manifold (2) and watching for any rise in the pressure.
    a. If there is no rise in pressure after 2 minutes proceeds to 7.
    b. If there is a rise in pressure it is likely the vacuum grease on the valves needs to be replaced.
    c. As a quick fix try rotating each valve back and forth to spread vacuum grease around for a better seal.
    d. Leak check manifold again
    e. If this does not work the grease should be replaced
    f. To change grease:
        i. Turn off the vacuum pump.
        ii. Bring manifold up to atmospheric pressure, by opening the valve that typically is used for import from gas cylinder (such as UHP N_2).
        iii. Put gloves on.
        iv. Individually remove each valve wiping off the old grease from the valve itself as well as where it sites in the manifold.
        v. Apply a thin even layer of new grease using q-tips.
        vi. Place the re-greased valve back into place and rotate it back and forth to smooth the grease around and ensure a good seal.
7. Close valve on backside of manifold (the one immediately before the needle valve).
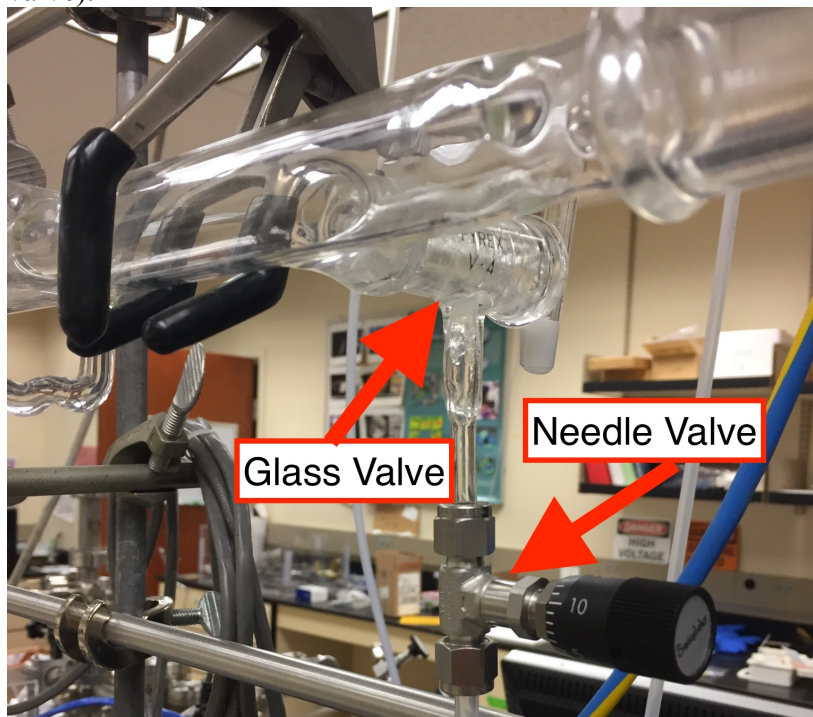
8. If using only gas from cylinder (as for purges) skip steps 9-13.

9. Ensure valves to the sample tube of interest and the mixture bulb are open.
    a. If the compound in the sample tube is new a series of three freeze-pump-thaw cycles should be performed prior to use.
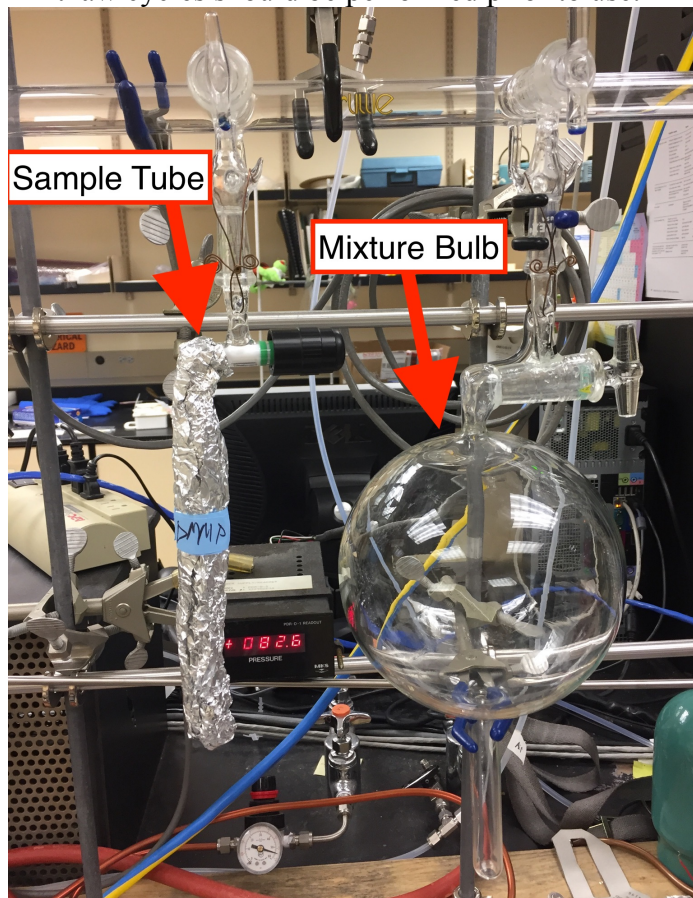
10. Slowly unscrew sample tube to allow vapor of the compound to fill the manifold.
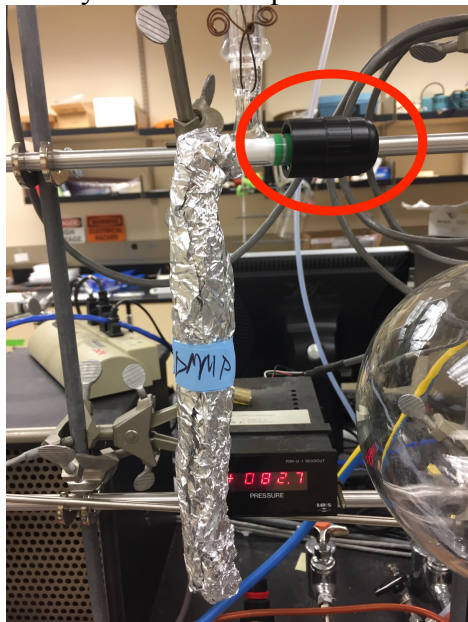
11. Once desired pressure is reached, screw the sample tube closed.

(0.6 torr is typical for DMMP)

12. Close the mixture bulb.
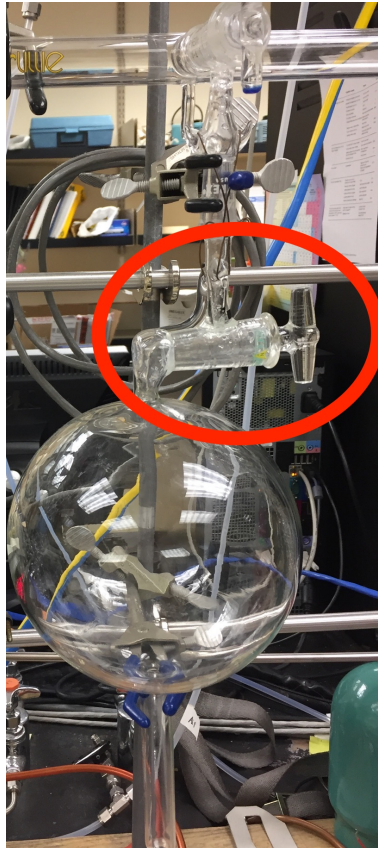
13. Re-evacuate the vacuum manifold by opening valve on top of manifold(2).

14. Start a very low flow rate of carrier gas (typically UHP N$_2$) from gas cylinder.

15. Attach Teflon tubing from gas cylinder to manifold via cajon fitting.
    a. It is best to put the tube up to the connection and back it away a few times to blow most atmospheric gasses out.
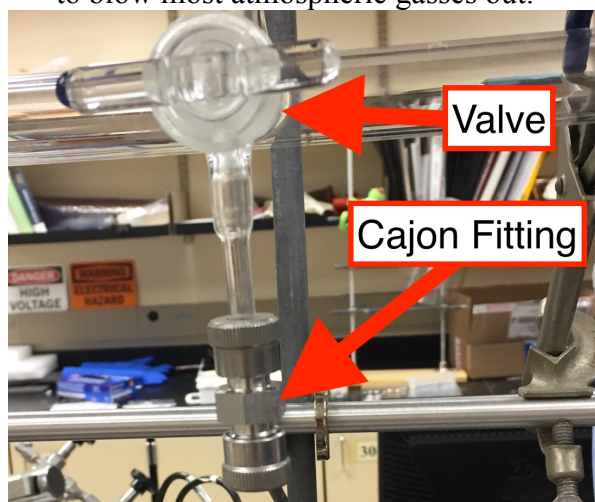
16. With the valve on top of manifold, to the vacuum, still open slowly open the valve to the cajon fitting. **IT DOES NOT NEED TO BE ALL THE WAY OPEN.**
17. Close off the valve to the vacuum.
    a. If the pressure is increasing too fast, re-evacuate and close valve to the cajon fitting more.
    b. Repeat until pressure increase rate is controlled.
18. SLOWLY open the valve to the mixture bulb ensuring that the flow is into the bulb rather than out of, by having a higher pressure in the manifold than what was put in from the sample tube.
    a. The manifold readout pressure will drop as the bulb is open due to large volume change.
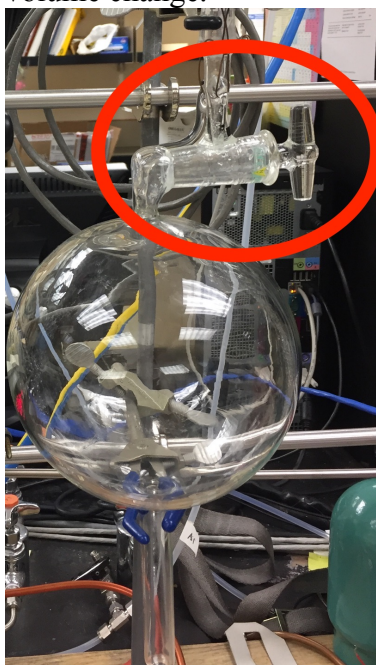
19. Once mixture is at the desired concentration close mixture bulb valve.

(.6 torr DMMP: 100 torr total is typical for a DMMP experiment)

20. Close valve to cajon fitting and turn off cylinder gas flow.
21. Open valve on backside of manifold (the one immediately before the needle valve).
22. Make sure needle valve is fully open. (This is to ensure line is full of mixture before starting experiment so there is minimal delay before exposure)
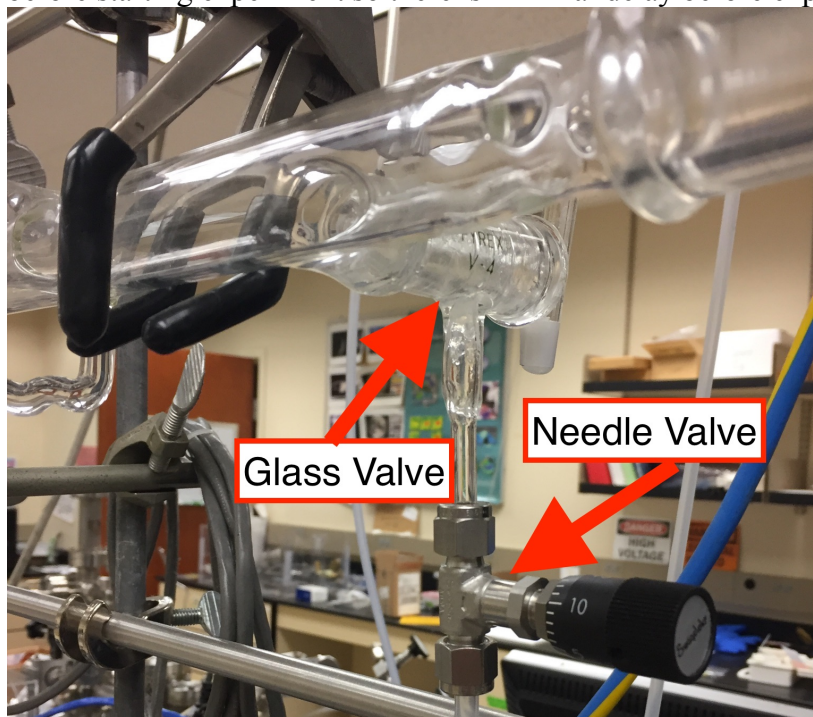
23. Re-evacuate the manifold.

Introducing gas mixture to prepared sample in DRIFTS cell

1. **CLOSE VALVE FROM ON TOP OF MANIFOLD (2) TO VACUUM**!
   If not, the mixture made will be lost in the next step.

2. Open mixture bulb and allow pressure to stabilize throughout the manifold.
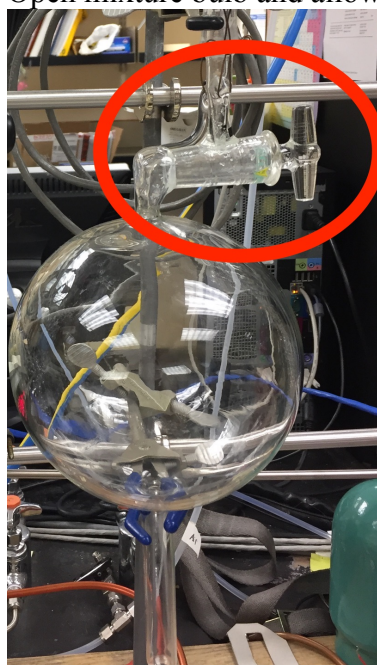
3. Note the pressure value for use later as

4. Close needle valve almost entirely.
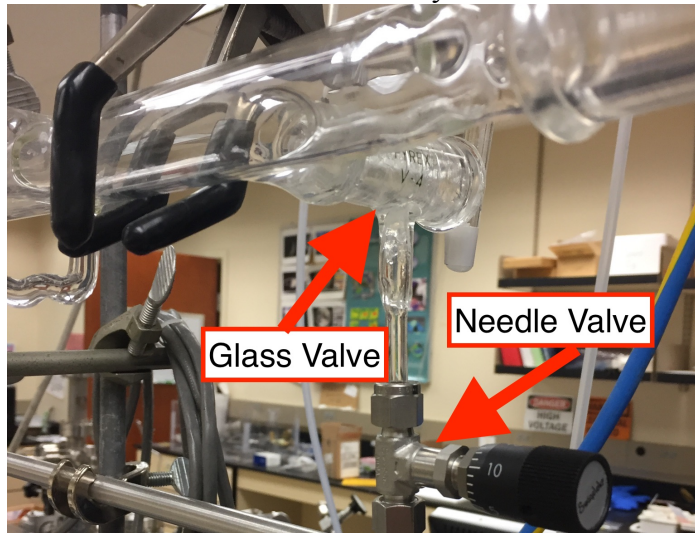
5. Take DRIFTS background spectrum, see **Using Spectrometer and Omnic** section.
6. On the DRIFTS vacuum system:
   a. Fill aerosol trap with LN_2.
   b. Flip "HIGH" pneumatic switch down (closed).
   c. Flip "LOW" pneumatic switch down (closed).

d. Open divergent valve to direct flow directly to mechanical pump.

7. Slowly open the bellows valve from vacuum manifold to DRIFTS cell. Pressure in cell, shown on the PC, should be allowed to reach 3-5 torr and maintained there throughout the duration of the experiment by continually opening the bellows valve until it is fully open, and then by using the needle valve on the vacuum manifold.
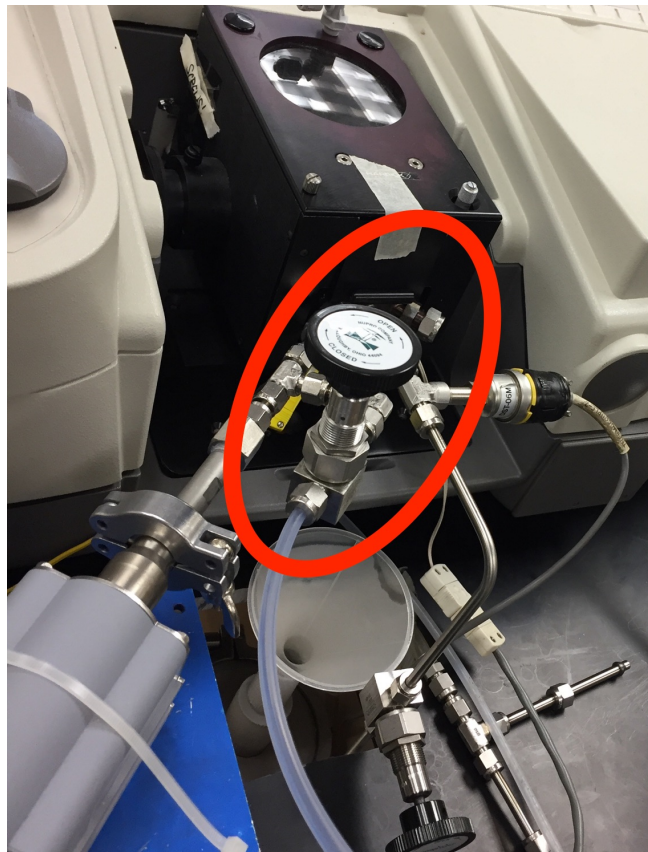
8. As soon as the pressure reaches 3 torr start the collection of a spectrum see **Using Spectrometer and Omnic** section. **This spectrum will be used as the "background" for subsequent spectra.**
    a. Note the pressure and peak value of the spectrum
    b. The pressure will be used to calculate moles used in gas mixture.

9. Continually collect spectra noting at the end of each the pressure remaining in the vacuum manifold and peak value of the spectrum.

a. $moles\ compound = \left(\dfrac{p_{compound}}{p_{total\ mixture}}\right)\left(\dfrac{(p_0-p_1)V}{RT}\right)$

10. Once the gas mixture is nearly used up the pressure in the DRIFTS cell will no longer be able to be maintained.
11. If the experiment is to continue:
    a. Close bellows valve to the DRIFTS vacuum system.
    b. Close the bellows valve to the vacuum manifold.
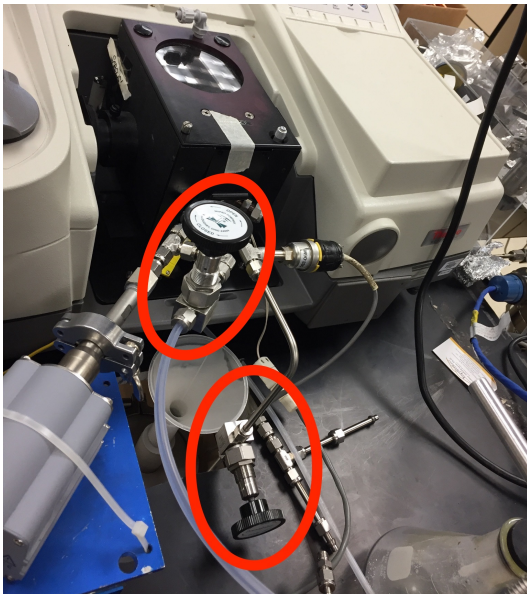
    c. Make a new gas mixture and continue as before.
        i. Be sure to reopen bellows valve to the DRIFTS vacuum system
12. If the experiment is to end:
    a. Sample can be left under vacuum overnight to see if further reaction occurs.
        i. Close the bellows valve to the vacuum manifold
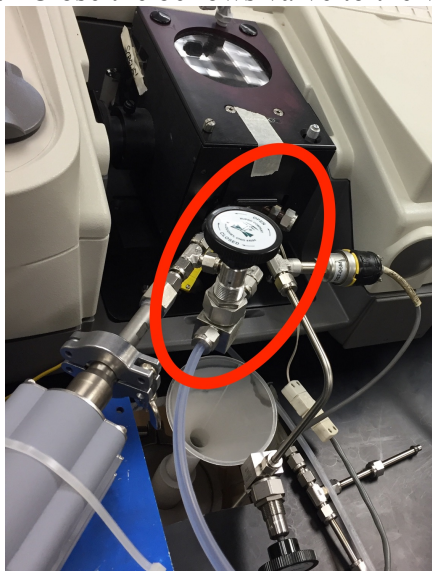
ii. Allow mechanical to reduce pressure sufficiently to switch to the turbo-molecular pump as described previously.
iii. Switch to the turbo-molecular pump
1. Open divergent valve to direct flow directly to mechanical pump.

2. Flip "LOW" pneumatic switch up (open).
3. Flip "HIGH" pneumatic switch down (open).

13. If experiment is to end, sample can be removed as described in **Preparing a New Sample** section.